

Universidad de El Salvador
Facultad de Ciencias Naturales y Matemática
Escuela de Física



Trabajo de graduación:
Chaos in Neutrino Fast Flavor Instability

Presentado por:
Erick Alcides Urquilla Orellana UO17001

Para optar al grado de:
Licenciado en Física

Asesores:

Ph.D Sherwood Richers
University of Tennessee, Knoxville


Dr. Raúl Antonio Henríquez Ortiz
Universidad de El Salvador

Ciudad Universitaria, San Salvador
Junio del 2023

Chaos in Neutrino Fast Flavor Instability

Erick Urquilla

Autor

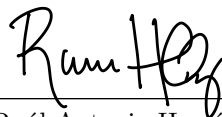


Erick Alcides Urquilla Orellana
Universidad de El Salvador

Asesores



Ph.D. Sherwood Richers
University of Tennessee, Knoxville

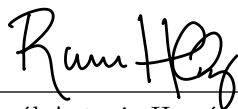


Dr. Raúl Antonio Henríquez Ortiz
Universidad de El Salvador

Tribunal calificador



Dr. Jose Francisco Melgar Brizuela
Universidad de El Salvador



Dr. Raúl Antonio Henríquez Ortiz
Universidad de El Salvador



B.Sc. Jose Roberto Dimas Valle
Universidad de El Salvador

Universidad de El Salvador

M.Sc. Roger Armando Arias Alvarado
Rector

PhD. Raúl Ernesto Azcúnaga López
Vicerrector Académico

Ing. Juan Rosa Quintanilla Quintanilla
Vicerrector Administrativo

Ing. Francisco Antonio Alarcón Sandoval
Secretario General

Lic. Rafael Humberto Peña Marín
Fiscal

Facultad de Ciencias Naturales y Matemática

Lic. Ernesto Americo Hidalgo Castellanos
Decano

M.Sc. Zoila Virginia Guerrero Mendoza
Vicedecana

Lic. Jaime Humberto Salinas Espinoza
Secretario

Escuela de Física

Lic. Guillermo Napoleón Morán Orellana
Director

Dedicatoria

A mi padre Erick, de él aprendí lo que es importante en la vida.

A mi madre Pati, ella creyó en mi primero.

A mi hermana Madai, será una médico increíble.

A mi hermano Boris, nunca admiraré a alguien más que a él.

Mi felicidad siempre estará vinculada a ellos.

Agradecimientos

Agradecimientos especiales a: Sherwood Richers, esta tesis no sería posible sin su asesoría, por animarme a participar en la escuela de verano del N3AS y por recibirme en UC Berkeley para trabajar en este proyecto. Raúl Ortiz, por su apoyo en mis etapas tempranas de investigación y por motivarme a participar en el Diplomado en Física Teórica del MCTP en México. Los profesores del MCTP especialmente el Dr. David Tamayo, quien me asesoró en una estancia corta de investigación allí. Wilson y Cesar, su amistad ha sido fundamental en mis años universitarios. La Division of Particle and Fields y el Topical Group on Few-Body Systems and Multiparticle Dynamics de la American Physical Society (APS) y la Facultad de Ciencias Naturales y Matemática de la Universidad de El Salvador por financiar mi viaje a la reunion de abril de la APS en Mineapolis, Minnesota, USA para presentar los resultados de este trabajo. Al club de lectura de papers sobre las transformaciones de sabor rápidas de neutrinos. Los profesores de la Escuela de Física de la Universidad de El Salvador, de quienes aprendí los fundamentos de la física. Notables, el profesor Melgar Brizuela, Roberto Dimas y Américo Mejía, quienes accedieron a mis intereses en la física teórica impartiendo las materias electivas de mi interés.

This work was partially supported by the NSF Award No. AST-2001760.

Abstract

Neutrinos play a crucial role in explosive stellar events. In core collapse supernovae (CCSN), neutrinos produced thermally in the proto-neutron star drive the CCSN dynamics, reviving the shock wave that causes the explosion. In neutron star mergers (NSM), neutrinos can significantly affect the ratio of neutrons to protons in the ejected mass via charged-current reactions, having a big impact on the production of heavy elements. Simulations have revealed that in those systems neutrinos undergo substantial fast flavor instabilities that make it challenging to fully understand the neutrino non-linear many-body dynamics, mainly because of the large number of neutrinos involved and the small spatial scale of the neutrino flavor oscillation in comparison with the CCSN and NSM spatial scale. In simplified neutrino models (bipolar oscillations), the presence of chaos in the flavor evolution has been proposed. Since chaotic systems are very sensitive to initial conditions, i.e., trajectories of slightly different initial conditions diverge exponentially, our ability to predict the neutrino flavor behavior in CCSN and NSM could be limited. To clarify this problem, we approximate the behavior of neutrinos inside NSM by simulating neutrino fast flavor instabilities in a domain a few centimeters wide. Our goal is to analyze the dynamics of nearby flavor states in the presence of neutrino fast flavor instabilities. We solve the neutrino quantum kinetic equation numerically including the neutrino self-interaction term in the flavor Hamiltonian, using the particle-in-cell code EMU under the mean field approximation. We conclude that solutions with nearby initial states diverge exponentially in the non-linear regime of the neutrino flavor evolution, demonstrating the presence of chaos. This produces a huge uncertainty in both the spatial flavor neutrino distributions and the density matrix of the individual computational particles. However, the domain-averaged neutrino density matrix component is not highly affected by chaos (1% maximum uncertainty) and could be used as a key variable in global neutrino simulations of CCSN and NSM.

Contents

Dedicatoria	ix
Agradecimientos	xi
Abstract	xiii
Contents	xv
List of figures	xvii
1 Introduction	1
2 Neutrino oscillations	5
2.1 Solar neutrinos	5
2.2 Atmospheric neutrinos	8
2.3 Neutrino flavor oscillation in vacuum	9
2.4 Neutrino-matter interaction (MSW effect)	14
2.5 Neutrino-neutrino interaction	19
3 Non-linear dynamics and chaos	23
3.1 Dynamics	23
3.2 Linear and non-linear dynamical systems	24
3.3 Chaos	25
3.4 The logistic equation	27
3.5 Chaos in the two beam neutrino model	34
3.5.1 Stationary solutions	38
3.5.2 Bipolar solutions	38
3.5.3 Non-periodic solutions	39
4 Methodology	41
4.1 PIC quantum neutrino transport	41
5 Results and discussion	45
5.1 One dimension fiducial simulation	45
5.2 Neutron star merger simulation	49
6 Conclusion	61
References	63
Appendix: Convergence tests	73

List of Figures

2.1	Solar neutrino flux from reference [1]. Figure used with permission of the authors and The Astrophysical Journal.	7
2.2	Flavor oscillation in vacuum for a neutrino initially emitted in a pure electron flavor state. The blue, green and orange lines represent the probability to detect the neutrino in electron, muon and tau flavor states, respectively. The mixing matrix was characterized by the mixing angles $\sin^2 \theta_{12}/10^{-1} = 3.11$, $\sin^2 \theta_{23}/10^{-1} = 5.55$ and $\sin^2 \theta_{13}/10^{-2} = 2.195$. The mass square differences are $\Delta m_{21}^2 = 7.42 (10^{-5} \text{ eV}^2)$, $\Delta m_{32}^2 = 2.4367 (10^{-3} \text{ eV}^2)$ and $\Delta m_{31}^2 = \Delta m_{32}^2 + \Delta m_{21}^2$. The neutrino energy is 50 GeV. Natural units were considered.	13
2.3	Feynman diagrams depicting (a) the coherent forward elastic scattering process due to the weak charged current interaction of electron neutrinos with background electrons via the exchange of a W boson. (b) shows the elastic scattering process of neutrinos with background matter by the weak neutral current interaction via the exchange of a Z boson.	15
2.4	Flavor oscillation in vacuum (solid line), matter (dotted line) and resonance (dashed line) for a neutrino initially emitted in a pure electron flavor state. The black and orange lines represent the probability to detect the neutrino in electron and $x = \mu + \tau$ flavor states, respectively. The two-flavor mixing matrix was characterized by a mixing angle of $\theta = 25^\circ$. The mass square difference is $\Delta m^2 = 7.42 (10^{-5} \text{ eV}^2)$. The neutrino energy is 50 GeV. Natural units were considered. The number density of electrons in the background medium was established so that $A_{CC} = 2\sqrt{2}EG_F n_e / \Delta m^2 = 1 \times 10^{-6}$. The resonance is achieved by setting $A_{CC} = \Delta m^2 \cos 2\theta$	18
3.1	First nine iterations of the logistic equation with a growth parameter r of 0.75 (upper panel) and 1.60 (lower panel). Different initial conditions x_0 that spanned the range between 0.1 and 0.9 are shown. In the upper panel, the logistic equation has a stable equilibrium point at $x_i = 0$. Independent of the initial population, the species goes extinct. The same trend occurs for $0 \leq r < 1$. In the lower panel, the solutions do not follow $x_i = 0$ as it is now an unstable equilibrium point. $x_i = 0.37$ is the new stable equilibrium point. Independent of the initial population, the logistic equation follows the stable equilibrium point as an asymptotic value. This is the main tendency for $1 \leq r < 3$. In this range, the stable equilibrium point takes the value of $x_i = (r - 1)/r$. For $r \geq 3$, all the equilibrium points became unstable.	28

3.2	Doubling period tendency of the logistic equation as the growth rate parameter r increases. In the top panel are shown the iterations of the logistic equation with $r = 3.30$. At iteration 16 the solution starts a periodic behavior every two iterations (two-cycles). This periodic behavior starts abruptly at $r = 3$. When r increases to approximately 3.45 the logistic equation changes abruptly from a two-cycle to a four-cycle behavior. In the lower panel, the four-cycle behavior of the logistic equation with $r = 3.49$ is plotted. This double period trend continues as r increases.	29
3.3	Iterations of the logistic equation for two different growth rates r and initial conditions between 0.1 and 0.9. The upper panel shows the logistic equation for $r = 3.57$. This corresponds to the chaotic regime of the logistic equation. The solution will never repeat its past behavior. The lower panel shows the logic equation for 3.84. At this point, the logistic equation recovers a three-cycle periodicity. However, as we increase r the period doubling behavior starts until it reaches the chaotic regime again.	32
3.4	Final set of asymptotic values (bifurcation diagram) (top panel) and Lyapunov exponents (Eq. 3.4.12) (bottom panel) in dependence of the growth rate parameter r for the logistic equation. In the non-chaotic regime (negative Lyapunov exponents), the logistic equation exhibits periodic behavior. This is represented by a finite set of final asymptotic values in the bifurcation diagram. In the chaotic regime (positive Lyapunov exponents), the solution never repeats its past behavior. This corresponds to an infinite set of asymptotic values in the bifurcation diagram. Images generated and distributed under the CC-BY-NC-ND license [2].	33
3.5	Sensitive to the initial condition in stable and chaotic systems. The panel (a) shows two four-cycle solutions of the logistic equation that are iterated starting with a close initial condition of $x_0 = 0.01$ and $0.01 + 10^{-10}$. The panel (b) shows the difference between the two solutions in the panel (a). Both simulations converge. On the contrary, in panel (c) are plotted two chaotic solutions to the logistic equations with nearby initial conditions $x_0 = 0.01$ and $0.01 + 10^{-10}$. As panel (d) shows, the difference between the two solutions grows exponentially over time but stops after approximately 25 iterations.	35
4.1	Deposition algorithm: Process of construction of the cell's neutrinos and antineutrinos distribution. Each computational particle (orange dots) is modeled by an extended quadratic shape function that depends on the coordinates. Given by the shape function, every computational particle i contributes a fraction w_{ij} of their particles to the cell distribution j (black dot). In this form, the neutrinos and antineutrinos number density and flux at each cell are given by the equation 4.1.7.	43
4.2	Interpolation algorithm: To compute the neutrinos and antineutrino's number density and flux at the computational particle i location, the interpolation algorithm runs over each cell distribution j adding a fraction w_{ij} of the cell's neutrino and antineutrino number density and flux. This procedure is mathematically represented in EMU with the equations 4.1.8.	44
5.1	Time evolution of the neutrino's density matrix components averaged over the entire domain in the one-dimensional fiducial simulation. The yellow area describes the linear regime in which the unstable modes grow exponentially matching the prediction of the linear stability analysis. The gray area represents the non-linear regime in which the system approximately reaches the flavor equilibrium (black dotted line). The antineutrino density matrix components averaged over the entire domain follow the same trend.	46

5.2	Time evolution of the neutrino’s density matrix diagonal components of a single computational particle. The yellow and gray regions represent the linear and non-linear regimes, respectively. In the non-linear regime, the flavor transformation is highly stochastic. Contrary to the behavior of the averaged density matrix components, individual particles exhibit larger oscillation amplitudes around the flavor equipartition (black dotted line). The antineutrino’s density matrix diagonal components follow the same trend.	47
5.3	Difference between the domain-averaged electron components of the density matrix of two one dimensional fiducial neutrino simulations with close flavor initial conditions. The yellow and gray shaded areas represent the linear and non-linear regimes, respectively. In the upper panel, both simulations started with a close initial condition at $t = 0$ ns (linear regime). The main tendency is established by the exponential growth of fast unstable modes. In the lower panel, both simulations started with a close initial condition at $t = 2.7$ ns (non-linear regime). The main trend is an exponential divergence. This suggests the neutrino system is highly sensitive to the choice of the initial condition. The difference between the domain-averaged electron components reaches an asymptotic behavior in the upper and lower panels, reaching a maximum separation of the order of 10^{-2} . The others domain-averaged density matrix components showed the same tendency.	48
5.4	Behavior of the domain-averaged density matrix components for the NSM simulation. The yellow shaded area represents the linear regime in which the unstable modes grow exponentially according to the dispersion relation given by the linear stability analysis. The gray shaded area represents the non-linear regime in which the system reaches a flavor asymptotic behavior without completely reaching the flavor equipartition (black dotted line).	51
5.5	Time behavior of the diagonal components of the density matrix of a single computational particle in the NSM simulation. The linear and non-linear regimes are represented by the yellow and gray shaded regions, respectively. In the non-linear regime, the flavor transformation is highly stochastic. Contrary to the behavior of the averaged density matrix components, individual particles exhibit larger oscillation amplitudes approximately around the flavor equipartition (black dotted line).	52
5.6	Divergence between two neutron star merger neutrinos simulations with close initial conditions. The yellow and gray shaded areas represent the linear and non-linear regimes, respectively. In the linear regime, the two neutrino solutions diverge exponentially following the fast unstable modes. In the non-linear regime, unstable modes saturate, stopping the exponential growth due to the fast flavor instability. However, the difference between the two neutron star merger neutrinos simulations continues to diverge exponentially at a lower rate between 0.25 and 1.8 ns. Finally, the solution reaches the maximum divergence value imposed by physical constraints (black dashed line).	53
5.7	Divergence between two neutron star merger simulations with close initial conditions in the non-linear regime. At this time, the unstable modes are saturated and have stopped growing exponentially. The stochastic neutrino flavor transformations are the dominant phenomenon. The difference between the two close initial condition neutron star merger simulations grows exponentially, proving the unstable dynamics of the initial condition of the neutron star merger neutrinos system.	54

- 5.8 Absolute difference between the diagonal components of the density matrix for a single particle in the neutron star merger PIC simulation. Although it is not appreciable in the linear vertical domain of the figures, the difference between each of the diagonal density matrix components grows exponentially in time. At approximately 65 ns the difference between each component reached an order of magnitude of 10^0 and became appreciable in the plots. In the bottom panel, the sum of the absolute value of the difference between each density matrix component is plotted. At approximately 75 ns the uncertainty between the sum of the diagonal components of the density matrix reaches the value of one, implying a 100% uncertainty. 56
- 5.9 Top panel: Spectrum of the divergence rate between two neutron star merger neutrino simulations with close initial conditions Both simulations start evolving in time at 2.65 ns with a difference between them of 10^{-6} . The difference between the two solutions is normalized each 0.9 ns conserving the direction. This corresponds to the Bennettin algorithm to compute the maximum Lyapunov exponent [3]. However, we are mostly interested in the initial trend of the difference between the two solutions. The spectrum showed divergence and convergence directions between the neutrino solutions with close initial conditions. The existence of directions of divergence (positive Lyapunov exponents) in the neutrino flavor state space is clear prove of chaos in the neutrino flavor evolution. Lower panel: Maximum Lyapunov exponent estimation (Eq. 5.2.8). The maximum Lyapunov exponent can not be lower than 10^8 s^{-1} . Even when this plot is not conclusive about the value of the maximum Lyapunov exponent because only the initial trend of the simulations was considered, it provides a good estimation of the main initial divergence tendency of the solutions. The observed trend agreed with the existence of positive Lyapunov exponents and chaos. 57
- 6.1 Test for convergence of the number of particles. The vertical axis shows the computed values of the exponent λ in equation $|\vec{r}_{\text{bas}} - \vec{r}_{\text{per}}| = A_0 e^{\lambda(t-t_0)}$ for five one-dimensional fiducial simulations in which were emitted 92, 378, 6022, 24088 and 54202 particles per cell in an approximately isotropic fashion. Each simulation used a $1 \times 1 \times 64$ centimeter domain divided into 1024 cells in the z direction. We added perturbation of magnitude $A_0 = 10^{-10}$ in a random direction when the neutrino system reached the non-linear regime. As the number of particles in the simulation grow, the values of λ obtained drop. The convergence is attained for a number of directions greater than 240888. 75
- 6.2 Test for convergence of the perturbation amplitude. Calculated values of λ in equation $|\vec{r}_{\text{bas}} - \vec{r}_{\text{per}}| = A_0 e^{\lambda(t-2.65 \times 10^{-9})}$ for five one-dimensional fiducial simulations for each of the three initial perturbation amplitudes: $A_0 = 10^{-6}, 10^{-8}, 10^{-10}$. Each simulation has a domain of $1 \times 1 \times 64$ cm with 1024 cells in the \hat{z} direction and 24088 particles emitted in an approximately isotropic distribution from the center of each cell. The blue-shaded region represents a 2σ spread for λ with an initial perturbation amplitude of 10^{-10} . Less dispersion in λ is produced by bigger perturbations without changing the mean significantly. The orange-shaded region represents a 2σ spread for λ with an initial perturbation amplitude of 10^{-8} , the for green-shaded region represent the same for a perturbation amplitude of 10^{-6} 76

6.3	Test for convergence of the simulation domain. Calculated values of λ in equation $ \vec{r}_{\text{bas}} - \vec{r}_{\text{per}} = A_0 e^{\lambda(t-t_0)}$ for three one-dimensional fiducial simulations with domains of 16, 32 and 64 cm in the \hat{z} and 1 cm in the \hat{x} and \hat{y} directions. 24088 particles per cells were consider in 16 cells per cm. Neutrinos were emitted in nearly isotropic directions. In the neutrino non-linear phase after saturation of the instability, we added a perturbation of magnitude $A_0 = 10^{-6}$ in a random direction. The values λ stay approximately constant as the simulation domain increase, having a small impact on the computation of λ	77
6.4	Test for convergence of the number of cells. Computed values of λ from equation $ \vec{r}_{\text{bas}} - \vec{r}_{\text{per}} = A_0 e^{\lambda(t-t_0)}$ for three one-dimensional fiducial simulations with 256, 512 and 1024 cells. A $1 \times 1 \times 64$ cm domain was considered for all simulations. Neutrinos were emitted in nearly 24088 isotropic directions. We added a perturbation in a random direction of magnitude $A_0 = 10^{-6}$ when the neutrino system reached the non-linear phase after the saturation of the instability. The obtained values of λ slightly increase as the number of cells increase.	78

Chapter 1

Introduction

It is well known that neutrinos oscillate between electron, muon and tau flavors while propagating [4, 5]. This flavor transformation can be strongly affected by the interaction of neutrinos with the background matter (charged leptons and quarks) via the Mikheyev-Smirnov-Wolfenstein (MSW) effect [6, 7]. In addition, the neutrino-neutrino coherent forward interaction may result in sophisticated flavor oscillation phenomena in dense neutrino environments [8, 9, 10].

Neutrino flavor transformations play a crucial role in astrophysical systems, including binary mergers and core-collapse supernovae. After the big bang, these are the only sites in the universe where neutrinos are produced at densities high enough to be briefly confined [11]. Core-collapse supernovae are produced when a massive star collapses after exhausting its nuclear fuel. The infalling material abruptly stops when the core reaches the nuclear density generating a bounce and a shock wave that propagates through the star producing the explosion. Neutrinos generated in the deep region of the star drive the explosion carrying energy from the collapsed core to the infalling material below the shock front. In the delayed supernova scenario, this mechanism propels the stalled shock wave through the star, causing the explosion [12, 13, 14, 15]. The explosion energies, neutrino luminosity, electromagnetic signals, and ejected material have all been simulated by a variety of core-collapse supernova simulations [16, 17, 18, 19]. However, several sources of uncertainties, such as a consistent treatment of the quantum neutrino transport [15, 20], the equation of state for matter beyond nuclear densities [21, 22] and the nuclear reaction rates of heavy and very unstable elements [23], make the core-collapse supernova explosion mechanism an open problem that requests further studies and simulations [24].

Neutron star mergers and supernovae are also prime candidates for the production of much of the heavy nuclei of the universe. The neutrinos emitted from the resulting hot accretion disk and ejected material can significantly affect the production of neutrons and protons via the following reactions:

$$p + \bar{\nu}_e \leftrightarrow n + e^+ \tag{Eq. 1.0.1}$$

$$n + \nu_e \leftrightarrow p + e^- \tag{Eq. 1.0.2}$$

Since different neutrino flavors interact in different ways with background matter, neutrino flavor transformation can have a big impact on the final production of heavy elements [25, 26, 27, 28, 29].

Neutron star mergers are being actively investigated observationally as important multimessenger events: gravitational waves, short gamma-ray bursts, kilonovae, electromagnetic afterglows and neutrinos [30, 31, 32, 33]. The gravitational wave event GW170817 [34] of two neutron stars colliding was widely studied in several multimessenger observations [35, 36]. The observed Kilonova light curve that resulted from the radiative decay of nuclei in the ejected material was the first direct detection of the synthesis of heavy elements via a rapid neutron capture process (r-process) [37, 38]. From a theoretical and computational perspective, several simulations have attempted to forecast the amount and composition of material ejected during compact object mergers, as

well as the electromagnetic signals, gravitational waves, and final compact object that results from the merger [39, 40, 41, 42, 43, 44, 45]. These simulations include the effects of general relativity, inviscid hydrodynamics, magnetic fields, a dense nuclear equation of state, nuclear reactions, and the transport of energy by neutrinos [46]. The neutrino flavor transformations have yet to be fully implemented in a neutron star merger simulation, though.

Despite its importance, the neutrino flavor transformation in dense neutrino environments is not fully understood. The flavor transformation due to the non-zero neutrino propagation mass and the MSW effects depends linearly on the neutrino quantum states. However, an ensemble of neutrinos undergoing coherent forward scattering among themselves is an interacting quantum many-body system that makes the flavor evolution equation highly non-linear. It is expected that the neutrino system will develop quantum entanglement between the neutrinos, which can leave imprints on their flavor evolution histories [47]. Quantum many-body systems involve an exponential increase in system complexity as the number of neutrinos increases. The Hilbert space of an ensemble of N interacting neutrinos with a number of flavors n_f has a dimension of n_f^N . State of the art full quantum many-body neutrino simulations do not involve more than 20 neutrinos [47, 48, 49, 50]. Several methods have been used to approximate the neutrino many-body evolution, based on compact representations of the wave function through tensor network methods [51, 52, 53] and other product state configurations [54] and this allows hundreds of neutrinos to be simulated [47]. Neglecting neutrinos quantum entanglements, the neutrino ensemble can be described in the mean field approximation by evolving N pure quantum states as $n_f \times n_f$ density matrices; this reduces the Hilbert space to a dimension of Nn_f . Formally, the mean field approximation is defined as an approximation of the expectation values of operator products as a product of the expectation values of individual operators [47]. Even with all this approximation in hand, a global implementation of the neutrino flavor transformations in neutron star mergers and core-collapse supernovae simulations is not computationally possible because of the highly non-linear complexity of the Hamiltonian, the large number of neutrinos and the small spatial and timescale of the flavor transformations [55, 56].

Although preliminary research suggested that neutrino flavor oscillations are not crucial for the dynamics of core-collapse supernovae [57, 58], the recently explored possibility of fast flavor instabilities deep inside core-collapse supernovae and neutron star accretion disks (see e.g. [59, 60, 56]) change the scenery, opening the possibility to neutrino flavor transformation on time and spatial scales of a few nanoseconds and centimeters, respectively [61, 62, 63, 55, 8]. Fast flavor conversion has the potential to drastically alter the elements generated in the ejected material, even if it has little bearing on the dynamics of a core-collapse supernova explosion [64, 65]. Recent numerical investigations have shown that simpler neutrino models exhibit fast flavor instabilities [66, 24, 46, 8, 67, 68, 69, 70]. At a specific site in a dense neutrino environment, a necessary and sufficient requirement for the emergence of fast flavor instabilities is at least one direction in which equal numbers of neutrinos and antineutrinos are moving, canceling the flux. This is a crossing in the lepton angular distribution [58, 66]. Since the interiors of supernovae and mergers cannot be observed directly, simulation must be used to determine whether fundamental physics, as it is currently understood, can account for what we observe in nature. Several numerical studies that simulates classical transport of neutrinos (no flavor oscillation) suggested favorable conditions for fast flavor conversions in the core-collapse supernovae's protoneutron star convection region [71, 72], under the shock wave [73, 74, 75], above the shock wave [76, 77], during the cooling phase of the protoneutron star [78] and neutron star merger accretion disk [56, 79] (see reference [11] for a review of the ways to test the emergence of neutrino fast flavor instability and recent results of possible fast flavor unstable regions in core-collapse supernovae and neutron star merger simulations).

In addition to the computational difficulty, the non-linear nature of the neutrino flavor transformation in dense neutrino environments offers other inconveniences. Previous studies have suggested the presence of chaos in the bipolar neutrino flavor oscillations [80, 81]. The flavor trajectories were observed to diverge exponentially at slightly altered initial conditions, disrupting the bipolar

oscillation's periodicity. Since future observations of supernovae neutrinos will reveal critical scientific information about the collapsing stellar core [82], a chaotic flavor development could severely restrict our capacity to predict and explain the neutrino behavior in supernovae and also neutron star mergers. Despite its importance, our current understanding of chaos in dense neutrino systems is limited to the two-beam neutrino model, which consists of two neutrino flavors with two opposing momentum states [80, 81]. In order to shed light on the problem, I extend the study of chaos to a more realistic distribution of neutrinos that experience fast flavor instabilities. In this thesis, I simulate the one-dimensional fiducial simulation extensively discussed in reference [24] and the neutron star merger described in reference [56]. The main goal is to characterize the sensitivity depending on the initial neutrino flavor state and the impact of chaos on our capacity to foresee the evolution of neutrino flavor in dense neutrino astrophysical systems.

Chapter 2

Neutrino oscillations

This chapter is focused on the theory of the neutrino oscillation. In the next two Sections, 2.1 and 2.2, I will briefly describe the neutrino observations that led to the experimental discovery of the neutrino flavor oscillation and the non-zero mass of neutrinos. I will expose the theory of neutrino flavor transformation in vacuum in Section 2.3. In Section 2.4, I will expose how the neutrino interaction with background matter (NSM effect) impacts the flavor transformations. Finally, I will expose the fast flavor conversion result of the neutrino-neutrino coherent forward scattering in Section 2.5.

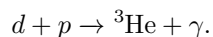
The main structure of this chapter is inspired by the outstanding readings of: Fundamentals of neutrino physics and astrophysics by C. Giunti and C Kim [83]; Neutrino physics by K. Zuber [84]; Neutrino oscillations: a practical guide to basics and applications by F. Suekane [85]; Chapter 9 and 11 of Introduction to elementary particle by D. Griffiths [86] and Chapter 11, 12 and 13 of Modern particle physics by M. Thomson [87].

2.1 Solar neutrinos

Solar neutrinos played a crucial role in the discovery of the non-zero neutrino masses inferred by the neutrino oscillation phenomenon. In low-mass stars like the sun, the source of energy that keeps the stars stable against gravity is primarily from the proton-proton chain, in which protons experience the energetically favorable fusion reactions to alpha particles¹ [88]. The proton-proton chain starts with the reaction of two protons producing a deuteron, a positron and an electron neutrino, or the combination of two protons with an incoming electron, producing a deuteron and an electron neutrino



eventually, the deuteron picks up another proton to form a Helium-3 nucleus, releasing energy in the form of a photon



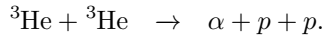
In this state, Helium-3 reacts in three different ways:

1. It can join a proton producing an alpha particle (Helium-4 nucleus), a positron and an electron neutrino

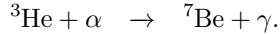


¹In heavier main-sequence stars, the dominant mechanism is the CNO (Carbon-Nitrogen-Oxygen) cycle.

2. It can combine another Helium-3 nucleus to form an alpha particle and two leftover protons



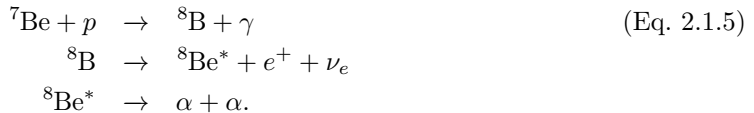
3. It can join an alpha particle to make Beryllium-7, with the emission of a photon



The final part of the proton-proton chain is the transformation of Beryllium-7 into alpha particles. Beryllium-7 absorbs an electron producing Lithium-7 and an electron neutrino. Eventually, Lithium-7 picks up a proton emitting two alpha particles

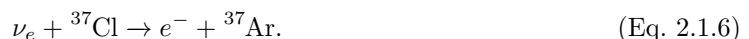


alternatively, Beryllium-7 can absorb a proton, producing unstable Boron-8 and a photon, Boron-8 quickly decays into an unstable Beryllium-8 excited state with a positron and an electron neutrino, finally, Beryllium-8 decays to two alpha particles



In order to experimentally test the proton-proton chain in the standard solar model, it was required to perform a precise theoretical calculation of the neutrino flux emitted in the five reactions in equations 2.1.1, 2.1.2, 2.1.3, 2.1.4 and 2.1.6. This was primarily done by Bahcall during the decade of the 1960s [89]. A more recent report can be seen in Figure 2.1.

The earliest solar neutrino experiment was done by Raymond Davis at the Homestake Solar Neutrino Observatory in the Homestake Mine in South Dakota, USA. The experiment consisted of a tank containing 615 tons of dry cleaning fluid (C_2Cl_3) which was required to be deep underground to eliminate the cosmic ray background. In this experiment, neutrinos with energies greater than 0.814 MeV interacted with the Chlorine-37 producing radioactive Argon-37 that was detected and counted



Theoretical estimates predict around 1.7 neutrino interactions per day. However, Davis, et al. only observed 0.48 ± 0.04 neutrino interactions per day [90]. This was about one third of the prediction by Bahcall, et. al. in reference [89]. This discrepancy was reported in 1968 in references [91] and [92] and marked the birth of the solar neutrino problem, the precursor of the discovery of the neutrino oscillations due to the existence of a non-zero neutrino mass. For this experiment, Raymond Davis was awarded the 2002 Physics Nobel Prize.

Subsequently, the Soviet–American Gallium Experiment (SAGE) which began operations in 1989, confirmed the solar neutrino discrepancy [93]. SAGE consisted of a 50-ton gallium detector stored deep underground at the Baksan Neutrino Observatory in the Caucasus Mountains in Russia. Unlike the Homestake experiment, SAGE detected neutrinos via the Gallium reaction



which is a less energetic reaction than the electron neutrino chlorine in equation 2.1.6 used in the Homestake experiment. This reaction permitted the detection of neutrinos with energies above 233.2 keV. This was the first time solar neutrinos from the reaction $p + p \rightarrow d + e^+ + \nu_e$ were detected. At almost the same time and using the same Gallium reaction, the Gallium Experiment

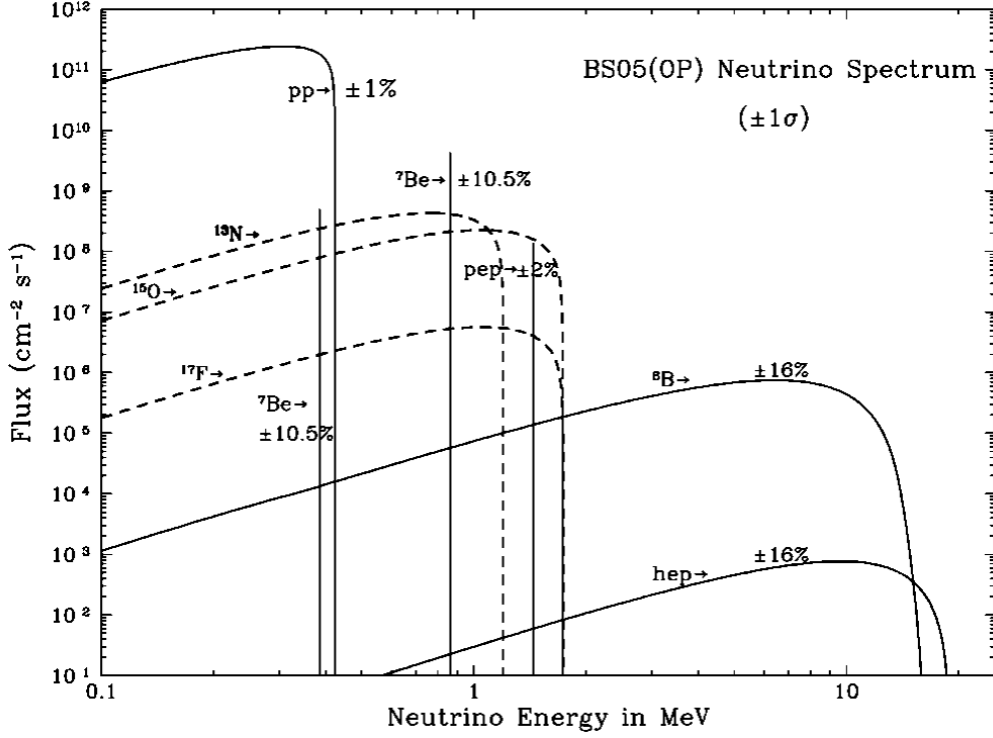


Figure 2.1: Solar neutrino flux from reference [1]. Figure used with permission of the authors and The Astrophysical Journal.

(GALLEX) in the Laboratori Nazionali del Gran Sasso, Italy, confirmed the missing solar neutrinos [94].

In all of these experiments, the neutrino detection mechanism was based only on the electron neutrino reactions. There was no way to determine whether the theoretical calculation of the neutrino emission based on the standard solar model was correct or whether the total neutrino flux ($\nu_e + \nu_\mu + \nu_\tau$) could confirm the standard solar model prediction and the existence of a neutrino mechanism to change flavor beyond the particle standard model. The introduction of new neutrino detectors, such as the Super-Kamiokande Collaboration in Japan and the Sudbury Neutrino Observatory in Canada, changed the landscape, allowing the possibility of detecting electron, muon and tau neutrinos coming from the sun.

The Super-Kamiokande Collaboration used a 50,000 ton detector with water as its neutrino target. Unlike the Homestake, SAGE and Gallex experiments, Super-Kamiokande can detect neutrinos through the scattering of electrons

$$\nu_l + e^- \rightarrow \nu_l + e^-, \quad (\text{Eq. 2.1.8})$$

where l represent electron, muon and tau flavors.

The detection method involved measuring the Cherenkov radiation that water's scattered electrons released. In the measurements, the electron neutrino scattering had 6.5 times more detection efficiency than the muon and tau neutrinos, implying the impossibility of measuring the total solar neutrino flux. Super-Kamiokande was able to measure neutrino energies and momenta above 5 MeV, as below this energy the noise from the background radiation of the earth's beta decay radioisotopes dominated. For this reason, the measurements were sensitive primarily to the Boron-8 neutrinos produced in the sun. It is important to remark that the Super-Kamiokande measure-

ments of the neutrino direction provided clear evidence that the neutrino flux detected came from the sun and they were about half the theoretical prediction [95, 4].

The final experimental evidence of the solar neutrino oscillation came from the Sudbury Neutrino Observatory (SNO). SNO is a 1,000-ton heavy water (D^2O) detector designed to measure both the electron neutrino flux and the total neutrino flux. Heavy water has a special property that allows neutrinos to interact in three different physical processes, each with different sensitivities. Another important property of the SNO experiment is that deuterons in heavy water have a binding energy between protons and neutrons that is lower than the boron-8 neutrino energies emitted by the sun, resulting in kinematically favorable reactions for lower-energy neutrinos.

In the SNO, electron neutrinos interact with deuterons through a charged current reaction to create two protons and one electron

$$\nu_e + d \rightarrow p + p + e^-, \quad (\text{Eq. 2.1.9})$$

this reaction is detected via the Cherenkov radiation emitted by the electron. Due to the high deuteron rest energy in comparison to the incoming neutrino energy, it is not possible to measure the neutrino momentum direction.

At the same time, all neutrinos, independently of flavor, interact with deuterons via the neutral current reaction, emitting a neutron, a proton and a neutrino of the same flavor

$$\nu_l + d \rightarrow n + p + \nu_l, \quad (\text{Eq. 2.1.10})$$

the neutron emitted in this reaction is expected to be captured by a Hydrogen-3 producing Hydrogen-4 and a 6.25 MeV photon

$$n + {}^3\text{H} \rightarrow {}^4\text{H} + \gamma, \quad (\text{Eq. 2.1.11})$$

the high-energy photon interaction with the background matter of the detector will produce relativistic electrons that can be detected via Cherenkov radiation.

Finally, SNO was able to detect the neutrino scattering with electrons as in equation 2.1.8. However, as mentioned before, this process shows more efficiency for the detection of the electron neutrino scattering than the other flavors by approximately 6.5 times. The scattered electron and also the Cherenkov radiation signal will point in the sun's direction as the electron energy is considerably less than the neutrino scattered energy, in this way, it is possible to distinguish the scattering process from the charged current reactions. This, combined with the different energy distribution of the detected Cherenkov photons, made it possible to distinguish between neutrinos from the three interactions mentioned before.

The SNO result showed that the total neutrino flux agreed with the theoretical prediction of the standard solar model

$$\Phi_{\nu_{e\mu\tau}}^{\text{SNO}} = 5.44 \pm 0.99 \times 10^{-6} \text{cm}^{-2}\text{s}^{-1}. \quad (\text{Eq. 2.1.12})$$

Meanwhile, SNO showed that the missing neutrinos correspond to the mu and tau neutrino fluxes

$$\Phi_{\nu_{\mu\tau}}^{\text{SNO}} = 3.69 \pm 1.13 \times 10^{-6} \text{cm}^{-2}\text{s}^{-1}. \quad (\text{Eq. 2.1.13})$$

As there is no reaction in the solar model proton-proton chain that produces muon and tau neutrinos, this was convincing evidence that neutrinos change flavor while traveling from the sun to the earth. Currently, this quantum phenomenon can only be explained if neutrinos acquire a non-zero mass via a mechanism beyond the particle standard model [5].

2.2 Atmospheric neutrinos

Although the precursor of the discovery of the neutrino flavor oscillation was the solar neutrino problem, the first conclusive evidence of this phenomenon came from the Kamiokande Collaboration (precursor of the Super-Kamiokande Collaboration) using measurements of atmospheric neutrinos at the beginning of the 1990s [96, 97, 98].

Atmospheric neutrinos are produced as decay products of hadronic showers (pions and then muons) produced by the collision of high-energy cosmic rays (protons from outer space) with molecules in the upper atmosphere. Neutrinos are produced first by the decay of pions, which also produce muons

$$\pi^+ \rightarrow \mu^+ + \nu_\mu \quad (\text{Eq. 2.2.1})$$

$$\pi^- \rightarrow \mu^- + \bar{\nu}_\mu \quad (\text{Eq. 2.2.2})$$

eventually, muons decay to electrons producing electron and muon neutrinos

$$\mu^+ \rightarrow e^+ + \nu_e + \bar{\nu}_\mu \quad (\text{Eq. 2.2.3})$$

$$\mu^- \rightarrow e^- + \bar{\nu}_e + \nu_\mu. \quad (\text{Eq. 2.2.4})$$

As can be deduced from equations 2.2.1, 2.2.2, 2.2.3 and 2.2.4, the ratio of muon flux ($\nu_\mu + \bar{\nu}_\mu$) to electron flux ($\nu_e + \bar{\nu}_e$) must be equal to two in the case of no flavor transformation. However, the Kamiokande Collaboration found a smaller ratio of muon and electron neutrino and antineutrino flux [96]

$$(\mu/e)_{\text{data}} / (\mu/e)_{\text{MC}} = 0.60_{-0.06}^{+0.07}(\text{stat.}) \pm 0.05(\text{syst.}) \quad (\text{Eq. 2.2.5})$$

where $(\mu/e)_{\text{MC}}$ is the Monte Carlo prediction of muon and electron detections in the case of a 2 :: 1 relation in the muon and electron neutrino and antineutrino flux.

This result strongly suggests that neutrinos changed their flavor while traveling from the atmosphere to the detector. An analysis of the direction of neutrinos led to the conclusion that neutrinos that came directly overhead (traveled around ten kilometers) showed the 2 :: 1 expected flux ratio, but the muon-electron neutrino antineutrino flux ratio decreased as the zenith angle of the incoming neutrinos decreased (the traveled distance increased). In 1998, the Super-Kamiokande Collaboration confirmed and improved these results, confirming the neutrino flavor oscillation phenomenon in atmospheric neutrinos [99].

2.3 Neutrino flavor oscillation in vacuum

Nowadays, it is well known that neutrinos behave in a quantum superposition of flavor (or weak interaction) eigenstates $|\nu_\alpha\rangle$, where $\alpha = e, \mu, \tau$ represents electron, muon and tau flavors, respectively

$$|\nu\rangle = \nu_e |\nu_e\rangle + \nu_\mu |\nu_\mu\rangle + \nu_\tau |\nu_\tau\rangle. \quad (\text{Eq. 2.3.1})$$

Neutrinos(antineutrinos) are produced and detected in flavor eigenstates in charged-current weak interaction processes either in transitions of charged lepton l_α^- to a neutrino ν_α or anti-lepton l_α^+ to an antineutrino $\bar{\nu}_\alpha$; or a creation pair of charged anti-lepton l_α^+ and a neutrino ν_α or lepton l_α^- and an antineutrino $\bar{\nu}_\alpha$, these neutrino production interactions are described by the charged-current weak interaction Lagrangian

$$\mathcal{L}^{CC} = -\frac{g}{2\sqrt{2}} (j^\rho W_\rho + j^{\rho\dagger} W_\rho^\dagger) \quad (\text{Eq. 2.3.2})$$

where $j^\rho = 2\bar{\nu}_\alpha \gamma^\rho l_\alpha$ is the lepton charged current and W_ρ is the charged weak interaction boson coupling term. We assumed the Einstein summation convention. Neutrinos can also be produced in neutral-current weak interactions but are not created in a definite flavor eigenstate [83].

Although neutrinos are detected in flavor eigenstates, neutrinos propagate in the mass eigenstates² solutions to the Dirac equation ν_i [100]

$$(i\cancel{\partial} - m_i)\nu_i = 0. \quad (\text{Eq. 2.3.3})$$

²Unlike flavor eigenstates that are represented with greek subindices ν_α , mass eigenstates will be represented with Latin subindices ν_i .

These states have well defined non-degenerate non-zero masses m_i , where $i = 1, 2, 3$ (see chapter 2 of reference [83] for a discussion of the Dirac equation's solutions). The Fourier expansion of the Dirac field operator ν_i will be given by

$$\nu_i(x) = \int \frac{d^3p}{(2\pi)^3 2E} \sum_{h=\pm 1} \left[a_{\nu_i}^{(h)}(p) u_{\nu_i}^{(h)}(p) e^{-ip \cdot x} + b_{\nu_i}^{(h)\dagger}(p) v_{\nu_i}^{(h)}(p) e^{ip \cdot x} \right] \quad (\text{Eq. 2.3.4})$$

where $a_{\nu_i}^{(h)}(p)$ and $b_{\nu_i}^{(h)\dagger}(p)$ are the neutrino annihilation and antineutrino creation operators and $u_{\nu_i}^{(h)}(p)$ and $v_{\nu_i}^{(h)}(p)$ are the Dirac spinors that depend on the used γ matrix representation.

The relationship between the mass ν_i and flavor basis ν_α is given, in analogy to the quark mixing [101, 102] by the Pontecorvo-Maki-Nakagawa-Sakata (PMNS) unitary mixing matrix [103]

$$\nu_\alpha = \sum_i U_{\alpha i}^\dagger \nu_i \quad (\text{Eq. 2.3.5})$$

The PMNS mixing matrix takes the form

$$U = \begin{pmatrix} 1 & 0 & 0 \\ 0 & c_{23} & s_{23} \\ 0 & -s_{23} & c_{23} \end{pmatrix} \begin{pmatrix} c_{13} & 0 & s_{13} e^{-i\delta_{cp}} \\ 0 & 1 & 0 \\ -s_{13} e^{i\delta_{cp}} & 0 & c_{13} \end{pmatrix} \begin{pmatrix} c_{12} & s_{12} & 0 \\ -s_{12} & c_{12} & 0 \\ 0 & 0 & 1 \end{pmatrix} \quad (\text{Eq. 2.3.6})$$

where $c_{ij} = \cos(\theta_{ij})$ and $s_{ij} = \sin(\theta_{ij})$, $\theta_{ij} = \theta_{12}, \theta_{13}, \theta_{23}$ are the three mixing angles and δ_{cp} is the charge parity violation phase. Current measurements show that [103]

$$\left. \begin{aligned} \sin^2 \theta_{12}/10^{-1} &= 3.11_{-0.17}^{+0.15} \\ \sin^2 \theta_{23}/10^{-1} &= 5.59_{-0.26}^{+0.10} \\ \sin^2 \theta_{13}/10^{-2} &= 2.230_{-0.069}^{+0.072} \\ \delta_{cp}^\circ &= 274_{-26}^{+24} \end{aligned} \right\} \text{Inverted mass ordering} \quad (\text{Eq. 2.3.7})$$

$$\left. \begin{aligned} \sin^2 \theta_{12}/10^{-1} &= 3.11_{-0.13}^{+0.15} \\ \sin^2 \theta_{23}/10^{-1} &= 5.55_{-0.42}^{+0.19} \\ \sin^2 \theta_{13}/10^{-2} &= 2.195_{-0.067}^{+0.076} \\ \delta_{cp}^\circ &= 225_{-29}^{+39} \end{aligned} \right\} \text{Normal mass ordering.} \quad (\text{Eq. 2.3.8})$$

Inverse and normal mass ordering makes reference to the still undetermined question of whether the ν_3 neutrino mass eigenstate is lighter or heavier than the ν_1 and ν_2 mass eigenstates [104]

$$\text{Normal mass ordering} \rightarrow m_3 > m_2 > m_1 \quad (\text{Eq. 2.3.9})$$

$$\text{Inverted mass ordering} \rightarrow m_2 > m_1 > m_3. \quad (\text{Eq. 2.3.10})$$

To describe the neutrino flavor evolution, it is convenient to express the neutrino flavor state as a density matrix

$$\rho = |\nu\rangle \langle \nu|, \quad (\text{Eq. 2.3.11})$$

the diagonal element of the density matrix ρ_{aa} represent the probability of finding the particle in flavor a , the off diagonal element ρ_{ab} is the amount of flavors a and b mixing. Using natural units ($\hbar = c = 1$), as in all this chapter, the evolution of the neutrino flavor density matrix is given by the Schrodinger equation

$$\frac{\partial \rho}{\partial t} = -i [H, \rho] \quad (\text{Eq. 2.3.12})$$

where H is the neutrino Hamiltonian, which contains the sum of the vacuum, neutrino-matter and neutrino-neutrino interaction Hamiltonians:

$$H = H_{\text{vacuum}} + H_{\text{matter}} + H_{\text{neutrino}}. \quad (\text{Eq. 2.3.13})$$

In this section, I will discuss the flavor dynamics under the neutrino vacuum Hamiltonian. The neutrino-matter and neutrino-neutrino interaction Hamiltonians are postponed to sections 2.4 and 2.5 respectively.

In the absence of background matter, the evolution of neutrino flavor states is determined by the neutrino vacuum Hamiltonian. It can be expressed in the flavor basis as a unitary PMNS transformation of the neutrino vacuum Hamiltonian in the mass basis. The vacuum Hamiltonian in the mass basis is

$$H_{\text{vacuum,ab}} = E_a \delta_{ab} = \sqrt{\mathbf{p}^2 + m_a^2} \delta_{ab} \approx |\mathbf{p}| + \frac{m_a^2 \delta_{ab}}{2|\mathbf{p}|}, \quad (\text{Eq. 2.3.14})$$

the approximation in the equation 2.3.14 holds for $|\mathbf{p}| \gg m_a$, and is valid because the neutrino masses are limited to $m_{\text{tot}} = \sum_{\nu} m_{\nu} < 11 \text{ eV}$ [103], and the typical neutrino energies in supernovae and neutron star mergers are $\sim 10 \text{ MeV}$ [105, 106].

It is possible to add a constant term to the Hamiltonian without affecting the equation of motion. Adding $-|\mathbf{p}| - m_1^2/2|\mathbf{p}|$ and considering $E \approx |\mathbf{p}|$ that comes from the condition $|\mathbf{p}| \gg m_i$, the vacuum Hamiltonian in flavor basis becomes

$$H_{\text{vacuum}} = \frac{1}{2E} U \begin{pmatrix} 0 & 0 & 0 \\ 0 & \Delta m_{21}^2 & 0 \\ 0 & 0 & \Delta m_{31}^2 \end{pmatrix} U^\dagger, \quad (\text{Eq. 2.3.15})$$

where $\Delta m_{ij}^2 = m_i^2 - m_j^2$. Current measurements show that [103]

$$\left. \begin{aligned} \Delta m_{21}^2 &= 7.42^+ (10^{-5} \text{ eV}^2) \\ \Delta m_{32}^2 &= -2.500_{-0.032}^{+0.034} (10^{-3} \text{ eV}^2) \end{aligned} \right\} \text{Inverted mass ordering} \quad (\text{Eq. 2.3.16})$$

$$\left. \begin{aligned} \Delta m_{21}^2 &= 7.42_{-0.18}^{+0.20} (10^{-5} \text{ eV}^2) \\ \Delta m_{32}^2 &= 2.4367_{-0.032}^{+0.032} (10^{-3} \text{ eV}^2) \end{aligned} \right\} \text{Normal mass ordering,} \quad (\text{Eq. 2.3.17})$$

and

$$\Delta m_{31}^2 = \Delta m_{32}^2 + \Delta m_{21}^2 \quad (\text{Eq. 2.3.18})$$

Using the equations 2.3.15 and 2.3.14 it is possible to evolve the flavor state of a neutrino in vacuum. Actually, this equation admits an analytical solution. For solving them, it is better to start with the Schrodinger equation of a single neutrino state on the mass basis

$$i\partial_t |\nu\rangle = \hat{H}_{\text{vacuum}} |\nu\rangle = E |\nu\rangle = \sqrt{p^2 + m^2} |\nu\rangle \quad (\text{Eq. 2.3.19})$$

the solution to this equation are plane waves

$$|\nu(t)\rangle = e^{-iEt} |\nu\rangle, \quad (\text{Eq. 2.3.20})$$

in the next procedure I will continue assuming the neutrino wave function can be described by a plane wave; this approximation leads to the right answer, but some arguable assumptions will be made in the process. Even so, this procedure is widely considered in the neutrino literature as a standard procedure. The neutrino solution considers a wave packet treatment that leads to the same answer with fewer assumptions. This can be found in Chapter 8 of reference [83].

To continue, we are going to impose that the initial state of the neutrinos in equation 2.3.20 is a pure $|\nu_\alpha\rangle$ flavor eigenstate. Using equation 2.3.5 this result in

$$|\nu(t=0)\rangle = |\nu\rangle = |\nu_\alpha\rangle = \sum_i U_{\alpha i}^\dagger \nu_i, \quad (\text{Eq. 2.3.21})$$

in substituting equation 2.3.21 in equation 2.3.20 we get

$$|\nu_\alpha(t)\rangle = \sum_i e^{-iE_i t} U_{\alpha i}^\dagger \nu_i, \quad (\text{Eq. 2.3.22})$$

changing the basis of equation 2.3.22 from the mass basis $|\nu_i\rangle$ to the flavor basis $|\nu_\beta\rangle$ using the relation $|\nu_i\rangle = \sum_\beta U_{i\beta} |\nu_\beta\rangle$ we obtain

$$|\nu_\alpha(t)\rangle = \sum_i \sum_\beta e^{-iE_i t} U_{\alpha i}^\dagger U_{i\beta} |\nu_\beta\rangle. \quad (\text{Eq. 2.3.23})$$

The probability of measuring a neutrino initially emitted at flavor $|\nu_\alpha\rangle$ at flavor $|\nu_\zeta\rangle$ at a time t will be given by

$$P_{\nu_\alpha \rightarrow \nu_\zeta}(t) = \langle \nu_\zeta | \nu_\alpha(t) \rangle^2, \quad (\text{Eq. 2.3.24})$$

substituting equation 2.3.23 in 2.3.24 we get

$$P_{\nu_\alpha \rightarrow \nu_\zeta}(t) = \left(\sum_i \sum_\beta e^{-iE_i t} U_{\alpha i}^\dagger U_{i\beta} \langle \nu_\zeta | \nu_\beta \rangle \right)^2, \quad (\text{Eq. 2.3.25})$$

using the normalization relationship $\langle \nu_\zeta | \nu_\beta \rangle = \delta_{\zeta\beta}$, where $\delta_{\zeta\beta}$ is the Kronecker delta, and developing the square, we obtain

$$P_{\nu_\alpha \rightarrow \nu_\beta}(t) = \sum_{ij} U_{\alpha i}^\dagger U_{i\beta} U_{\alpha j} U_{j\beta}^\dagger e^{-i(E_i - E_j)t}. \quad (\text{Eq. 2.3.26})$$

As can be seen in the last equation, the probability depends on the energies of the $|\nu_i\rangle$ and $|\nu_j\rangle$ mass eigenstates. Neutrinos while traveling do not have definite energy, mass and momentum because they are a linear combination of mass eigenstate with definite energy, mass and momentum in the plane wave approximation assumed.

We can approximate $E_i - E_j$ assuming the mass eigenstates $|\nu_i\rangle$ and $|\nu_j\rangle$ have both the same momentum $p_i = p_j = p$ and the neutrino has a definite energy E in the flavor state.

With these assumptions, and considering the limit when $p \gg m_i$ and m_j , we obtain that

$$E_i = \sqrt{p^2 + m_i^2} \approx p + \frac{m_i^2}{2p} \approx E + \frac{m_i^2}{2E} \quad (\text{Eq. 2.3.27})$$

$$E_j = \sqrt{p^2 + m_j^2} \approx p + \frac{m_j^2}{2p} \approx E + \frac{m_j^2}{2E}, \quad (\text{Eq. 2.3.28})$$

and therefore

$$E_i - E_j \approx \frac{\Delta m_{ij}^2}{2E} \quad (\text{Eq. 2.3.29})$$

with $\Delta m_{ij}^2 = m_i^2 - m_j^2$. With this, the probability that a neutrino emitted in the flavor eigenstate $|\nu_\alpha\rangle$ will be detected at the flavor eigenstate $|\nu_\beta\rangle$ at a time t will be given by

$$P_{\nu_\alpha \rightarrow \nu_\beta}(t) = \sum_{ij} U_{\alpha i}^\dagger U_{i\beta} U_{\alpha j} U_{j\beta}^\dagger e^{-i(\Delta m_{ij}^2/2E)t}. \quad (\text{Eq. 2.3.30})$$

In Figure 2.2 I show the behavior of equation 2.3.30 for the mixing angles and the mass square differences in equations 2.3.7, 2.3.8, 2.3.16 and 2.3.17. The neutrino there carries an energy of 50 GeV. This figure represents the evolution of the state of a neutrino emitted in an electron state

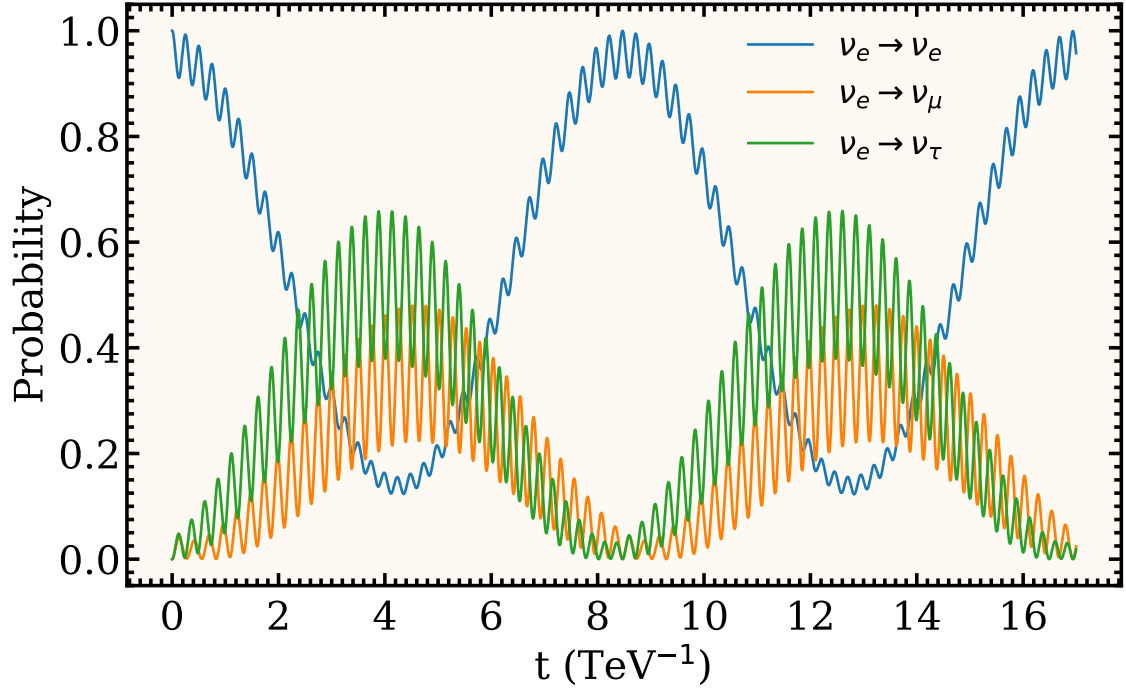


Figure 2.2: Flavor oscillation in vacuum for a neutrino initially emitted in a pure electron flavor state. The blue, green and orange lines represent the probability to detect the neutrino in electron, muon and tau flavor states, respectively. The mixing matrix was characterized by the mixing angles $\sin^2 \theta_{12}/10^{-1} = 3.11$, $\sin^2 \theta_{23}/10^{-1} = 5.55$ and $\sin^2 \theta_{13}/10^{-2} = 2.195$. The mass square differences are $\Delta m_{21}^2 = 7.42 (10^{-5} \text{ eV}^2)$, $\Delta m_{32}^2 = 2.4367 (10^{-3} \text{ eV}^2)$ and $\Delta m_{31}^2 = \Delta m_{32}^2 + \Delta m_{21}^2$. The neutrino energy is 50 GeV. Natural units were considered.

traveling in vacuum. The blue line is the probability of detecting the neutrino in electron states, the green and orange lines represent the probability of detecting the neutrino in mu and tau flavors, respectively.

For the reduced case of two flavors (e and x), the mixing matrix U in equation 2.3.30 can be simplified to a two-by-two matrix that depends on a single angle

$$U = \begin{pmatrix} \cos \theta & \sin \theta \\ -\sin \theta & \cos \theta \end{pmatrix}. \quad (\text{Eq. 2.3.31})$$

The probability that a neutrino emitted in electron flavor would be detected in the flavor x will be given by the following equation:

$$P_{\nu_e \rightarrow \nu_x}(t) = 1 - \sin^2 2\theta \sin^2 \frac{\Delta m^2}{4E} t, \quad (\text{Eq. 2.3.32})$$

in the same way, the probability that a neutrino emitted in the electron flavor would be detected in the electron flavor will be given as follows:

$$P_{\nu_e \rightarrow \nu_e}(t) = 1 - P_{\nu_e \rightarrow \nu_x}(t) = \sin^2 2\theta \sin^2 \frac{\Delta m^2}{4E} t. \quad (\text{Eq. 2.3.33})$$

In the solid line of Figure 2.4 I show the vacuum neutrino behavior in equations 2.4.28 and 2.4.29 for a mixing angle of $\theta = 25^\circ$, a mass square difference of $\Delta m^2 = 7.42 (10^{-5} \text{ eV}^2)$ and a neutrino energy of 50 GeV.

2.4 Neutrino-matter interaction (MSW effect)

Even before the experimental discovery of the neutrino vacuum oscillations due to neutrino mass, flavor transformation due to coherent forward neutrino scattering³ with matter, which had already been studied by Mikheyev, Smirnov and Wolfenstein (MSW effect) as a solution to the solar neutrino problem [6, 7]. Potentials caused by the coherent forward scattering of ultrarelativistic neutrinos with matter can reach or greatly exceed the vacuum oscillation potential, leading to sizable neutrino matter flavor oscillation [85].

Flavor transformation due to neutrino incoherent scattering cross-section in terrestrial applications is so small that incoherent scattering effects can be ignored. Following reference [83] we can easily estimate the order of magnitude of the mean free path due to incoherent scatterings. The cross-section of an incoherent scattering of a neutrino with a charged lepton is of the order of

$$\sigma \sim G_F s, \quad (\text{Eq. 2.4.1})$$

where G_F is the Fermi constant and s is the Lorentz invariant Mandelstam variable which in the center-of-mass frame represents the square of the total energy. In the laboratory reference frame where the target particle with mass m is at rest, the Mandelstam variable s is given by

$$s = 2Em, \quad (\text{Eq. 2.4.2})$$

where E is the neutrino energy.

The mean free path of a neutrino in a homogeneous medium with a target number density of N is given by

$$l \sim \frac{1}{N\sigma} \sim \frac{1}{2NG_F Em}. \quad (\text{Eq. 2.4.3})$$

For solar neutrino energies of 1 MeV the mean free path in ordinary matter $N = 10^{24} \text{ cm}^{-3}$ in a background of target particles with masses of around 1 GeV is of the order of 10^{17} cm . This is small enough to ignore incoherent neutrino scattering effects. However, in stellar explosive events like core-collapse supernovae or neutron star mergers, the neutrino's energy and background matter densities are high enough to consider the neutrino incoherent scattering. Neutrinos play a crucial role in the dynamics of these systems. Neutrinos with energies of around 10 MeV and matter densities near the $10^{12} N_A \text{ cm}^{-3}$ (N_A is the Avogadro number) lead to a neutrino mean free path around a few thousand meters. Neutrino incoherent scattering effects in explosive stellar events is still an active research field [107, 108, 109, 70, 110]. However, in the next paragraphs and the rest of this thesis, I will focus on the coherent neutrino forward scattering.

Neglecting gravity, neutrino interactions with matter are restricted to weak interactions via neutral and charged currents. In the next paragraphs, I will first discuss the charged current interaction of electron neutrinos with background electrons, as this is the most important flavor-changing neutrino interaction with the background particles in astrophysical systems. The charged current interaction of muon and tau neutrinos with muons and tau, respectively, is easily generalized; however, it does not play a crucial role in the flavor transformation of neutrinos since particle energies in those systems are not high enough to create significant amounts of muons and taus. The background media in explosive stellar events are predominantly composed of neutrons and an equal number of electrons and protons. I will also consider the neutral current interaction of neutrinos mediated by the Z boson. It will become evident that this interaction does not affect the flavor evolution as it contributes to all the neutrinos flavors equally.

In Figure 2.3a I show the Feynman diagram of the coherent forward scattering of an electron neutrino with an electron via the exchange of a charged W boson. Although charged current

³Coherent forward neutrino scattering makes reference to interactions in which the neutrino energy and momentum do not change. On the other hand, incoherent scattering refers to an interaction in which energy and momentum are transferred between the particles involved, e.g., Compton scattering.

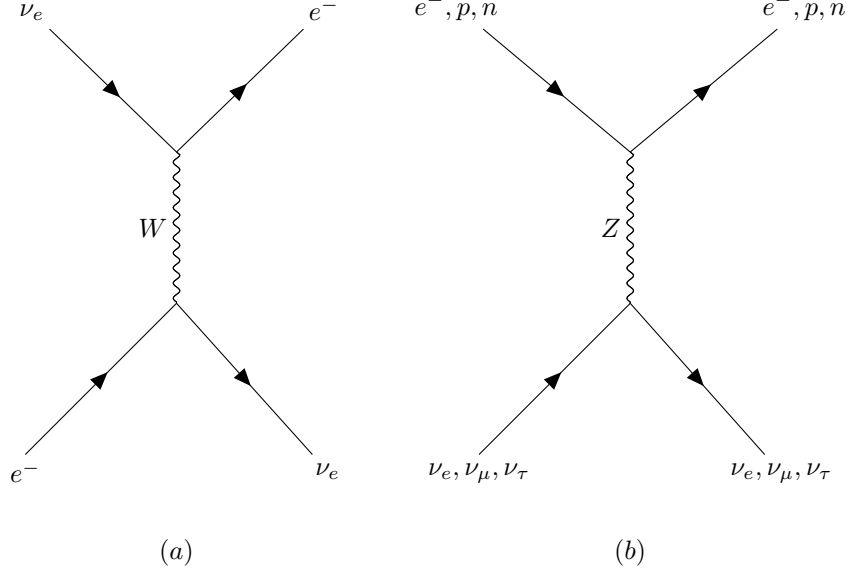


Figure 2.3: Feynman diagrams depicting (a) the coherent forward elastic scattering process due to the weak charged current interaction of electron neutrinos with background electrons via the exchange of a W boson. (b) shows the elastic scattering process of neutrinos with background matter by the weak neutral current interaction via the exchange of a Z boson.

interactions are in general described by the Lagrangian in equation 2.3.2, in most astrophysical systems the particles energy is smaller than the masses of the W and Z gauge bosons (100 GeV). For this reason, the interaction can be described by an effective low energy charged current Lagrangian and the gauge boson propagator can be simplified to a point in the Feynman diagram. This corresponds to the following Lagrangian

$$\mathcal{L}_{\text{eff}}^{CC} = -\frac{G_F}{\sqrt{2}} j_W^\dagger j_W^\rho \quad (\text{Eq. 2.4.4})$$

where j_W^ρ is the leptonic charged-current

$$j_W^\rho = 2 \sum_{\alpha=e,\mu,\tau} \bar{\nu}_\alpha \gamma^\rho (1 - \gamma^5) l_\alpha. \quad (\text{Eq. 2.4.5})$$

For background matter mostly composed of electrons, the leptonic charged current is reduced to

$$j_W^\rho = 2\bar{\nu}_e \gamma^\rho (1 - \gamma^5) e. \quad (\text{Eq. 2.4.6})$$

The Hamiltonian corresponding to the Lagrangian in equation 2.4.4 considering only the leptonic charged-current due to electrons in equation 2.4.6 takes the form

$$\mathcal{H}_{\text{eff}}^{CC} = -\frac{G_F}{\sqrt{2}} [\bar{\nu}_e \gamma^\rho (1 - \gamma^5) e] [\bar{e} \gamma_\rho (1 - \gamma^5) \nu_e]. \quad (\text{Eq. 2.4.7})$$

The average of the effective Hamiltonian over a homogeneous electron background in the rest frame of the medium is given by

$$\langle \mathcal{H} \rangle_{\text{eff}}^{CC} = V_e^{CC} [\bar{\nu}_e \gamma^0 \nu_e] \quad (\text{Eq. 2.4.8})$$

where V_{cc} has the form

$$V_e^{CC} = 2\sqrt{2}G_F\gamma^\rho [\bar{e}\gamma_\rho (1 - \gamma^5) e] = \sqrt{2}G_F n_e, \quad (\text{Eq. 2.4.9})$$

and n_e is the electron number density of the medium.

This can be generalized to include muon and tau charged currents as follows:

$$V_{\alpha\beta}^{CC} = \sqrt{2}G_F n_\alpha \delta_{\alpha\beta} \quad (\text{Eq. 2.4.10})$$

where α and β represent the e , μ and τ flavors.

On the other hand, the neutrino interaction with matter via the neutral current reactions in Figure 2.3b is described by the weak neutral current Lagrangian interaction

$$\mathcal{L}_{\text{eff}}^{NC} = -\frac{G_F}{\sqrt{2}} j_Z^\mu j_{Z\mu} \quad (\text{Eq. 2.4.11})$$

where j_Z^μ represents the sum of the lepton j_{Zl}^μ and quark j_{Zq}^μ neutral currents.

The effective Hamiltonian of the interaction in Figure 2.3b from the Lagrangian in equation 2.4.11 is given as follows:

$$\mathcal{H}_{\text{eff}}^{NC} = -\frac{G_F}{\sqrt{2}} \sum_{\alpha=e,\mu,\tau} [\bar{\nu}_\alpha \gamma^\rho (1 - \gamma^5) \nu_\alpha] \sum_f [\bar{f} \gamma_\rho (g_V^f - g_A^f) f], \quad (\text{Eq. 2.4.12})$$

the potential related to this Hamiltonian in the following equation

$$\langle \mathcal{H} \rangle_{\text{eff}}^{NC} = \sum_{\alpha=e,\mu,\tau} V_\alpha^{NC} [\bar{\nu}_\alpha \gamma^0 \nu_\alpha] \quad (\text{Eq. 2.4.13})$$

takes the form

$$V_\alpha^{NC} = \sqrt{2}G_F\gamma^\rho \sum_f [\bar{f} \gamma_\rho (g_V^f - g_A^f) f] = \sqrt{2}G_F \sum_f n_f g_V^f, \quad (\text{Eq. 2.4.14})$$

where for electrons, protons and neutrons, the coefficients g_V^f are

$$g_V^e = -\frac{1}{2} + 2\sin^2 \theta_W \quad (\text{Eq. 2.4.15})$$

$$g_V^p = 2g_V^u + g_V^d = \frac{1}{2} - 2\sin^2 \theta_W \quad (\text{Eq. 2.4.16})$$

$$g_V^n = g_V^u + 2g_V^d = -\frac{1}{2} \quad (\text{Eq. 2.4.17})$$

where θ_W is the Weinberg angle and u and d represent up and down quarks respectively.

As it is evident from the values of g_V^e and g_V^p in equation 2.4.15 and 2.4.16, the electron and proton contributions to the neutral current potential cancel each other in a neutral electric background. The neutral current will be a function only of the neutron number density and will be the same for all neutrino flavors

$$V^{NC} = -\frac{\sqrt{2}}{2} G_F n_n \mathbf{I}. \quad (\text{Eq. 2.4.18})$$

Summarizing, the neutrino potential due to coherent forward scattering with matter will be given by

$$V_{\text{matter}} = V^{CC} + V^{NC}. \quad (\text{Eq. 2.4.19})$$

This is the matter Hamiltonian of the neutrino flavor

$$H_{\text{matter}} = \sqrt{2}G_F \begin{pmatrix} n_e & 0 & 0 \\ 0 & n_\mu & 0 \\ 0 & 0 & n_\tau \end{pmatrix} - \frac{\sqrt{2}}{2}G_F \begin{pmatrix} n_n & 0 & 0 \\ 0 & n_n & 0 \\ 0 & 0 & n_n \end{pmatrix}. \quad (\text{Eq. 2.4.20})$$

As motioned before, the second term in the matter Hamiltonian in the equation 2.4.20 due to the neutral current interaction ($-\sqrt{2}G_F n_n/2\mathbf{I}$) does not affect the density matrix evolution, since the potential is the same for all the flavors of neutrinos and it will be canceled in the commutator term of equation 2.3.12.

To study the evolution of the neutrino flavor while traveling in matter, it is convenient to consider the two flavor case. I will consider a background medium composed of a constant electron number density in which there are no muons or tau.

For two flavors, the vacuum Hamiltonian in the flavor basis in equation 2.3.15 can be written as

$$H_{\text{vacuum}} = \frac{1}{2E}U \begin{pmatrix} 0 & 0 \\ 0 & \Delta m^2 \end{pmatrix} U^\dagger, \quad (\text{Eq. 2.4.21})$$

where U is the mixing matrix in equation 2.3.31. After doing the matrix multiplication in the equation 2.4.21 the resultant vacuum Hamiltonian is

$$H_{\text{vacuum}} = \frac{\Delta m^2}{4E} \begin{pmatrix} -\cos 2\theta & \sin 2\theta \\ \sin 2\theta & \cos 2\theta \end{pmatrix} + \frac{\mathbf{I}}{2}, \quad (\text{Eq. 2.4.22})$$

where the second term can be neglected because a diagonal matrix commutes with all matrices and will have no effect on the commutator of the neutrino flavor evolution in equation 2.3.12.

The solutions to the Hamiltonian in equation 2.4.22 can be observed in equations 2.3.32 and 2.3.33.

To include the matter's effects I will sum equation 2.4.20 to the vacuum Hamiltonian in equation 2.4.22. I will set $n_x = 0$. This resulted in

$$H_{\text{v\&m}} = \frac{\Delta m^2}{4E} \begin{pmatrix} -\cos 2\theta & \sin 2\theta \\ \sin 2\theta & \cos 2\theta \end{pmatrix} + \sqrt{2}G_F \begin{pmatrix} n_e & 0 \\ 0 & 0 \end{pmatrix}, \quad (\text{Eq. 2.4.23})$$

the addition of a diagonal term $-\sqrt{2}G_F n_e/2\mathbf{I}$ in the Hamiltonian in equation 2.4.23 will not affect the evolution of the neutrino flavor. This will result in

$$H_{\text{v\&m}} = \frac{\Delta m^2}{4E} \begin{pmatrix} -\cos 2\theta & \sin 2\theta \\ \sin 2\theta & \cos 2\theta \end{pmatrix} + \frac{\sqrt{2}}{2}G_F \begin{pmatrix} n_e & 0 \\ 0 & -n_e \end{pmatrix}, \quad (\text{Eq. 2.4.24})$$

which can be written as follows:

$$H_{\text{v\&m}} = \frac{\Delta m^2}{4E} \begin{pmatrix} -\cos 2\theta + A_{CC} & \sin 2\theta \\ \sin 2\theta & \cos 2\theta - A_{CC} \end{pmatrix}, \quad (\text{Eq. 2.4.25})$$

where $A_{CC} = 2\sqrt{2}EG_F n_e/\Delta m^2$.

The Hamiltonian in equation 2.4.25 can be diagonalized to the form

$$H_{\text{v\&m}} = \frac{1}{4E} \begin{pmatrix} -\Delta m_M^2 & 0 \\ 0 & \Delta m_M^2 \end{pmatrix} \quad (\text{Eq. 2.4.26})$$

via a unitary transformation with the following unitary matrix

$$U_M = \begin{pmatrix} \cos \theta_M & \sin \theta_M \\ -\sin \theta_M & \cos \theta_M \end{pmatrix} \quad (\text{Eq. 2.4.27})$$

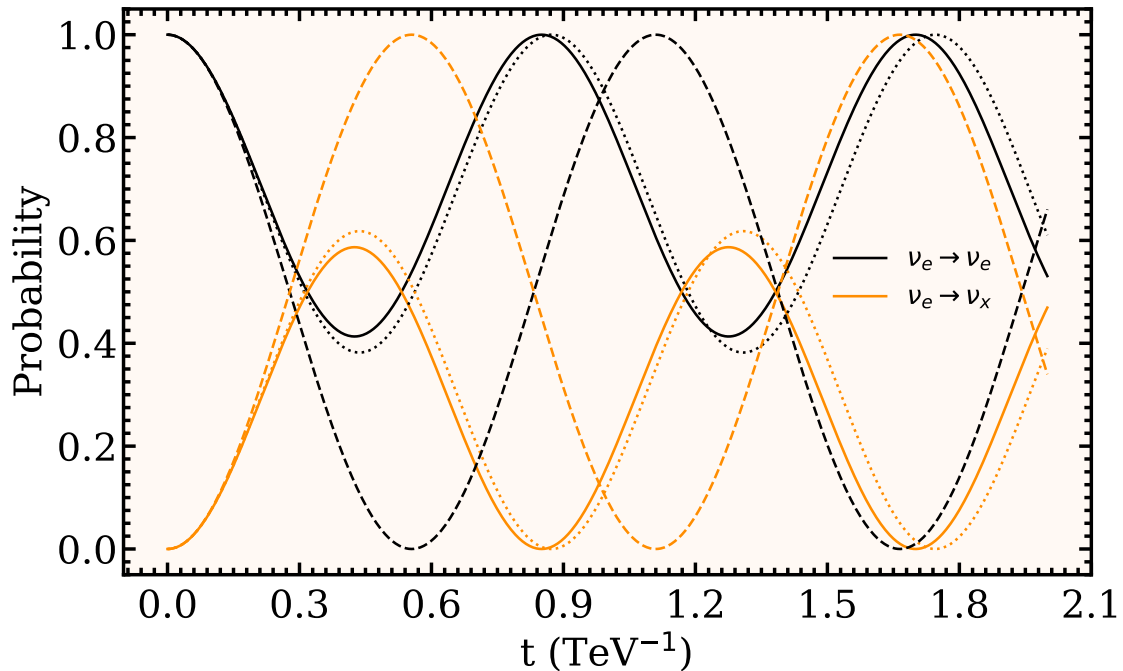


Figure 2.4: Flavor oscillation in vacuum (solid line), matter (dotted line) and resonance (dashed line) for a neutrino initially emitted in a pure electron flavor state. The black and orange lines represent the probability to detect the neutrino in electron and $x = \mu + \tau$ flavor states, respectively. The two-flavor mixing matrix was characterized by a mixing angle of $\theta = 25^\circ$. The mass square difference is $\Delta m^2 = 7.42 (10^{-5} \text{ eV}^2)$. The neutrino energy is 50 GeV. Natural units were considered. The number density of electrons in the background medium was established so that $A_{CC} = 2\sqrt{2}EG_F n_e / \Delta m^2 = 1 \times 10^{-6}$. The resonance is achieved by setting $A_{CC} = \Delta m^2 \cos 2\theta$.

where

$$\Delta m_M^2 = \sqrt{(\Delta m^2 \cos 2\theta - A_{CC})^2 + (\Delta m^2 \sin 2\theta)^2} \quad (\text{Eq. 2.4.28})$$

$$\tan 2\theta_M = \tan 2\theta \cdot \left(1 - \frac{A_{CC}}{\Delta m^2 \cos 2\theta}\right)^{-1}. \quad (\text{Eq. 2.4.29})$$

We can conclude that the neutrino oscillation in matter has the same form as the vacuum neutrino oscillation with an effective mixing angle and square mass difference as shown in equations 2.3.32 and 2.3.33. In the solid line of Figure 2.4 I show the vacuum neutrino behavior in equations 2.4.28 and 2.4.29 for a mixing angle of $\theta = 25^\circ$, a mass square difference of $\Delta m^2 = 7.42 (10^{-5} \text{ eV}^2)$ and a neutrino energy of 50 GeV. The effect of the neutrino-matter coherent interaction in the flavor oscillation can be observed in the dotted lines for $A_{CC} = 2\sqrt{2}EG_F n_e / \Delta m^2 = 1 \times 10^{-6}$. It can be noted that the background matter acts as an index of refraction in the oscillation, modifying the amplitude and frequency of the oscillation.

Another important behavior of neutrinos in matter can be obtained from an analysis of the equation 2.4.29. It can be observed that when $A_{CC} = \Delta m^2 \cos 2\theta$ the system will experience resonance. This corresponds to a neutrino number density of $n_e = \Delta m^2 \cos 2\theta (2\sqrt{2}EG_F)^{-1}$. The effective mass square difference will reach its minimum value at the resonance $\Delta m_M^2 = \Delta m^2 \sin 2\theta$

and the mixing angle will reach its maximum value $\theta_M = \pi/4$. It is necessary to clarify that a requirement for resonance is that the vacuum mixing angle satisfy the following relation: $\cos 2\theta > 0$. In Figure 2.4 the dashed line describes resonance in the neutrino flavor oscillation due to the coherent forward scattering with background electrons.

2.5 Neutrino-neutrino interaction

In addition to vacuum and matter effects, the standard model neutral weak interaction potential allows neutrinos to interact pairwise exchanging virtual Z bosons

$$H_{\nu\nu} = \frac{G_f}{\sqrt{2}} \sum_{\alpha\beta} \bar{\nu}_\beta \gamma^\mu \nu_\beta \bar{\nu}_\alpha \gamma_\mu \nu_\alpha, \quad (\text{Eq. 2.5.1})$$

where α and β run over the neutrino flavors. This Hamiltonian allows the neutrino flavor transformation via neutrino-neutrino coherent forward scattering interaction (also called neutrino self-interaction).

The neutrino flavor transformation due to the coherent forward scattering of neutrinos has seen decades of progress (see [8, 9, 10, 47] for recent reviews) and is still an active research field, considered one of the most challenging open problems in neutrino physics not only from a theoretical point of view but also for its phenomenological implications in astrophysics and cosmology [55].

Unlike vacuum and matter effects, the neutrino-neutrino interaction can lead to plenty of non-linear phenomena. Fast flavor conversions have recently been hypothesized to be crucial in dense neutrino astrophysical environments. Core-collapse supernovae and neutron star mergers are the only places in the universe after the big bang where neutrinos are produced at sufficiently high densities that they are not only temporarily confined by dense matter, but they interact and scatter between them in a way that drives a rich variety of complex non-linear effects [11].

In contrast with slow flavor conversion, in which the spacial scale of the oscillation is in the order of the kilometers [111], fast flavor conversion occurs on spatial and time scales of a few centimeters and nanoseconds [62, 11].

To properly treat the neutrino-neutrino coherent forward scattering in dense neutrino environments in the mean field approximation (neglecting quantum many body effects), the neutrino flavor field needs to be represented by a $N_f \times N_f$ matrix distribution function $f(\vec{x}, \vec{p}, t)$ that depends on the spatial coordinates \vec{x} , momentum \vec{p} and time t . The elements of the distribution function are the expectation values of the bilinear creation and annihilation operators $\langle a_i^\dagger a_j \rangle$, in which the diagonal terms ($i = j$) represent the neutrino occupation numbers of each neutrino species, and the off-diagonal term ($i \neq j$) represents the flavor correlation [47, 50].

The neutrino transport equation (a generalization of equation 2.3.12 that includes the change in position and the momentum exchange of neutrinos) in terms of the flavor distribution function is given by

$$\left(\frac{\partial}{\partial t} + \vec{x} \cdot \vec{\nabla}_x + \vec{p} \cdot \vec{\nabla}_p \right) f(\vec{x}, \vec{p}, t) = -i[H, f(\vec{x}, \vec{p}, t)] + C. \quad (\text{Eq. 2.5.2})$$

where H has the same form as in equation 2.3.13 and C is the collision matrix that includes the incoherent interaction effects. The flavor transformation including the collision matrix is out of the scope of this work as collisions occur over longer length and time scales than flavor transformation (see [112, 110, 70] for recent investigations).

The Hamiltonian of the neutrino-neutrino coherent forward scattering interaction for a neutrino field distribution $f(\vec{x}, \vec{p}', t)$ can be expressed as follows,

$$H_{\text{neutrino}} = \sqrt{2}G_F \int d\vec{p}' \left(f(\vec{x}, \vec{p}', t) - \bar{f}^*(\vec{x}, \vec{p}', t) \right) \left(1 - \vec{v} \cdot \vec{v}' \right) \quad (\text{Eq. 2.5.3})$$

where the bar denotes antineutrino quantities

The neutrino-neutrino coherent forward scattering Hamiltonian has important properties that make it different from other flavor transformation mechanisms. It does not depend on the neutrino and antineutrino energy distributions and is independent of the neutrino masses and mass hierarchy. It is highly dependent on the neutrino and antineutrino angular distributions and is non-linear. The non-linearity of the Hamiltonian makes its application in real environments extremely complicated. A usual technique to grasp the behavior of a neutrino system when the neutrino-neutrino interaction is important is the linear stability analysis. Linear stability analysis can be used to predict whether a neutrino distributions will exhibit flavor instabilities.

In the next paragraphs, I will consider a highly dense neutrino gas

$$\mu \gg \omega_{\text{vacuum}} = \Delta m_{ij}^2 / 2E, \quad (\text{Eq. 2.5.4})$$

in which the vacuum and matter effects are negligible.

To analyze the instability of a neutrino and antineutrino distribution via a linear stability analysis, it is necessary to consider only the linear regime of the transport equation (Eq. 2.5.2). This can be achieved by linearizing the distribution function matrix. In the two-flavor case of e and $x = \mu + \tau$ neutrino flavors, the linear distribution functions will be described by the following equations:

$$f(\vec{x}, \vec{p}, t) = \begin{pmatrix} N_{ee} - \Delta(\vec{x}, \vec{p}, t) & \epsilon(\vec{x}, \vec{p}, t) \\ \epsilon^*(\vec{x}, \vec{p}, t) & N_{xx} + \Delta(\vec{x}, \vec{p}, t) \end{pmatrix} \quad (\text{Eq. 2.5.5})$$

$$\bar{f}(\vec{x}, \vec{p}, t) = \begin{pmatrix} \bar{N}_{ee} - \bar{\Delta}(\vec{x}, \vec{p}, t) & \bar{\epsilon}(\vec{x}, \vec{p}, t) \\ \bar{\epsilon}^*(\vec{x}, \vec{p}, t) & \bar{N}_{xx} + \bar{\Delta}(\vec{x}, \vec{p}, t) \end{pmatrix} \quad (\text{Eq. 2.5.6})$$

where $|\epsilon(\vec{x}, \vec{p}, t)| \ll |N_{ee} - N_{xx}|$ and $|\bar{\epsilon}(\vec{x}, \vec{p}, t)| \ll |\bar{N}_{ee} - \bar{N}_{xx}|$.

The behavior of the non-diagonal components $\epsilon(\vec{x}, \vec{p}, t)$ and $\bar{\epsilon}(\vec{x}, \vec{p}, t)$ can be studied by expanding the neutrino transport equation (Eq. 2.5.2) in series of $\epsilon(\vec{x}, \vec{p}, t)$ and $\bar{\epsilon}(\vec{x}, \vec{p}, t)$ and considering only the linear terms. In this linearization, the interest is the dispersion relation between the unstable frequency modes ω and the wave numbers \vec{k} . Using the following ansatz

$$\epsilon(\vec{x}, \vec{p}, t) = Q_{\omega, k} e^{-i(\omega t - \vec{k} \cdot \vec{x})} \quad (\text{Eq. 2.5.7})$$

$$\bar{\epsilon}(\vec{x}, \vec{p}, t) = \bar{Q}_{\omega, k} e^{-i(\omega t - \vec{k} \cdot \vec{x})}, \quad (\text{Eq. 2.5.8})$$

the unstable modes can be identified by the presence of an imaginary component in frequencies and wave numbers that makes the non-diagonal component of the neutrino distribution function grow exponentially in time. When frequency modes ω and the wave numbers \vec{k} have imaginary oscillation modes the system exhibits flavor instabilities [8, 113, 61].

It is important to mention that the neutrino system can have time and spatial flavor instabilities. When ω has a non-zero imaginary component, the system exhibits time instability. The spatial instability occurs when \vec{k} has a non-zero imaginary part. The fast flavor instability regime is characterized by a linear trend between the imaginary modes and $\mu = \sqrt{2}G_F(n_\nu + n_{\bar{\nu}})$:

$$\text{Im}(\omega) \propto \mu \quad (\text{Eq. 2.5.9})$$

$$\text{Im}(\vec{k}) \propto \mu. \quad (\text{Eq. 2.5.10})$$

Slow oscillation modes scale with $\sqrt{\omega_v \mu}$, where ω_v is the vacuum oscillation frequency.

In a flavor instability, the off-diagonal components of the density matrix rapidly reach the order of magnitude of the diagonal terms. At this point, it is expected that the exponential behavior to stop. This will be the end of the linear regime of the neutrino transport equation, and the neutrinos' behavior can no longer be explained via the linearized transport equation.

Although the existence of a flavor instability is a promising condition for flavor transformation to occur, it is possible that the instability does not result in significant flavor change. It is not

generally possible to know the final abundance of each neutrino flavor through a linear stability analysis, as the final flavor amount will be determined by the non-linear regime [55, 8]. For this reason, it is necessary to execute computer simulations to approximate the neutrino flavor evolution in the non-linear regime. In Section 4, I will present a particle-in-cell implementation of the quantum neutrino transport that will be used to simulate the flavor evolution of a dense neutrino gas.

The necessary and sufficient condition for the occurrence of fast neutrino flavor instability is a crossing in the angular distribution of neutrinos and antineutrinos [114, 58]. That is, at least one direction \hat{p} , in which the angular distribution of the flavor α , defined as

$$G^\alpha(\vec{x}, \hat{p}, t) = \sqrt{2}G_F \int \frac{d^3p'}{2\pi^2} [f_{\alpha\alpha}(\vec{x}, p'\hat{p}, t) - \bar{f}_{\alpha\alpha}(\vec{x}, p'\hat{p}, t)], \quad (\text{Eq. 2.5.11})$$

is zero [115].

Chapter 3

Non-linear dynamics and chaos

In this chapter, I will define several important concepts in the field of non-linear dynamics. They will be useful to analyze the chaotic behavior of the neutrino flavor evolution in the neutron star merger simulation in Chapter 5. I will start defining a dynamical system in Section 3.1. The importance of non-linearity and its counterpart, linearity will be covered in Section 3.2. In Section 3.3 I will formally define chaos and the sensitive dependence on initial conditions as keys to identifying chaos. In order to exemplify chaos, I will study the logistic map in Section 3.4. Finally, in Section 3.5, I will summarize an outstanding analysis of chaos in the two-beam neutrino model by Hansen and Hannestad in reference [80].

The main structure and fundamental framework of this chapter were built on the following readings: Nonlinear dynamics and chaos: With applications to physics, biology, chemistry, and engineering by S. Strogatz [116]; Chaos in dynamical systems by E. Ott [117]; Chaotic Dynamics: An Introduction by G. Baker [118]; Chaos and nonlinear dynamics: an introduction for scientists and engineers by R. Hilborn [119]; Classical Mechanics by J. Taylor [120]; Lecture notes: Applied Nonlinear Dynamics by A. Schaum [121] and Notes of Nonlinear Dynamics by A. Colombo [122].

3.1 Dynamics

The study of dynamical systems formally started in the 1600s with the advent of Newton's mechanics. Since then, the use of differential equations has been widely applied to model the time evolution of phenomena not only in classical mechanics but also in biology, chemistry, electric devices, economy, quantum mechanics and others. Mathematically, a dynamical system is a deterministic prescription for evolving the state of a system forward in time. Time could be either a continuous or a discrete variable. A dynamical system that is fully characterized by N variables

$$x_1, x_2, \dots, x_N \tag{Eq. 3.1.1}$$

can be modeled as a system of N first-order, autonomous, ordinary differential equations as follows [117]

$$\begin{aligned} \frac{dx_1}{dt} &= F_1(x_1, x_2, \dots, x_N) \\ \frac{dx_2}{dt} &= F_2(x_1, x_2, \dots, x_N) \\ &\cdot \\ &\cdot \\ &\cdot \\ \frac{dx_N}{dt} &= F_N(x_1, x_2, \dots, x_N). \end{aligned} \tag{Eq. 3.1.2}$$

This system can be written in vector form as

$$\frac{d\mathbf{x}}{dt} = \mathbf{F}(x_1, x_2, \dots, x_N), \quad (\text{Eq. 3.1.3})$$

where \mathbf{x} is the vector state of the dynamical system

$$\mathbf{x} = \begin{pmatrix} x_1 \\ x_2 \\ \cdot \\ \cdot \\ x_N \end{pmatrix}. \quad (\text{Eq. 3.1.4})$$

The state space of a dynamical system represents the set of all possible states. The number of variables needed to characterize the state of the system defines its dimension. The trajectory of the dynamical system is the path the states take through state space as time evolves

$$(x_1(t), x_2(t), \dots, x_N(t)). \quad (\text{Eq. 3.1.5})$$

Theoretically, it is possible to compute the future behavior of a dynamical system given a set of initial conditions $\mathbf{x}(t_0)$. However, as I will explain in Sections 3.3 and 3.4, in practice our ability to predict the behavior of certain kinds of dynamical systems called chaotic could be limited even though the full mathematical description is known.

3.2 Linear and non-linear dynamical systems

Dynamical systems can be classified as linear or non-linear in dependence on the mathematical set of equations that define them.

Linear dynamical systems are characterized by a set of equation that evolves linearly on the dependent variables

$$(x_1, x_2, \dots, x_N) \quad (\text{Eq. 3.2.1})$$

and their derivatives

$$\begin{aligned} &\frac{d}{dt}(x_1, x_2, \dots, x_N) \\ &\frac{d^2}{dt^2}(x_1, x_2, \dots, x_N) \\ &\cdot \\ &\cdot \\ &\cdot \end{aligned} \quad (\text{Eq. 3.2.2})$$

In general, linear dynamical systems have the following structure:

$$\begin{aligned} \frac{dx_1}{dt} &= a_{11}x_1 + a_{12}x_2 + \dots + a_{1N}x_N + b_1 \\ \frac{dx_2}{dt} &= a_{21}x_1 + a_{22}x_2 + \dots + a_{2N}x_N + b_2 \\ &\cdot \\ &\cdot \\ &\cdot \\ \frac{dx_N}{dt} &= a_{N1}x_1 + a_{N2}x_2 + \dots + a_{NN}x_N + b_N, \end{aligned} \quad (\text{Eq. 3.2.3})$$

where the coefficients a_{ij} and b_i can depend on time. In the vector formulation (Eq. 3.1.3), linear systems take the following form:

$$\frac{d}{dt}\mathbf{x}(t) = \mathbf{a}\mathbf{x}(t) + \mathbf{b}, \quad (\text{Eq. 3.2.4})$$

where \mathbf{a} is the matrix of the coefficient a_{ij} and \mathbf{b} is the vector of the coefficients b_i .

Linear systems have played a crucial role in physics. Sometimes they provide good approximations of non-linear systems that can not be solved analytically. The simple harmonic oscillator

$$\ddot{x} = -\omega^2 x \quad (\text{Eq. 3.2.5})$$

and the driven harmonic oscillator

$$\ddot{x} + \omega^2 x = F(t), \quad (\text{Eq. 3.2.6})$$

that in the form of the Eq. 3.2.3 is

$$\dot{x}_1 = x_2 \quad (\text{Eq. 3.2.7})$$

$$\dot{x}_2 = x_3 \quad (\text{Eq. 3.2.8})$$

$$\dot{x}_3 = -\omega^2 x_1 + F(t) \quad (\text{Eq. 3.2.9})$$

are examples of linear systems.

An important property of linear systems is that a small change in the initial conditions leads only to a small and constant change in the solution at all times [123]. Another characteristic is that a linear combination of a linear-independent solution will also be a solution. This property is called the superposition principle and is an important property of the wave functions (linear superposition of the eigenfunction) in quantum mechanics. The superposition principle implies that a linear set of differential equations can be broken down into parts and solved independently to finally recombine the partial solution to get the complete solution. This is the basic principle behind the Laplace transforms, superposition arguments and Fourier analysis methods to solve linear differential equations [116].

On the other hand, non-linear dynamical systems involve non-linear terms of the dependent variables and their derivatives in the functions $F_i(x_1, x_2, \dots, x_N)$ in equation 3.1.2. This implies terms of the form $x_1 x_2$, $\sin x_1$, $x_N \dot{x}_2$, $x_1^{-4} \ln x_2$ and others. An example of a non-linear dynamical system is the two-body gravitational motion

$$m\ddot{\mathbf{r}} = -\frac{GmM}{r^2}\hat{\mathbf{r}}. \quad (\text{Eq. 3.2.10})$$

and the simple pendulum

$$\ddot{\theta} = -\frac{g}{L} \sin \theta. \quad (\text{Eq. 3.2.11})$$

Unlike linear systems, non-linear systems do not have methodical solutions and almost all of them are impossible to solve analytically. Nonlinearity is a prerequisite for the appearance of chaos (Section 3.4). However, not all non-linear dynamical systems are chaotic. In a non-linear first-order autonomous ordinary differential equation (Eq. 3.1.2) another requirement for the existence of chaos is a state space with a dimension greater than three [117]. The superposition principle does not hold in a non-linear system. In general, any linear combination of solutions will not be a solution.

3.3 Chaos

One of the first studies of chaotic dynamics was done by Poincare on the three-body celestial problem [124]. Poincare, rather than focusing on individual orbits tried to characterize the effect

of a set of initial conditions on the final state of the systems. In spite of Poincare's work, however, the possibility of chaos in real physical systems was not widely appreciated until relatively recently. There were several reasons for this, including the mathematical difficulty of the papers for workers in other fields and the fact that the proved theorems were not enough to convince researchers that this behavior would be critical in their systems. The situation changed drastically with the use of numerical techniques to solve dynamical systems on digital computers [117].

The discovery by Lorenz in 1963 [125] of an atmospheric convection model that exhibits irregular and unpredictable behavior opened the door to the study of so-called chaotic systems. Chaotic systems are non-linear dynamical systems with erratic and irregular complex behavior whose principal characteristic is that, although these systems are essentially deterministic in the sense that the precise knowledge of the initial conditions at one time allows us to predict the future behavior, a very small variation of these initial conditions (like the measurement uncertainty) leads to completely different results. Unlike non-chaotic systems in which the approximate present determines the future approximately, in chaotic systems, the approximate present leads to a completely different future. [118, 120, 116, 126, 119].

Since the Lorenz findings, many dynamical systems have been found to exhibit chaos. It was surprising how chaos and complexity can arise from simple dynamic systems like the logistic equation [127], a driven damped pendulum [128] or a double pendulum [129]. It has been found that chaos, rather than being an isolated behavior of a specific dynamical system, is a universal property of the complexity in all of them [119].

There are several ways to test if a dynamical system exhibits chaos or not; one of the most commonly used is the Lyapunov exponent. The Lyapunov exponent measures the sensitive dependence on the initial condition. Suppose a dynamical system with the initial condition $\mathbf{x}_{t=t_0}$. Consider a nearby point $\mathbf{x}_{t=t_0} + \delta_{t=t_0}$ where $|\delta_{t=t_0}|$ is extremely small. If δ_t satisfies

$$|\delta_t| \approx |\delta_{t=t_0}| e^{\lambda t}, \quad (\text{Eq. 3.3.1})$$

λ is a Lyapunov exponent of the dynamical system. The Lyapunov exponents can have positive, negative or zero values. A dynamical system is chaotic if the Lyapunov exponent is found to be positive

$$\lambda_{\text{chaos}} > 0. \quad (\text{Eq. 3.3.2})$$

It is important to note that only an approximate exponential trend is expected. Different regions in the state space can have proper local behavior, such as an erratic oscillatory motion, which can impact the local tendency of $|\delta_t|$. However, in a chaotic system, the average behavior and main tendency of $|\delta_t|$ will be exponential.

At a certain value of $|\delta_t|$, it is expected that the exponential trend will stop. Many dynamical systems are bounded. That means their variables can only take values in a certain domain. It is not expected that the difference between two wave functions of the same quantum system with different initial conditions will be greater than one because both wave functions are normalized to one.

In a n -dimensional system, there will be n different Lyapunov exponents. A useful way to think about the set of Lyapunov exponents is as a sphere of small perturbed initial conditions with the center at a given point $\mathbf{x}_{t=t_0}$. As time evolves, the sphere of the perturbed initial condition will change shape, becoming an ellipsoid. Each dimension of the sphere will stretch and contract at a different rate according to its Lyapunov exponent,

$$|\delta_t^k| \approx |\delta_{t=t_0}^k| e^{\lambda_k t}, \quad (\text{Eq. 3.3.3})$$

where $k = 1, 2, \dots, n$ represent the direction of each dimension of the dynamical system. δ_t^k are usually called Lyapunov vectors of the Lyapunov exponent λ_k . If the perturbation evolves for a long time, the greater Lyapunov exponent will dominate the shape of the sphere. When referring to the Lyapunov exponent, it is common to consider the largest of them.

The Lyapunov exponent also depends on the trajectory in the state space the solution takes. For this reason, it is recommended to take the average Lyapunov exponent at different points of the trajectory to get a value that more accurately represents the long-term evolution of the system [118, 119].

In the next Section, I will exemplify chaos using the dynamical system in the logistic equation, an extremely simple but chaotic system that is usually used to describe the evolution in time of the population of some species.

3.4 The logistic equation

Dynamical systems can be continuous or discrete in time. Previous examples of differential equations are continuous in time (Eq. 3.1.2). Dynamical system in which time is a discrete variable are called iterated maps. Iterated maps are used to describe events that occur once over a period of time. For example, the total amount of rain in winter or the number of bear births after the mating season. In these systems, it is not of interest how much rain or how many bear births occurred in a single day or in a single hour, but the total amount over a period of time is of big interest. Iterated maps are also useful in computer simulation, even time-continuous dynamical systems need to be discretized in steps to be simulated.

The logistic equation is an iterated map used to describe the population of a species in an environment with limited resources

$$n_{i+1} = rn_i \left(1 - \frac{n_i}{N}\right). \quad (\text{Eq. 3.4.1})$$

In the logistic equation r is the growth rate parameter. In a species in which every old member died after a season, leaving two new hatchlings alive, the growth rate parameter r will have a value of two. The term $(1 - n_i/N)$ is the mortality factor. N is the maximum or carrying capacity of the model when overcrowding or starvation becomes important.

When n_i is small compared to N the logistic equation can be approximately described by the following equation:

$$n_{i+1} \approx rn_i, \quad (\text{Eq. 3.4.2})$$

this is a fast exponential growth of the population, which implies the environment has enough resources for all the population. However, when n_i becomes comparable to N , the environment resources will be limited and the mortality factor will become important, limiting the growth of the population.

When n_i equals N , the resources of the environment will not be sufficient to satisfy the needs of the species, and in the next iteration, the population will be zero, implying extinction.

Although the logistic equation appears to be a very simple mathematical model of the population of a species, for a certain set of parameters, it shows a huge dynamical complexity [130].

To study the logistic equation's solutions, it is convenient to do the following change of variable

$$x_i = \frac{n_i}{N}. \quad (\text{Eq. 3.4.3})$$

With this change, x_i can only take values between zero and one. $x_i = 1$ will represent the maximum capacity of the model and $x_i = 0$ the extinction of the species. Now, the logistic equation takes the form

$$x_{i+1} = rx_i(1 - x_i), \quad (\text{Eq. 3.4.4})$$

where $0 \leq r \leq 4$ to satisfy $0 \leq x_i \leq 1$.

In the upper panel of Figure 3.1 I plot the logistic equation for $r = 0.75$ in a wide range of initial conditions x_0 . Independent of the initial conditions, as time evolves, the species becomes

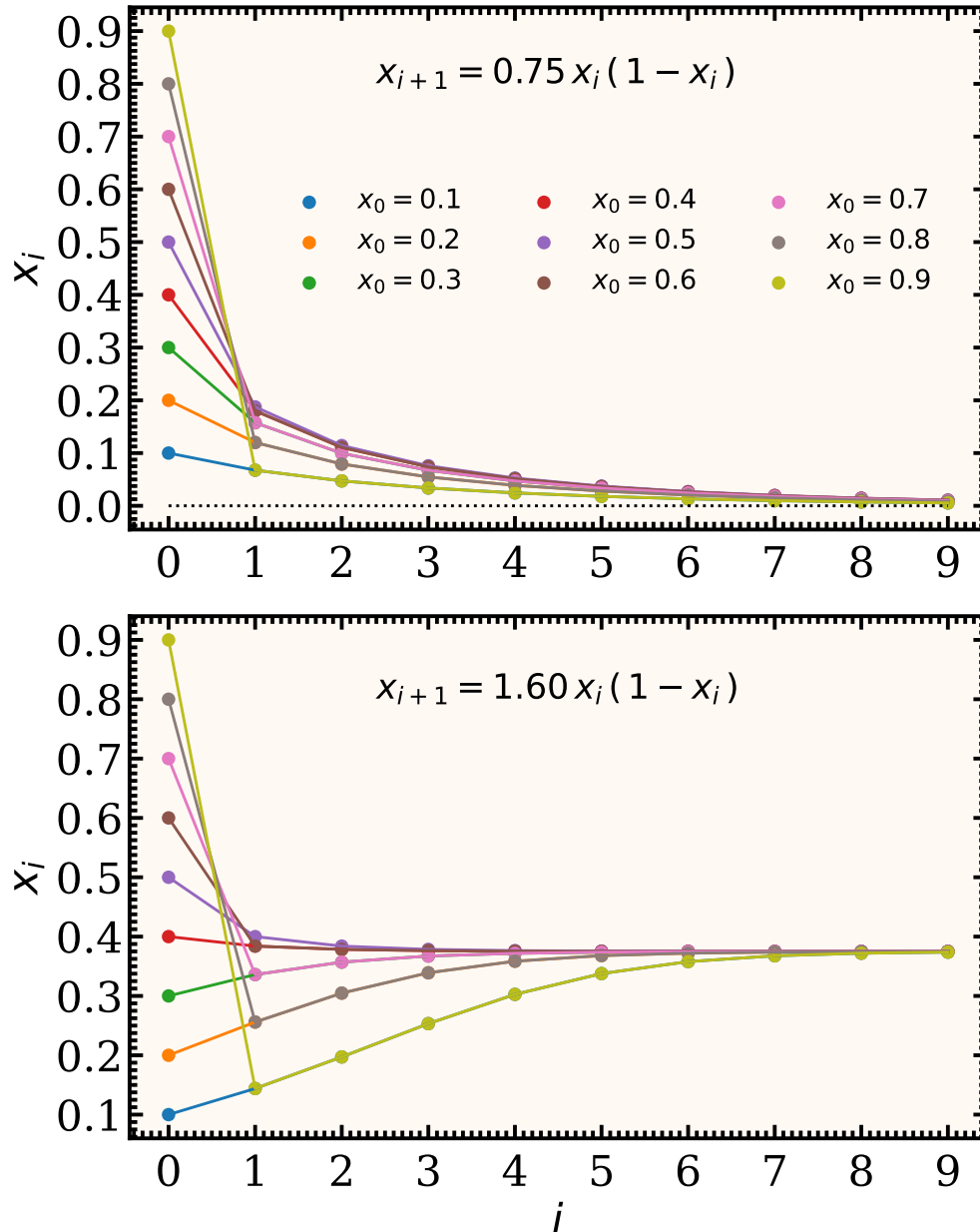


Figure 3.1: First nine iterations of the logistic equation with a growth parameter r of 0.75 (upper panel) and 1.60 (lower panel). Different initial conditions x_0 that spanned the range between 0.1 and 0.9 are shown. In the upper panel, the logistic equation has a stable equilibrium point at $x_i = 0$. Independent of the initial population, the species goes extinct. The same trend occurs for $0 \leq r < 1$. In the lower panel, the solutions do not follow $x_i = 0$ as it is now an unstable equilibrium point. $x_i = 0.37$ is the new stable equilibrium point. Independent of the initial population, the logistic equation follows the stable equilibrium point as an asymptotic value. This is the main tendency for $1 \leq r < 3$. In this range, the stable equilibrium point takes the value of $x_i = (r - 1)/r$. For $r \geq 3$, all the equilibrium points became unstable.

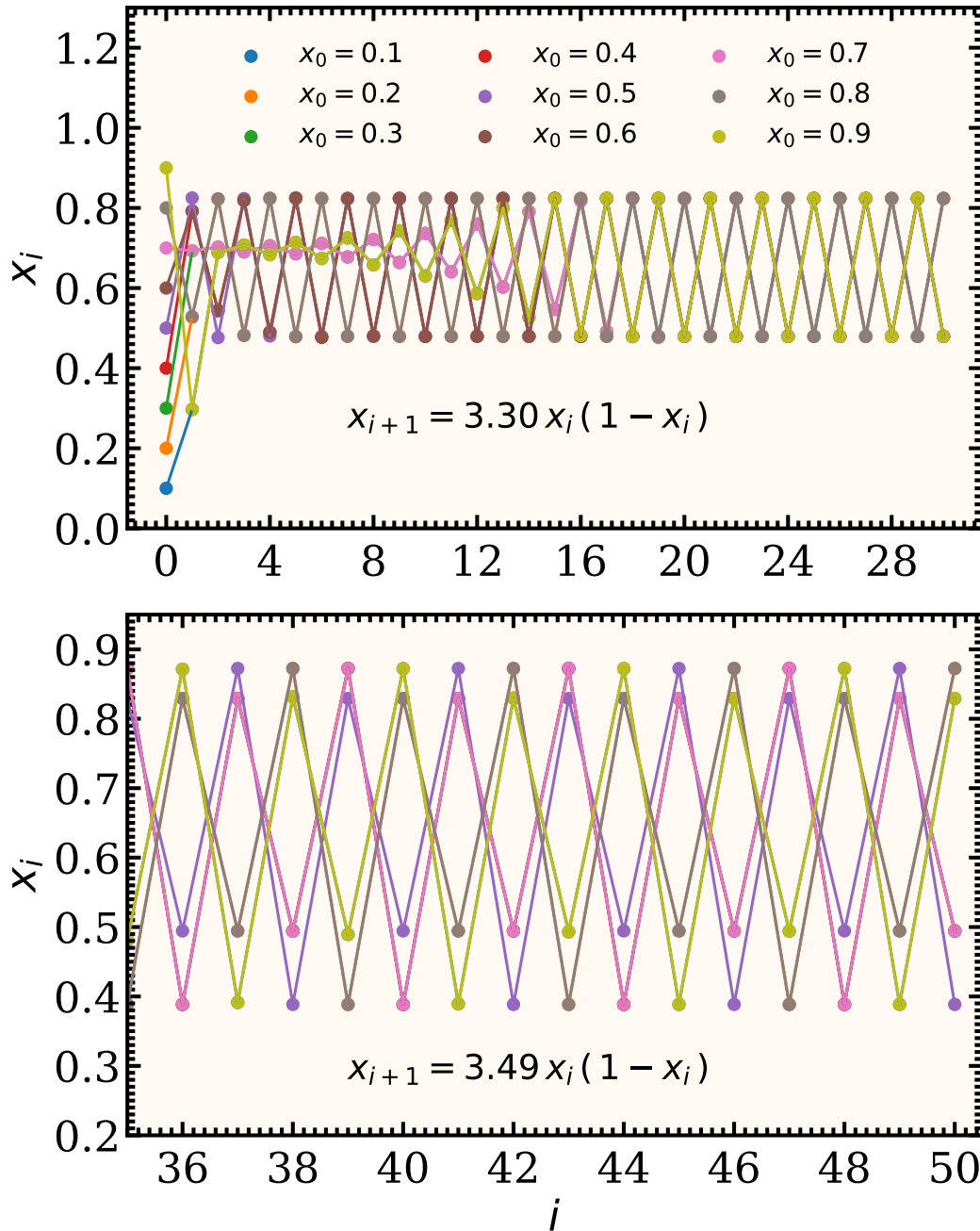


Figure 3.2: Doubling period tendency of the logistic equation as the growth rate parameter r increases. In the top panel are shown the iterations of the logistic equation with $r = 3.30$. At iteration 16 the solution starts a periodic behavior every two iterations (two-cycles). This periodic behavior starts abruptly at $r = 3$. When r increases to approximately 3.45 the logistic equation changes abruptly from a two-cycle to a four-cycle behavior. In the lower panel, the four-cycle behavior of the logistic equation with $r = 3.49$ is plotted. This double period trend continues as r increases.

extinct. This behavior is repeated for growth rate values between zero and one ($0 \leq r \leq 1$), which means that the reproduction rate is not enough to maintain the specie.

In the lower panel of Figure 3.1 I show the first nine iterations of the logistic map for $r = 1.60$. The initial conditions x_0 in this panel expand from 0.1 to 0.9. Independent of the initial conditions of the specie, after nine iterations, the population converges to approximately 0.37 and stays there in all the following iterations. This behavior is repeated for $1 < r < 3$.

The two versions of the logistic equation ($r = 0.75$ and 1.60) in Figure 3.1 have equilibrium points at different values of x_i . An equilibrium point is characterized by fulfilling the following relationship:

$$x_{i+1} = x_i. \quad (\text{Eq. 3.4.5})$$

For the logistic equation, the equilibrium points satisfy

$$x_i = rx_i(1 - x_i) \quad (\text{Eq. 3.4.6})$$

whose solutions are

$$x_i = 0 \quad (\text{Eq. 3.4.7})$$

$$x_i = \frac{r-1}{r}. \quad (\text{Eq. 3.4.8})$$

For $0 \leq r < 1$, the equilibrium point in the equation 3.4.8 is negative and only $x_i = 0$ is a valid equilibrium point. For $1 < r < 3$, both equilibrium points are valid.

A stability test [116] of the equilibrium point in equations 3.4.7 and 3.4.8 shows that $x_i = 0$ is a stable point for $0 \leq r \leq 1$ and becomes unstable for $r > 1$. The equilibrium point $x_i = (r-1)/r$ is stable for $1 < r < 3$ and unstable for $r \geq 3$.

For $r \geq 3$ the solution of the logistic equation increases its complexity. In the upper panel of Figure 3.2 I plot the logistic equation for 30 iterations for $r = 3.30$. This panel shows a variety of initial conditions x_0 between 0.1 and 0.9. The solution no longer follows a single asymptotic value. Actually, it oscillates between two different values 0.48 and 0.82 (two-cycle behavior). This behavior starts abruptly at $r = 3$.

At approximately $r = 3.45$, the logistic equation abruptly changes its behavior again doubling the two-cycle behavior to a four-cycle behavior. In the lower panel of Figure 3.2 I plot some late iterations of the logistic equation (from the 35th to the 50th iterations) with a growth rate parameter of 3.49. Independent of the initial conditions x_0 , the logistic equation shows a pattern that is repeated after four iterations.

The doubling period behavior of the logistic equation continues as r increases. At approximately $r = 3.53$, the behavior abruptly changes to an eight-cycle. At $r = 3.564$ a 16-cycle behavior starts and at $r = 3.568$ a 32-cycle behavior follows the tendency. Eventually, at approximately $r = 3.569$, the logistic equation reaches an infinity-cycle behavior. At this point the past behavior of the logistic equation is never repeated. This is chaos.

In the top panel of Figure 3.3 I plot the iterations of the logistic equation in the chaotic regime ($r = 3.57$). The behavior there is highly stochastic.

Surprisingly, as r increases, the logistic equation recovers the periodicity. For $3.828 \leq r \leq 3.841$ the logistic equation exhibits a three-cycle behavior. This can be observed in the lower panel of Figure 3.3 for $r = 3.84$. As r increases, it continues doubling the period to a six-cycle, 12-cycle, until it reaches the infinite-cycle behavior in a chaotic regime again.

So far, there is no clear connection between the behavior of the logistic equation and the growth rate parameter r . As I exposed previously, the logistic equation constantly has transitions in its behavior. A useful tool for understanding these abrupt changes is the bifurcation diagram. A bifurcation diagram shows the asymptotic values of the logistic equation in dependence on the growth rate parameter r .

The logistic equation for $0 \leq r < 1$ has a unique possible asymptotic value $x_{i \rightarrow \infty} = 0$. For $1 \leq r < 3$, the solution takes a single asymptotic value that depends on the growth rate parameter $x_{i \rightarrow \infty} = (r - 1)/r$. This behavior can be observed for $r < 3$ in the bifurcation diagram of the logistic equation in the top panel of Figure 3.4.

For $r > 3$, the logistic equation starts the doubling period behavior that ends in an infinite cycle at approximately $r = 3.569$. The bifurcation diagram of the logistic equation clearly shows the high complexity of their solution for $3 \leq r \leq 4$. In a chaotic regime, the asymptotic values ($x_{i \rightarrow \infty}$) are a continuous domain that reaches its maximum range between zero and one at $r = 4$.

It is important to note that the doubling period behavior is not an individual property of the logistic equation. Other chaotic systems in classical mechanics, circuits and fluid dynamics show the same behavior. The periodic windows and the size of the interval between the abrupt doubling of the period in all of them follow approximately the same geometric acceleration, even when they are completely different dynamical systems. This led researchers to think that, rather than being an isolated behavior, chaos is a universal property of dynamic systems.

The universality of chaotic systems has been quantified using the parameter values for which the systems double the period in the bifurcation diagram. In the logistic map, they are

$$r = 3, 3.449, 3.54409, 3.5644, 3.568759, \dots \quad (\text{Eq. 3.4.9})$$

Feigenbaum found that the limit when time goes to infinity of division between the distance of two successive bifurcation points is a fundamental constant (other than π and e)

$$\delta = \lim_{i \rightarrow +\infty} \frac{r_i + r_{i+1}}{r_{i-1} + r_i} \approx 4.669201609 \dots \quad (\text{Eq. 3.4.10})$$

The Feigenbaum constant has been determined in several experiments in hydrodynamics [131, 132] and electric circuits [133, 134, 135, 136].

It is important to emphasize that the period doubling behavior is one of the many possible routes a dynamical system can take towards chaos. Other chaotic systems, like the Lorentz equation, the double pendulum and the three-body gravitation system, do not show the double route to chaos and are intrinsically chaotic.

Chaotic systems are characterized by exhibiting complicated non-periodic behavior. However, this is not the main factor in determining whether the system exhibits chaos. The most important property of chaotic systems is their sensitive dependence on the initial condition.

The sensitive dependence on initial conditions can be quantified by computing the difference between trajectories with close initial conditions. In the one dimensional map of the logistic equation, for an arbitrary initial condition x_0 , consider a nearby trajectory to the solution to the logistic equation with initial condition $x_0 + \delta_0$, where δ_0 is a small perturbation. After i iterations, the initial perturbation δ_0 becomes δ_i . If the trend of δ_i satisfies

$$|\delta_i| = |\delta_0| e^{\lambda i} \quad (\text{Eq. 3.4.11})$$

λ is the Lyapunov exponent. A positive Lyapunov exponent means the system is highly sensitive to initial conditions and chaotic.

Based on the definition in equation 3.4.11 it can be demonstrated that the value of the Lyapunov exponent for a one dimensional map will be given by

$$\lambda = \lim_{i \rightarrow +\infty} \frac{1}{i} \sum_{n=0}^{i-1} \ln |f'(x_n)|, \quad (\text{Eq. 3.4.12})$$

where f_{x_i} is defined as

$$x_{i+1} = f(x_i), \quad (\text{Eq. 3.4.13})$$

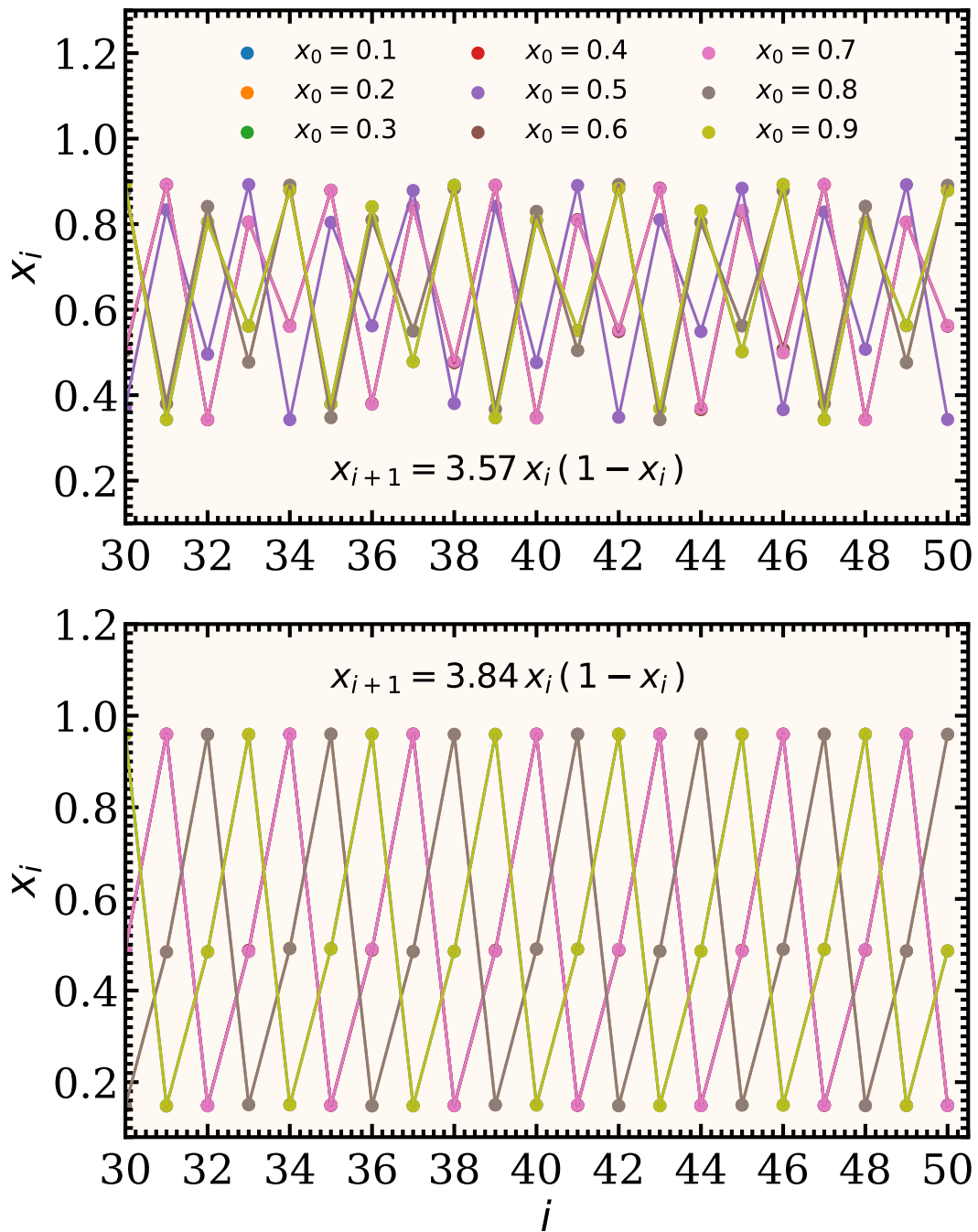


Figure 3.3: Iterations of the logistic equation for two different growth rates r and initial conditions between 0.1 and 0.9. The upper panel shows the logistic equation for $r = 3.57$. This corresponds to the chaotic regime of the logistic equation. The solution will never repeat its past behavior. The lower panel shows the logistic equation for 3.84. At this point, the logistic equation recovers a three-cycle periodicity. However, as we increase r the period doubling behavior starts until it reaches the chaotic regime again.

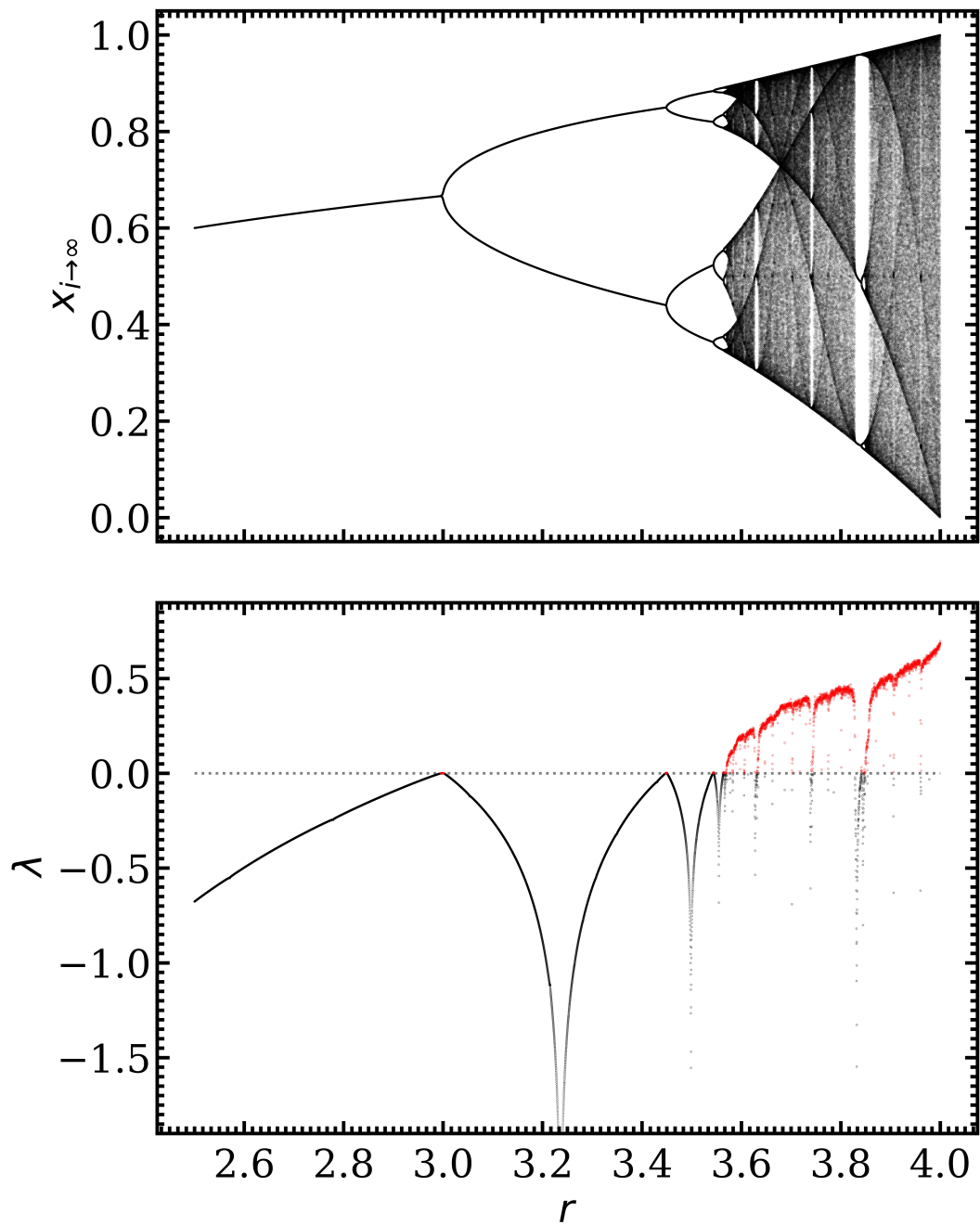


Figure 3.4: Final set of asymptotic values (bifurcation diagram) (top panel) and Lyapunov exponents (Eq. 3.4.12) (bottom panel) in dependence of the growth rate parameter r for the logistic equation. In the non-chaotic regime (negative Lyapunov exponents), the logistic equation exhibits periodic behavior. This is represented by a finite set of final asymptotic values in the bifurcation diagram. In the chaotic regime (positive Lyapunov exponents), the solution never repeats its past behavior. This corresponds to an infinite set of asymptotic values in the bifurcation diagram. Images generated and distributed under the CC-BY-NC-ND license [2].

and

$$f'(x_i) = \left. \frac{df(x)}{dx} \right|_{x=x_i}. \quad (\text{Eq. 3.4.14})$$

For the logistic equation $f(x) = rx(1-x)$.

In the lower panel of Figure 3.4 are plotted the Lyapunov exponents computed with Equation 3.4.12 versus the value of the growth rate parameter r . The appearance of a positive Lyapunov exponent (red dots) indicates chaos. The chaotic behavior of the solution of the logistic equation emerges for $r > 3.569$. However, even within this interval, there are zones with a negative Lyapunov exponent (black dots).

The zones with negative Lyapunov exponents coincide with the values of r for which the logistic equation has a finite set of asymptotic values, these are the periodic n -cycle solutions. The positive Lyapunov exponents are related to the value of r with a continuous set of final asymptotic values. For these intervals of r the solutions do not repeat their past behavior.

The sensitive dependence on the initial condition of the chaotic and periodic solutions to the logistic equation is also described in Figure 3.5. There, I simulated the behavior of the logistic equation for a growth rate parameter of $r = 3.49$ and 4.00 . This corresponds to the four-cycle and infinity-cycle (chaotic) solutions.

In panel (a) of Figure 3.5 are shown two simulations of the four-cycle solution with close initial conditions x_0 of 0.01 and $0.01 + 10^{-10}$. As can be observed in panel (b) of Figure 3.5, both simulations converge. After 60 iterations, the initial difference between the two simulations decreased from 10^{-10} to 10^{-16} .

In panel (c) of Figure 3.5 the chaotic behavior of the logistic equation is plotted for two nearby initial conditions x_0 of 0.01 and $0.01 + 10^{-10}$. Contrary to the four-cycle solution, after 25 iteration, the two chaotic simulations start to behave in a different trend. The panel (d) of Figure 3.5 clarifies that the small initial difference between the two solutions grows exponentially (a line in the logarithmic plot) until it reaches the same magnitude as the solution x_i . At this point, the small difference between the two initial conditions 10^{-10} has become important, making the two solutions evolve in different ways.

The sensitive dependence on the initial condition of a chaotic system has a huge implication for our capacity to predict the future behavior of a chaotic dynamical system. If the initial difference between the initial condition (10^{-10}) in the logistic map is considered an uncertainty in our knowledge of the initial condition (remember, it is impossible to do an exact measurement). After 30 iterations, the propagation of uncertainty will grow from 10^{-10} to 1. As the possible values of x_i are between zero and 1, the final uncertainty in our prediction will be of 100%. This is why chaotic systems are highly unpredictable.

3.5 Chaos in the two beam neutrino model

Chaos in neutrino flavor evolution in dense environments has been studied by Hansen and Hannestad [80]. They numerically studied the two-beam neutrino model, in which neutrinos are traveling in two momentum states in opposite directions ($\vec{p}_1 = -\vec{p}_2$). This model is well known to exhibit flavor instabilities.

Hansen and Hannestad used the polarization vector parameterization of the density matrices for two flavors

$$\mathbf{P}_i = \text{Tr}(\rho\sigma_i) \quad (\text{Eq. 3.5.1})$$

$$\bar{\mathbf{P}}_i = \text{Tr}(\bar{\rho}\sigma_i), \quad (\text{Eq. 3.5.2})$$

where σ_i represents the Pauli matrices, and \mathbf{P} holds for neutrinos and $\bar{\mathbf{P}}$ for antineutrinos. It is evident that the flavor polarization vector is a three-dimensional vector, as there are only three

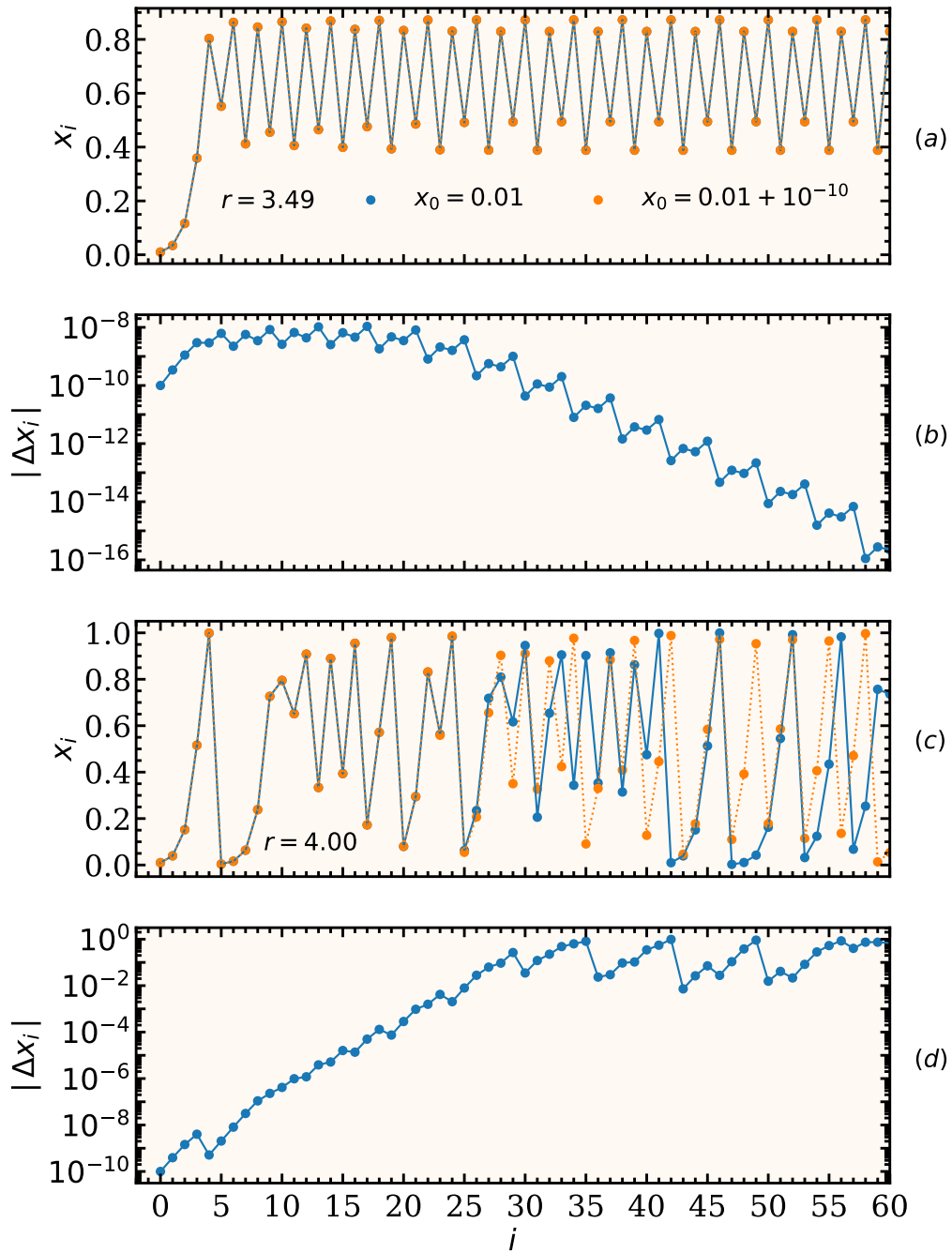


Figure 3.5: Sensitive to the initial condition in stable and chaotic systems. The panel (a) shows two four-cycle solutions of the logistic equation that are iterated starting with a close initial condition of $x_0 = 0.01$ and $0.01 + 10^{-10}$. The panel (b) shows the difference between the two solutions in the panel (a). Both simulations converge. On the contrary, in panel (c) are plotted two chaotic solutions to the logistic equations with nearby initial conditions $x_0 = 0.01$ and $0.01 + 10^{-10}$. As panel (d) shows, the difference between the two solutions grows exponentially over time but stops after approximately 25 iterations.

Pauli matrices. The density matrix in terms of the flavor polarization vector will be given by

$$\rho = \frac{1}{2} (\mathbf{I} + \mathbf{P} \cdot \boldsymbol{\sigma}) \quad (\text{Eq. 3.5.3})$$

$$\bar{\rho} = \frac{1}{2} (\mathbf{I} + \bar{\mathbf{P}} \cdot \boldsymbol{\sigma}). \quad (\text{Eq. 3.5.4})$$

where $\boldsymbol{\sigma} = (\sigma_1, \sigma_2, \sigma_3)$. The polarization vector in equations 3.5.1 and 3.5.2, contrary to the isospin convection, in which neutrinos and antineutrinos with similar flavor content are represented with polarization vectors pointing in opposite directions, Hansen and Hannestad decided to point neutrinos and antineutrinos with same flavor content in the same direction. In equations 3.5.1 and 3.5.2 both polarization vectors \mathbf{P} and $\bar{\mathbf{P}}$ are normalized to one.

In the polarization vector formalism and considering the generalization to N momentum states and neglecting matter effects in order to make the analytical treatment of the equations simpler (as was exposed in Section 2.4 matter effects just redefine the mixing angles and can be neglected in analytic calculation), the equation of motion for the i momentum state (Equation (1) in reference [80]) will be given by

$$\dot{\mathbf{P}}_i = \left(\omega_i \mathbf{B} + \frac{\mu}{2} \sum_{j=1}^N (\mathbf{P}_j - \bar{\mathbf{P}}_j) (1 - \vec{v}_j \cdot \vec{v}_i) \right) \times \mathbf{P}_i \quad (\text{Eq. 3.5.5})$$

$$\dot{\bar{\mathbf{P}}}_i = \left(-\omega_i \mathbf{B} + \frac{\mu}{2} \sum_{j=1}^N (\mathbf{P}_j - \bar{\mathbf{P}}_j) (1 - \vec{v}_j \cdot \vec{v}_i) \right) \times \bar{\mathbf{P}}_i \quad (\text{Eq. 3.5.6})$$

where $\mu \sim 2\sqrt{2}G_F n_\nu$; $\omega_i = \Delta m^2/2E_i$; \mathbf{B} is the mass unit vector in flavor space, this vector result from the matrix decomposition of the two flavor vacuum Hamiltonian in terms of the Pauli matrices. $\vec{v}_i = \vec{p}_i/E_i$ is the direction of the momentum. Following Hansen and Hannestad nomenclature, arrows indicate vectors in real space while bold faces refer to vectors in polarization space.

By convention, Hansen and Hannestad take the mass unit vector in flavor space to define the z axis $\mathbf{B} = (\mathbf{0}, \mathbf{0}, -1)$. This choice ensures that $\omega > 0$ corresponds to the normal hierarchy, while $\omega < 0$ corresponds to the inverted hierarchy. This implies that the polarization vector given by equations 3.5.1 and 3.5.2 needs to be rotated. In equations 3.5.1 and 3.5.2, the z component of the polarization vectors represents the electron flavor state. A neutrino and antineutrino in the pure electron state will be given by $\mathbf{P}_i = \bar{\mathbf{P}}_i = (0, 0, 1)$. However, on the new axis configuration a neutrino and antineutrino in the pure electron state will be given by

$$\mathbf{P}_i = \bar{\mathbf{P}}_i = (\sin 2\theta, 0, \cos 2\theta), \quad (\text{Eq. 3.5.7})$$

where the mixing angle is arbitrarily chosen to satisfied $\sin(2\theta) = 0.1$.

In addition, in order to take advantage of the conservative nature of the system, they considered a classical Hamiltonian formulation of equations 3.5.5 and 3.5.6 given by

$$H_{\text{classical}} = \mathbf{B} \cdot \mathbf{M} + \frac{\mu}{4} \sum_{i,j=1}^N (\mathbf{P}_i - \bar{\mathbf{P}}_i) (\mathbf{P}_j - \bar{\mathbf{P}}_j) (1 - \vec{v}_i \cdot \vec{v}_j) \quad (\text{Eq. 3.5.8})$$

where \mathbf{M} , in analogy to the magnetic moment, takes the form $\mathbf{M} = \sum_{i=1}^N \omega_i \mathbf{P}_i + \omega_i \bar{\mathbf{P}}_i$.

With the classical neutrino flavor Hamiltonian in equation 3.5.8, the equation of motion of the polarization vector will be given in terms of the Poisson brackets as

$$\begin{aligned} \dot{P}_i &= \{P_i, H\} \\ \dot{\bar{P}}_i &= \{\bar{P}_i, H\}. \end{aligned} \quad (\text{Eq. 3.5.9})$$

In the particular case of two momentum states in opposite directions ($\vec{p}_1 = -\vec{p}_2$), it is useful to write the sum and the difference of the polarization vector of neutrinos and antineutrinos in the momentum state $i = 1, 2$ as follows:

$$\begin{aligned} \mathbf{S}_i &= \mathbf{P}_i + \bar{\mathbf{P}}_i \\ \mathbf{D}_i &= \mathbf{P}_i - \bar{\mathbf{P}}_i, \end{aligned} \quad (\text{Eq. 3.5.10})$$

in terms of this, the equation of motion for the flavor in the two beam neutrino systems will be given by

$$\begin{aligned}
\dot{\mathbf{S}}_1 &= \omega \mathbf{B} \times \mathbf{D}_1 + \mu \mathbf{D}_2 \times \mathbf{S}_1 \\
\dot{\mathbf{S}}_2 &= \omega \mathbf{B} \times \mathbf{D}_2 + \mu \mathbf{D}_1 \times \mathbf{S}_2 \\
\dot{\mathbf{D}}_1 &= \omega \mathbf{B} \times \mathbf{S}_1 + \mu \mathbf{D}_2 \times \mathbf{D}_1 \\
\dot{\mathbf{D}}_2 &= \omega \mathbf{B} \times \mathbf{S}_2 + \mu \mathbf{D}_1 \times \mathbf{D}_2
\end{aligned}
\tag{Eq. 3.5.11}$$

Hansen and Hannestad solved these equations numerically with $\omega = \pm 1$ for the normal and inverted mass hierarchies and $\mu = 6$ in some arbitrary units. They choose the initial condition to be symmetric in both beams ($S_1 = S_2$ and $D_1 = D_2$), with neutrinos and antineutrinos in the pure electron states

$$\mathbf{S}_1 = 2(\sin 2\theta, 0, \cos 2\theta) \tag{Eq. 3.5.12}$$

$$\mathbf{D}_1 = (0, 0, 0) \tag{Eq. 3.5.13}$$

$$\mathbf{S}_2 = 2(\sin 2\theta, 0, \cos 2\theta) \tag{Eq. 3.5.14}$$

$$\mathbf{D}_2 = (0, 0, 0). \tag{Eq. 3.5.15}$$

Hansen and Hannestad identify two solutions for the two possible values of the mass hierarchy for the regime where $\mu > \omega$. This condition represents a dense neutrino environment in which the neutrino-neutrino interaction dominates the vacuum flavor transformation mechanism.

For the normal hierarchy $\omega > 0$, S_i and D_i slightly oscillate around the z and y axes, respectively. Hansen and Hannestad called it stationary, as it only deviated slightly from the initial condition.

For the inverted hierarchy $\omega < 0$, the solution is a bipolar oscillation. Since the vector \mathbf{D} that describes the separation between the neutrinos and antineutrinos polarization vector grows until it reaches a full inversion of the polarization vector.

Hansen and Hannestad also studied the antisymmetric initial conditions ($\mathbf{S}_{x_1} = -\mathbf{S}_{x_2} > 0$)

$$\mathbf{S}_1 = 2(\sin 2\theta, 0, \cos 2\theta) \tag{Eq. 3.5.16}$$

$$\mathbf{D}_1 = (0, 0, 0) \tag{Eq. 3.5.17}$$

$$\mathbf{S}_2 = 2(-\sin 2\theta, 0, \cos 2\theta) \tag{Eq. 3.5.18}$$

$$\mathbf{D}_2 = (0, 0, 0). \tag{Eq. 3.5.19}$$

Contrary to the symmetric initial condition. For the normal hierarchy, the antisymmetric initial condition describes bipolar oscillations. For the inverted hierarchy, it describes a stationary solution.

Other modifications to the initial condition of the flavor polarization vectors lead to complex nonlinear behavior. These solutions were called non-periodic.

In order to study the complex behavior of the flavor transformation in the two-beam neutrino model, Hansen and Hannestad computed the set of Lyapunov exponents and the covariant Lyapunov vectors for the stationary, bipolar, and non-periodic solutions. The covariant Lyapunov vectors are a generalization of the concept of normal modes for a stationary solution to arbitrary trajectories in the state space. The Lyapunov vectors have the property that when the vector is evolved forward in time it expands at an exponential rate λ and when it is evolved backward in time it contracts at an exponential rate of $-\lambda$.

Because the neutrino system is conservative, Hansen and Hannestad expected a symmetric set of Lyapunov exponents. The two-beam model consists of four polarization vectors, one for neutrinos and one for antineutrinos in both momentum states. This means that the two-flavor,

two-beam neutrino system expands its solution into 12 dimensional state space, as each vector has three components. Due to this, the set of Lyapunov vectors must have the following form:

$$(\lambda_1, \lambda_2, \lambda_3, \lambda_4, \lambda_5, \lambda_6, -\lambda_6, -\lambda_5, -\lambda_4, -\lambda_3, -\lambda_2, -\lambda_1,).$$

For the trajectories under study, Hansen and Hannestad found only four non-vanishing Lyapunov exponents

$$(\lambda_1, \lambda_2, 0, 0, 0, 0, 0, 0, 0, -\lambda_2, -\lambda_1,).$$

The reason for this behavior is that for each conserved quantity, there will be at least one vanishing Lyapunov exponent. As the set of Lyapunov exponents is symmetric, there will be two vanishing Lyapunov exponents for each conserved quantity. The conserved quantities in the two neutrino beam models are the Hamiltonian $H_{\text{classical}}$, $\mathbf{P} \cdot \mathbf{B}$ where $\mathbf{P} = \sum_{i=1}^N \mathbf{P}_i - \bar{\mathbf{P}}_i$, and the magnitude of the polarization vectors. This results in six vanishing Lyapunov exponents.

In Sections 3.5.1, 3.5.2 and 3.5.3, I will expose Hansen and Hannestad's results for the stationary, bipolar and non-periodic solutions, respectively.

3.5.1 Stationary solutions

The stationary solution occurs in the normal hierarchy for the symmetric initial condition ($S_{x_1} = S_{x_2}$) and in the inverse hierarchy for the antisymmetric initial condition ($S_{x_1} = -S_{x_2}$). Although the solution is called stationary, the neutrino flavor evolution is still non-linear. The Lyapunov exponents were found $\lambda_1 \approx \lambda_2 = 3.31$.

As the state space of the two beam neutrino system is 12 dimensional, the covariant Lyapunov vectors will have 12 components, Hansen and Hannestad computed them for each time step of the simulation, however, the visualization of these vectors is complicated. Hansen and Hannestad computed the average in time of each component and compared their values; this can be found in figure 4 in reference [80]. The covariant vectors show that the direction of the stable and unstable directions in the polarization space is in the same; this means that the diverging solution will always dominate in the solutions. The covariant Lyapunov vector due to a zero Lyapunov exponent indicates a marginally stable direction and are related perturbations that respect the symmetry of the system ($S_{x_1} = S_{x_2}$ symmetric and $S_{x_1} = -S_{x_2}$ antisymmetric).

Another important conclusion about the stability of the systems was found by transforming the reference frame again to that in which the z axis represents the pure electron neutrino state. Hansen and Hannestad concluded that in the case of a vanishing mixing angle θ , the stationary solution will be marginally stable towards perturbations in the flavor content (perturbations in the z axis) but unstable towards anything that could shift the phase as perturbations in the x and y axes. In the case of a non-vanishing mixing angle, the inverted hierarchy will be unstable towards flavor perturbations. The normal hierarchy will be unstable towards anti-symmetric perturbations but marginally stable towards symmetric flavor perturbations.

3.5.2 Bipolar solutions

The bipolar oscillation is found for the antisymmetric ($S_{x_1} = -S_{x_2}$) initial condition for the normal hierarchy and the symmetric ($S_{x_1} = S_{x_2}$) initial condition for the inverted hierarchy.

For the normal hierarchy, the Lyapunov exponents $\lambda_1 = 0.997$ and $\lambda_2 = 0.545$ were found. For the inverted hierarchy, the Lyapunov exponents were found $\lambda_1 = 0.545$ and $\lambda_2 = 0.0006 \approx 0$. Compared to the Lyapunov exponents of the stationary case, these are not degenerate and $\lambda_{\text{bipolar}} < \lambda_{\text{stationary}}$ suggest that the stationary solution is more unstable than the bipolar solution.

The covariant Lyapunov vector analysis shows that only the perturbations that break the symmetry grow exponentially. For the normal hierarchy with antisymmetric initial condition ($S_{1x} = -S_{2x}$) is stable towards antisymmetric perturbations but unstable with regard to symmetric perturbations. The inverted hierarchy with symmetric initial conditions is stable with

respect to symmetric perturbations but unstable with respect to antisymmetric perturbations. At the same time, a small symmetric perturbation in the flavor content (z axis) or the x and y axis will not be important in the inverted hierarchy if the initial conditions are approximately symmetrical.

3.5.3 Non-periodic solutions

The non-periodic solutions are generated with the same initial condition as the stationary and bipolar solutions but by adding $\delta = 2 \cdot 10^{-3}$ to one of the directions S_z or S_y . Hansen and Hannestad found that these initial conditions are enough to make the marginally stable directions non-periodic and at the same time they allow the study of the symmetric ($S_{1x} = -S_{2x}$) and antisymmetric ($S_{1x} = S_{2x}$) initial conditions.

Hansen and Hannestad studied two different solutions, modifying S_z , the solution was found to be mildly non-periodic and modifying S_y very chaotic. They found that modifying all the other components gave results similar to mildly non-periodic and chaotic solutions. The covariant Lyapunov vectors were very similar in both solutions.

The Lyapunov exponents for the non-periodic solution range between $0.28 < \lambda_1 < 1.23$ for both hierarchies. The second Lyapunov exponent for the normal hierarchy ranges from 0.52 to 0.79. For the inverse hierarchy the largest λ_2 was found to be 0.082 indicating that there are directions in which the solution is almost stable in the inverted hierarchy.

The first Lyapunov exponent was found to be approximately one third of the stationary case and quite similar to the bipolar case. This means that a certain perturbation would need about three times longer to affect the solution in the non-periodic cases than it would in the stationary cases.

The mildly non-periodic solution has Lyapunov exponents of approximately one for the normal hierarchy. Both covariant Lyapunov vectors associated with these Lyapunov exponents will diverge almost at the same rate. For the inverse hierarchy, $\lambda_2 \approx 0$ and $\lambda_1 \approx 1$. The covariant Lyapunov vector associated with the first Lyapunov vector will diverge faster than the Lyapunov covariant vector associated with the second exponent and will dominate the chaotic dynamics.

Chapter 4

Methodology

4.1 PIC quantum neutrino transport

To simulate the flavor transformations of neutrinos in a dense neutrino environment, I used the open source EMU code¹ [24]. EMU solves the neutrino quantum kinetic equations (Equations 2.3.15, 2.4.20, 2.5.2 and 2.5.3) under the mean-field approximation.

There are different ways to discretize the neutrino quantum kinetic equations in a dense neutrino gas (see for example [10, 68, 137, 138]). The discretization scheme is the way in which the neutrino momentum and/or coordinate spaces are divided to approximate the computation of the derivatives (advection term, momentum exchange, flavor transformation) in the neutrino transport equation 2.5.2. Several authors have performed calculations under restricted symmetries as simplifications, these included homogenous systems, beam models, planar geometry models and line models. Almost all of them are only in the two-flavor transformation scheme [11].

To discretize the neutrino system, Emu implemented the particle-in-cell (PIC) methods used mostly by the plasma physics community. To discretize the neutrino field, EMU uses computational particles that represent a given number of neutrinos N and antineutrinos \bar{N} with two density matrices that represent the neutrinos ρ and antineutrinos $\bar{\rho}$ quantum states.

In EMU, the evolution in time of a computational particle is given by the next set of equations (Equation 4 in reference [24])

$$\begin{aligned}
 \frac{\partial \rho}{\partial t} &= -i [H, \rho] \\
 \frac{\partial \bar{\rho}}{\partial t} &= -i [\bar{H}, \bar{\rho}] \\
 \frac{\partial \mathbf{x}}{\partial t} &= c \hat{\mathbf{p}} \\
 \frac{\partial E}{\partial t} &= 0 \\
 \frac{\partial \hat{\mathbf{p}}}{\partial t} &= 0 \\
 \frac{\partial N}{\partial t} &= \frac{\partial \bar{N}}{\partial t} = 0.
 \end{aligned}
 \tag{Eq. 4.1.1}$$

These imply there is no momentum exchange (incoherent scattering), annihilation, or creation of neutrinos and antineutrinos, neutrino and antineutrino energies are larger than their rest mass, and the flavor transformation is given by the Schrödinger equation 2.3.12. As was exposed in

¹EMU GitHub repository: <https://github.com/AMReX-Astro/Emu>

Chapter 2, the neutrino Hamiltonian is the sum of the vacuum, matter and neutrino-neutrino interaction Hamiltonian in equations 2.3.15, 2.4.20 and 2.5.3, respectively.

According to the EMU discretization of the neutrino system, the vacuum, matter and neutrino-neutrino interaction Hamiltonians are conveniently coded in the following form:

$$H_{ab}^{\text{vacuum}} = U_{ac} \sqrt{p^2 c^2 + m_c^2 c^4} \delta_{cd} U_{db}^\dagger \quad (\text{Eq. 4.1.2})$$

$$H_{ab}^{\text{matter}} = \sqrt{2} G_F (\hbar c)^3 (n_a - \bar{n}_a^*) \delta_{ab} \quad (\text{Eq. 4.1.3})$$

$$H_{ab}^{\text{neutrino}} = \sqrt{2} G_F (\hbar c)^3 [(n_{ab} - \bar{n}_{ab}^*) - \hat{\mathbf{p}} \cdot (\mathbf{f}_{ab} - \bar{\mathbf{f}}_{ab}^*)], \quad (\text{Eq. 4.1.4})$$

Einstein summation convention is assumed. And n_{ab} and \mathbf{f}_{ab} are the neutrino number density and flux defined as

$$n_{ab} = \frac{1}{c^3} \int d\hat{\mathbf{p}} \int dp p^2 f_{ab} \quad (\text{Eq. 4.1.5})$$

$$\mathbf{f}_{ab} = \frac{1}{c^3} \int d\hat{\mathbf{p}} \int dp p^2 f_{ab} \hat{\mathbf{p}} \quad (\text{Eq. 4.1.6})$$

where f_{ab} is the neutrino distribution function matrix defined in section 2.5. n_a represent the lepton number density of flavors $a = e, \mu, \tau$.

To compute the flavor Hamiltonian of every computational particle in the simulation, it is necessary to know the neutrino and antineutrino number density and flux at every computational particle position, as can be observed in equations 4.1.2, 4.1.3 and 4.1.4. This is an easy task in a continuous neutrino and antineutrino field. However, in the discrete approximation used in EMU, it is necessarily a process of interpolation of the neutrino and antineutrino number density and flux at every computational particle position.

For this reason, EMU divides the simulation spatial domain into a background grid. The collection of computational particles moves through the grid cells.

To compute the neutrino and antineutrino number density and flux at every computational particle position, EMU performs two procedures: a deposition and an interpolation.

In the deposition algorithm, EMU constructs a neutrino and antineutrino distribution for each cell of the grid. To do this, each computational particle is modeled with an extended shape function. This means that all computational particles will represent a distribution of neutrinos and antineutrinos that spread over a spatial domain comparable to each grid cell. In this work, the computational particle's shape function is a quadratic function of its position.

The deposition algorithm used in the EMU is represented graphically in Figure 4.1. Each computational particle $i = 1, 2, 3, \dots$ contributes to each cell distribution j in a proportion given by the weight w_{ij} . The weight is given by the shape function at the cell center position. The sum of the weight w_{ij} of the particle i in all affected cells j is defined 1, which means that w_{ij} is the fraction of the particle i that contributes to the grid cell j . In this form, the j cell distribution is constructed with the following set of equations:

$$\begin{aligned} n_{\nu,j} &= \frac{1}{\Delta V} \sum_i N_i w_{ij} \rho_i \\ \bar{n}_{\nu,j} &= \frac{1}{\Delta V} \sum_i \bar{N}_i w_{ij} \bar{\rho}_i \\ \mathbf{f}_{\nu,j} &= \frac{1}{\Delta V} \sum_i N_i w_{ij} \rho_i \hat{\mathbf{p}}_i \\ \bar{\mathbf{f}}_{\nu,j} &= \frac{1}{\Delta V} \sum_i \bar{N}_i w_{ij} \bar{\rho}_i \hat{\mathbf{p}}_i \end{aligned} \quad (\text{Eq. 4.1.7})$$

where ΔV is the cell volume and i runs over all computational particles.

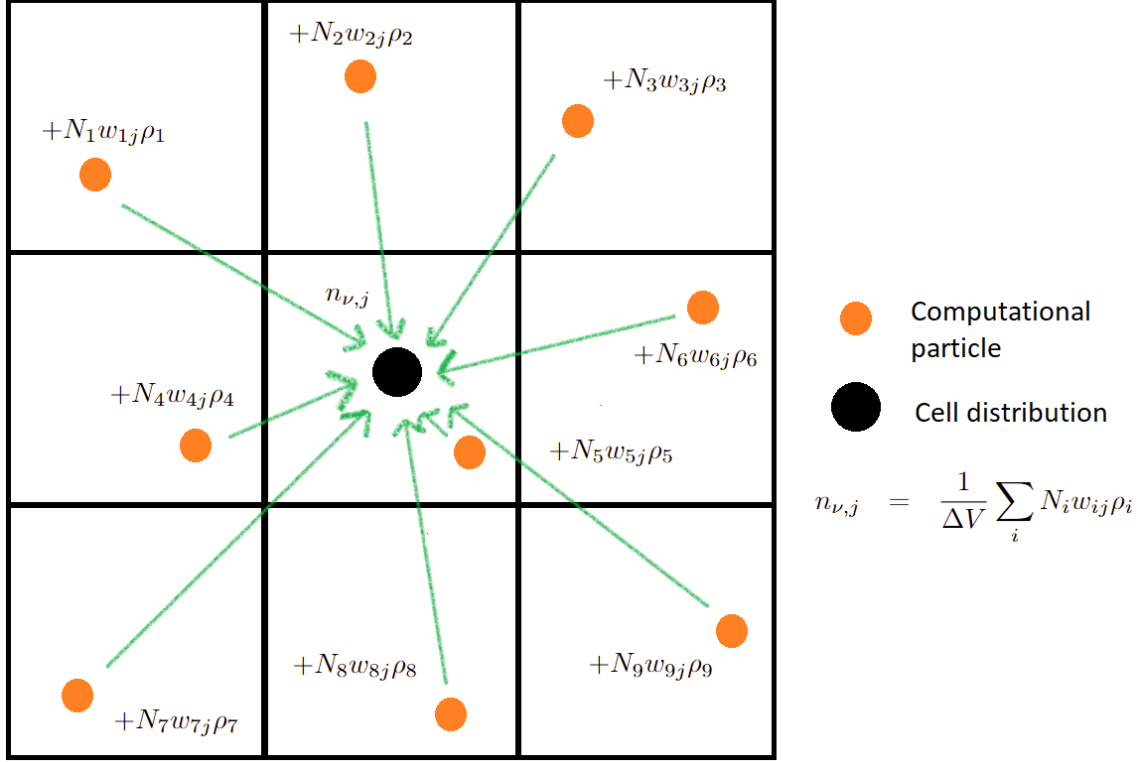


Figure 4.1: Deposition algorithm: Process of construction of the cell’s neutrinos and antineutrinos distribution. Each computational particle (orange dots) is modeled by an extended quadratic shape function that depends on the coordinates. Given by the shape function, every computational particle i contributes a fraction w_{ij} of their particles to the cell distribution j (black dot). In this form, the neutrinos and antineutrinos number density and flux at each cell are given by the equation 4.1.7.

Once the distribution of each cell (neutrinos and antineutrinos number density and flux) is obtained from the deposition algorithm, it is possible to interpolate the neutrino number density and flux to the position of each computational particle. For this proposal, EMU uses an interpolation algorithm (See figure 4.2 for a graphic representation).

To interpolate the neutrino and antineutrino number flux at the position of a computational particle i , the interpolation algorithm runs over each cell distribution j , adding a fraction w_{ij} of the cell’s neutrino and antineutrino number and flux density. This procedure is mathematically represented in EMU with the following equations:

$$\begin{aligned}
 n_{\nu,i} &= \sum_j w_{ij} n_{\nu,j} \\
 \bar{n}_{\nu,i} &= \sum_j w_{ij} \bar{n}_{\nu,j} \\
 \mathbf{f}_{\nu,i} &= \sum_j w_{ij} \mathbf{f}_{\nu,j} \\
 \bar{\mathbf{f}}_{\nu,i} &= \sum_j w_{ij} \bar{\mathbf{f}}_{\nu,j}
 \end{aligned}
 \tag{Eq. 4.1.8}$$

where j runs over each cell on the grid.

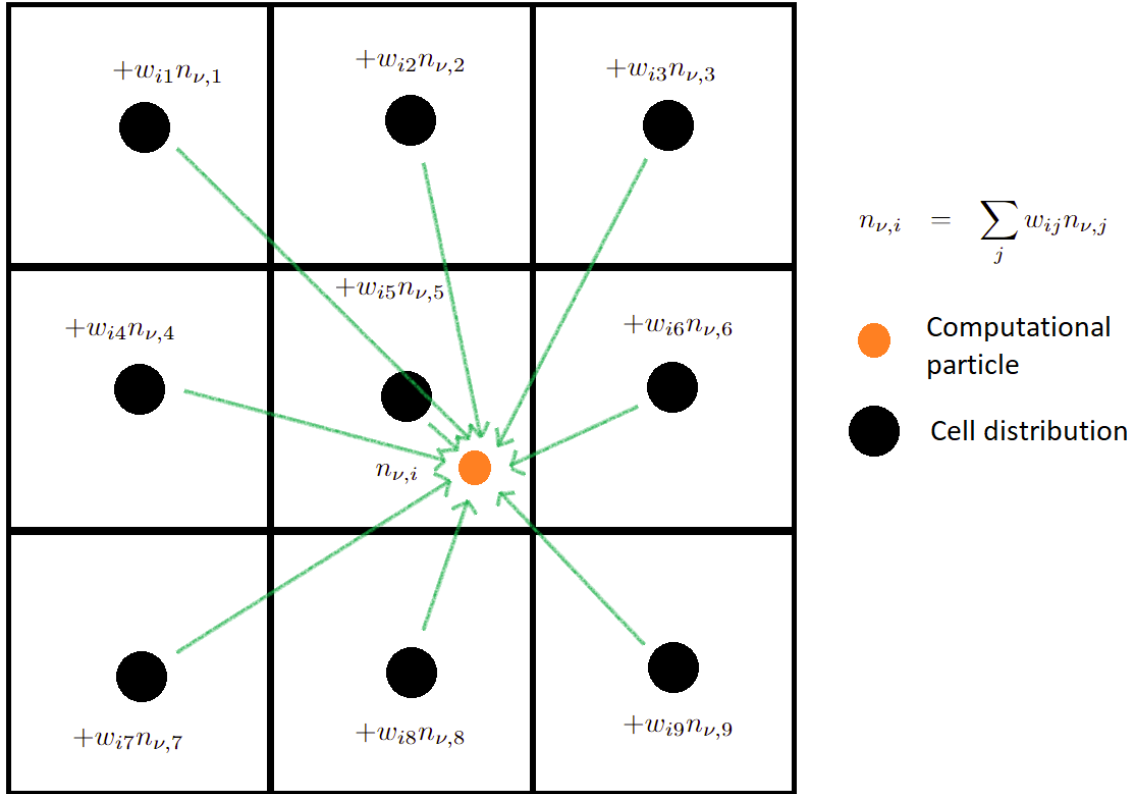


Figure 4.2: Interpolation algorithm: To compute the neutrinos and antineutrino’s number density and flux at the computational particle i location, the interpolation algorithm runs over each cell distribution j adding a fraction w_{ij} of the cell’s neutrino and antineutrino number density and flux. This procedure is mathematically represented in EMU with the equations 4.1.8.

In this way, it is possible to compute the neutrino and antineutrino numbers and flux density at each computational particle position, as well as the neutrino-neutrino flavor Hamiltonian in equation 4.1.4. In each time step, the deposition and interpolation algorithms are repeated to evolve the neutrino quantum kinetic equations 4.1.1.

The last description is implemented in the EMU code in an efficient and scalable manner, based on the AMReX framework for performance portable to CPU and GPU hardware. More details about EMU can be found in the reference [24].

Chapter 5

Results and discussion

5.1 One dimension fiducial simulation

In this section, I will discuss the one-dimensional fiducial simulation presented in reference [24], my motivation for this simulation is to have a test problem with known results. The input parameters of this simulation are publicly available in the GitHub repository of the EMU code¹.

In this simulation, neutrinos and antineutrinos exhibit strong electron-lepton number crossing. One-third of the total number of neutrinos and antineutrinos traveling in opposite directions. This system has shown strong fast flavor instabilities that match the unstable modes predicted by linear stability analysis.

In this simulation, I consider a $1 \times 1 \times 64$ cm domain that is partitioned into 1024 cells in the \hat{z} direction. Previous work showed that the one-dimensional results are robust in comparison with the computationally expensive three-dimensional simulation [46]. In order to have a numerically consistent analysis (see Appendix: Convergence test), I chose to simulate 24,088 computational particles that are released from the center of each cell with directions distributed approximately isotopically. The electron neutrino and antineutrino densities were chosen to be 4.89×10^{32} cm⁻³ and zero for muon and tau neutrinos and antineutrinos, respectively. The reason for this choice is that the fastest growing mode of a two-beam model with these neutrino densities has a wavelength of 1 cm, as mentioned in the reference [24].

The number of physical neutrinos and antineutrinos that a computational particle represents is set by the following equation:

$$N_p = \frac{1}{N_{\text{ppc}}} (n_{\text{input}} + 3\mathbf{f}_{\text{input}} \cdot \hat{\mathbf{p}}) \Delta V \quad (\text{Eq. 5.1.1})$$

$$\bar{N}_p = \frac{1}{N_{\text{ppc}}} (\bar{n}_{\text{input}} + 3\bar{\mathbf{f}}_{\text{input}} \cdot \hat{\mathbf{p}}) \Delta V, \quad (\text{Eq. 5.1.2})$$

where n_{input} (\bar{n}_{input}) is the neutrino(antineutrino) density, $\mathbf{f}_{\text{input}}$ ($\bar{\mathbf{f}}_{\text{input}}$) is the neutrino(antineutrino) flux density established to be $\mathbf{f}_{\text{input}} = n_{\text{input}}\hat{\mathbf{z}}/3$ and $\bar{\mathbf{f}}_{\text{input}} = -\bar{n}_{\text{input}}\hat{\mathbf{z}}/3$, N_{ppc} is the number of computational particles per cell. This generates an anisotropic neutrino distribution based on an isotropic distribution of computational particles.

The initial flavor state of each computational particle is considered to be nearly in the pure electron state with a small random perturbation on the non-diagonal component of the density matrix as follows:

$$\rho = \begin{bmatrix} 1 - \epsilon_\mu - \epsilon_\tau & \alpha(U + Ui) & \alpha(U + Ui) \\ \rho_{e\mu}^* & \epsilon_\mu & 0 \\ \rho_{e\tau}^* & 0 & \epsilon_\tau \end{bmatrix}, \quad (\text{Eq. 5.1.3})$$

¹<https://github.com/AMReX-Astro/Emu>

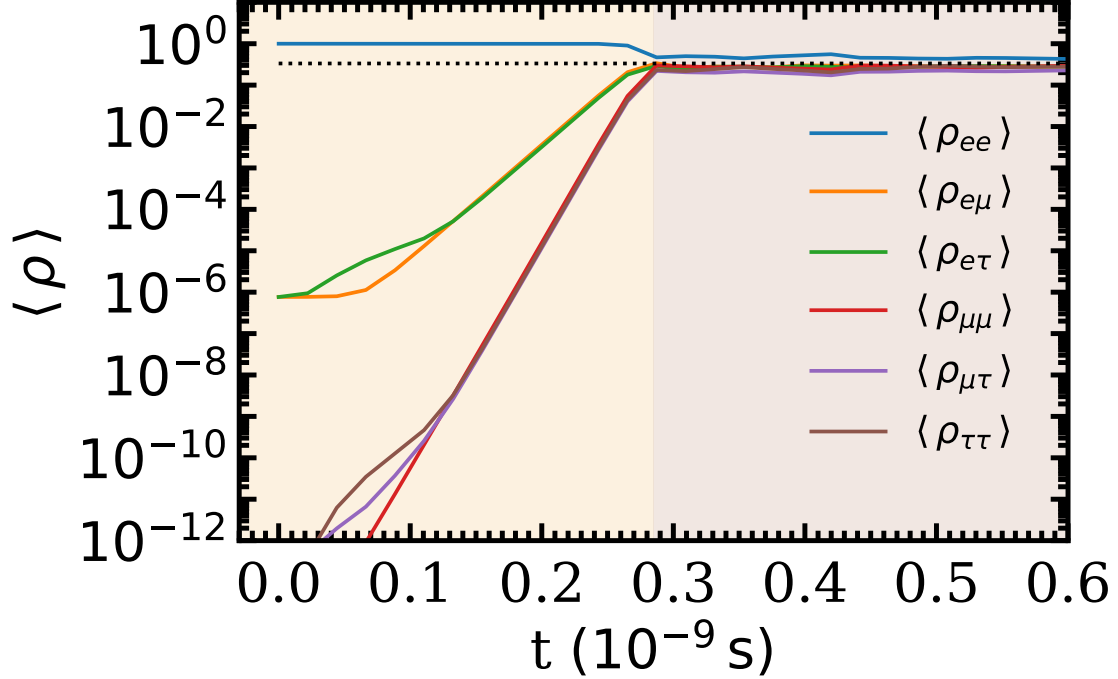


Figure 5.1: Time evolution of the neutrino's density matrix components averaged over the entire domain in the one-dimensional fiducial simulation. The yellow area describes the linear regime in which the unstable modes grow exponentially matching the prediction of the linear stability analysis. The gray area represents the non-linear regime in which the system approximately reaches the flavor equilibrium (black dotted line). The antineutrino density matrix components averaged over the entire domain follow the same trend.

$$\bar{\rho} = \begin{bmatrix} 1 - \epsilon_\mu - \epsilon_\tau & \alpha(U + Ui) & \alpha(U + Ui) \\ \bar{\rho}_{e\mu}^* & \epsilon_\mu & 0 \\ \bar{\rho}_{e\tau}^* & 0 & \epsilon_\tau \end{bmatrix}, \quad (\text{Eq. 5.1.4})$$

where U is a random number between -1 and 1 generated each time it appears and α is the strength of the random perturbation, which is set to be 10^{-6} . ϵ_μ and ϵ_τ are computed once the random non-diagonal components are generated in order to satisfy the conservation of the length of the flavor polarization vector and the unit trace of the density matrix.

Although the timescale of this simulation is too short for vacuum neutrino oscillation to be observed, I included it for completeness. As in reference [24], I consider the vacuum term in the flavor Hamiltonian setting the mixing angles of the PMNS mixing matrix as $\theta_{12} = 10^{-6}$, $\theta_{23} = 8.61$ and $\theta_{13} = 48.3$ degrees. The charge-parity violation phase was settled at 222 degrees [103]. The neutrino propagation eigenstate masses were established to be $m_1 = m_2 = 0$ and $m_3 = 0.0495$ eV. All neutrinos were considered to have an energy of 50 MeV.

In Figure 5.1 the components of the density matrix are plotted averaged over the entire domain. For the purpose of this study, I will divide the neutrino flavor evolution into two phases: the linear and non-linear regimes represented by the yellow and gray areas, respectively.

In the linear regime (yellow area), the small amplitude of unstable modes grows exponentially as predicted by the linear stability analysis [24]. The non-diagonal components of the domain averaged density matrix start to behave linearly in the logarithmic plot after 0.1 ns. This exponential trend of the small unstable modes eventually reaches saturation when their amplitudes grow sufficiently to leave the linear regime at approximately 0.28 ns. At this point, the non-diagonal components of

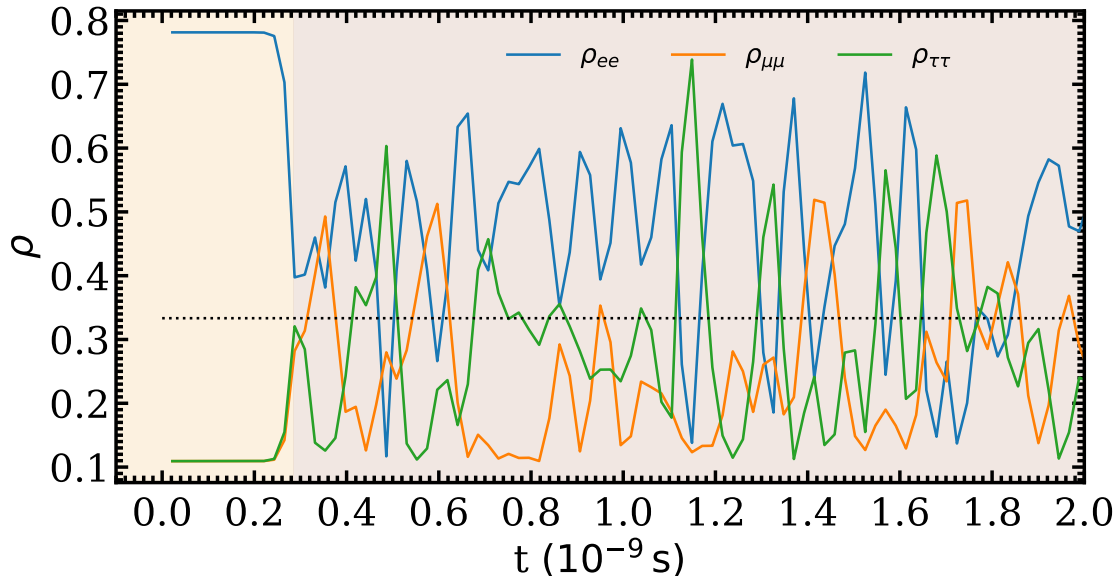


Figure 5.2: Time evolution of the neutrino’s density matrix diagonal components of a single computational particle. The yellow and gray regions represent the linear and non-linear regimes, respectively. In the non-linear regime, the flavor transformation is highly stochastic. Contrary to the behavior of the averaged density matrix components, individual particles exhibit larger oscillation amplitudes around the flavor equipartition (black dotted line). The antineutrino’s density matrix diagonal components follow the same trend.

the density matrix are approximately of the same order of magnitude as the diagonal components. The presence of fast flavor instability is a necessary but not sufficient condition for flavor conversion to occur [8]. In this simulation, the fast flavor instability results in a large flavor conversion from electron to muon and tau neutrinos in approximately 0.28 ns.

In the non-linear regime (gray area in Figure 5.1), the diagonal components of the domain-averaged density matrix approximate the flavor equipartition at late times (black dotted line in Figure 5.1) reaching an asymptotic behavior around the following values:

$$\begin{aligned}
 \langle \rho_{ee} \rangle &\approx 0.35 \\
 \langle \rho_{\mu\mu} \rangle &\approx 0.33 \\
 \langle \rho_{\tau\tau} \rangle &\approx 0.32,
 \end{aligned}
 \tag{Eq. 5.1.5}$$

the diagonal components of the domain-averaged density matrix slightly oscillate randomly around these values.

In Figure 5.2 the behavior of the diagonal components of the density matrix is shown for a single computational particle. The yellow and gray regions represent the linear and non-linear regimes, respectively. The flavor transformation became noticeable in the final part of the linear regime, when the unstable modes saturated. In the non-linear regime, the stochastic behavior of the flavor became the main effect. Contrary to Figure 5.1 in which the density matrix averaged over the entire domain slightly oscillates approximately around the flavor equipartition, individual particles experience flavor transformation with large amplitudes.

The highly stochastic behavior of the density matrix component of a single particle in the one dimensional fiducial simulations gives us valuable insight about the complexity of the neutrino flavor states. Quantitatively, the complexity has a strong relationship with the sensitive dependence on the initial condition and can be measured by computing the difference between two one-dimensional

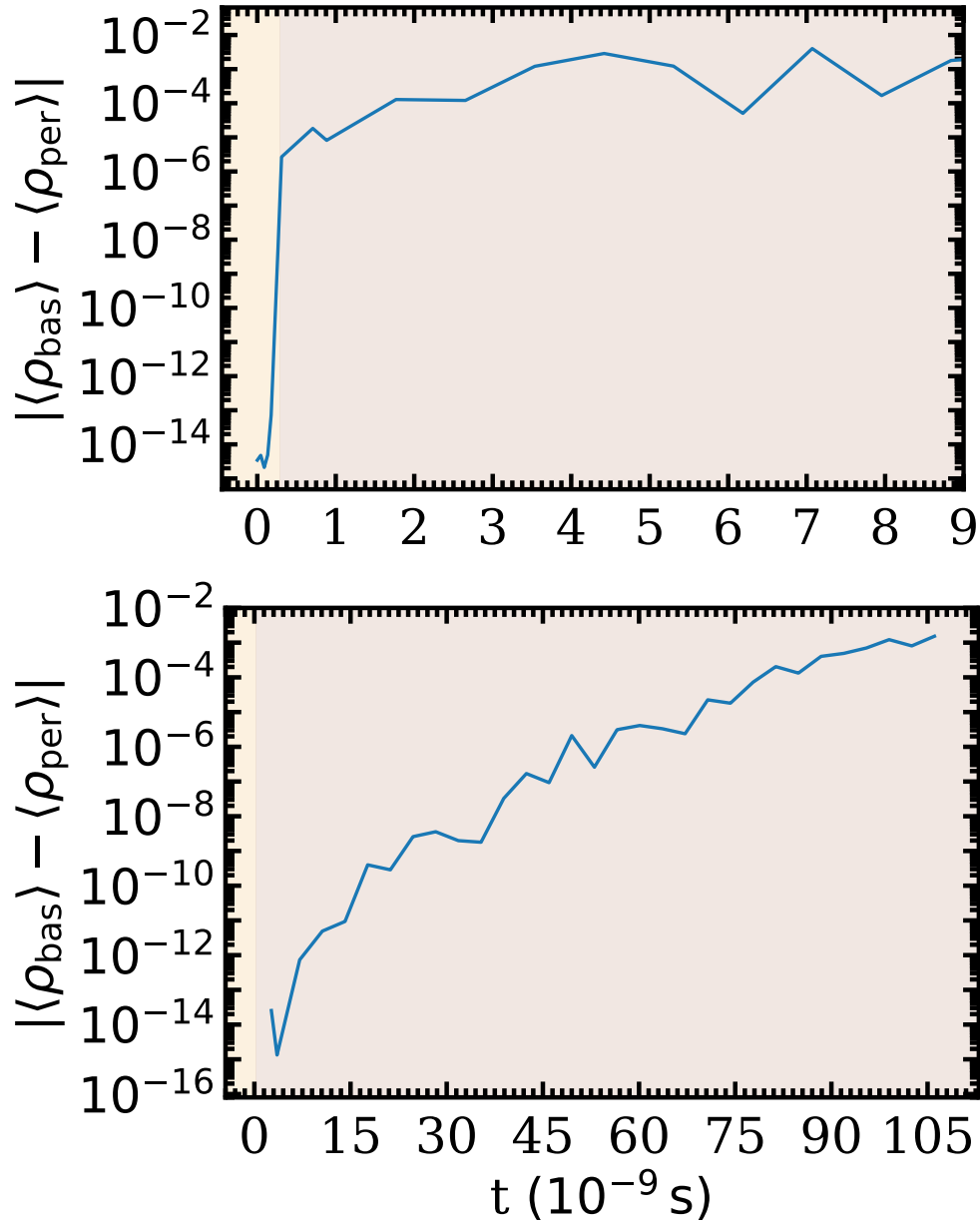


Figure 5.3: Difference between the domain-averaged electron components of the density matrix of two one dimensional fiducial neutrino simulations with close flavor initial conditions. The yellow and gray shaded areas represent the linear and non-linear regimes, respectively. In the upper panel, both simulations started with a close initial condition at $t = 0$ ns (linear regime). The main tendency is established by the exponential growth of fast unstable modes. In the lower panel, both simulations started with a close initial condition at $t = 2.7$ ns (non-linear regime). The main trend is an exponential divergence. This suggests the neutrino system is highly sensitive to the choice of the initial condition. The difference between the domain-averaged electron components reaches an asymptotic behavior in the upper and lower panels, reaching a maximum separation of the order of 10^{-2} . The others domain-averaged density matrix components showed the same tendency.

fiducial simulations with close initial conditions. In the top and bottom panels of Figure 5.3 I plot the absolute value of the difference between the domain-averaged electron components of the density matrix $|\langle\rho_{\text{bas}}\rangle - \langle\rho_{\text{per}}\rangle|$ of two simulations with close initial conditions. The baseline simulation $\langle\rho_{\text{bas}}\rangle$ is the one-dimensional fiducial simulation described in the last paragraphs, and the perturbed simulation $\langle\rho_{\text{per}}\rangle$ is the baseline simulation plus a random perturbation of amplitude 10^{-6} in each component of the density matrix of all computational particles. In Figure 5.3, I am looking for an exponential behavior, as this is a signal of sensitive dependence on the initial condition and chaos (see Section 3.3).

In the upper panel of Figure 5.3 the initial difference between the domain-averaged electron components of the density matrix is 3.4×10^{-15} at $t = 0$ ns. In the linear regime (first 0.29 ns), the growth of fast unstable modes is the dominant behavior. The main tendency is an exponential behavior with a rate of $1.3 \times 10^{10} \text{ s}^{-1}$. However, this exponential behavior can not be assigned to the sensitive dependence on the initial condition, as chaos emerges only in the non-linear regime of the equations. Finally, the difference between the domain-averaged electron component of the density matrix reaches an asymptotic behavior that oscillates randomly between 10^{-4} and 10^{-2} .

In the upper panel of Figure 5.3 is not clearly appreciated the behavior of the difference between the domain-averaged electron components in the non-linear regime because the solutions reach the maximum separation just after leaving the linear regime. To study the behavior of the solutions in the non-linear regime I compute the difference between the domain-averaged electron components of the density matrix of two one-dimensional fiducial simulations with close flavor initial conditions starting at $t = 2.7$ ns (see the lower panel of Figure 5.3). At this time, fast unstable modes that grow exponentially in time are not present in the simulation. The initial difference between the domain-averaged electron component of the simulations at $t = 2.7$ ns is 2.5×10^{-14} . After 100 ns, the difference between the electron components averaged in the domain increases by the 10 order of magnitudes in an approximately exponential trend (a line in the logarithmic plot). The exponential growth rate is around $2.2 \times 10^8 \text{ s}^{-1}$.

The exponential divergence tendency observed in the domain-averaged electron component of the density matrix in the lower panel of Figure 5.3 suggests the neutrino system is highly sensitive to the flavor initial conditions. Although this result is not conclusive because the domain-averaged electron component of the density matrix is not an exact representation of the entire flavor state of the neutrinos in the system, it provides valuable information about the maximum impact of the initial condition in the final domain-averaged components of the density matrix

$$|\langle\rho_{\text{bas}}\rangle - \langle\rho_{\text{per}}\rangle|_{ij}^{\text{max}} \sim |\langle\bar{\rho}_{\text{bas}}\rangle - \langle\bar{\rho}_{\text{per}}\rangle|_{ij}^{\text{max}} \sim 10^{-2}. \quad (\text{Eq. 5.1.6})$$

This result is independent of the choice of the initial difference between the domain-averaged components of the density matrix.

In the next section, I will simulate the neutrino flavor transformation inside a small domain of neutron star mergers. To study the dependence of the system on the initial conditions, instead of using the domain-averaged components of the density matrix, I will consider a neutrinos flavor vector that uniquely defines the complete flavor state of the entire system.

5.2 Neutron star merger simulation

Here, I consider the realistic neutrino condition of the neutron star merger simulation studied in reference [56]. Reference [56] examined the neutrino momentum distribution of the neutron star merger remnant produced in the classical global general relativistic two-moment radiation hydrodynamics simulation in Reference [139]. As in Reference [56] I extracted the neutrino conditions in a small cube of 7.86 cm size. The region of neutron star merger chosen exhibited a crossing in the lepton angular distribution, that is, at least one angular direction in which the flux of neutrinos and antineutrinos are equal. This allows the appearance of fast flavor instabilities [114].

The densities and fluxes directions of neutrinos and antineutrinos in the simulation are the following:

$$\begin{aligned}
N_{ee} &= 1.422 \times 10^{33} \text{ cm}^{-3} \\
\bar{N}_{ee} &= 1.915 \times 10^{33} \text{ cm}^{-3} \\
N_{\mu\mu} &= 4.913 \times 10^{32} \text{ cm}^{-3} \\
\bar{N}_{\mu\mu} &= 4.913 \times 10^{32} \text{ cm}^{-3} \\
N_{\tau\tau} &= 4.913 \times 10^{32} \text{ cm}^{-3} \\
\bar{N}_{\tau\tau} &= 4.913 \times 10^{32} \text{ cm}^{-3} \\
\mathbf{f}_{ee} &= (0.0974 \ 0.0421 \ 0.1343) \\
\bar{\mathbf{f}}_{ee} &= (0.0723 \ 0.0313 \ 0.3446) \\
\mathbf{f}_{\mu\mu} &= (0.0216 \ 0.0743 \ 0.5354) \\
\bar{\mathbf{f}}_{\mu\mu} &= (0.0216 \ 0.0743 \ 0.5354) \\
\mathbf{f}_{\tau\tau} &= (0.0216 \ 0.0743 \ 0.5354) \\
\bar{\mathbf{f}}_{\tau\tau} &= (0.0216 \ 0.0743 \ 0.5354)
\end{aligned} \tag{Eq. 5.2.1}$$

I will use the same angular distribution as in the reference [56]. There, the lepton angular distributions were chosen to satisfy the classical maximum entropy closure [140]. This maximizes the angular entropy of the energy-integrated distribution constrained to a given number density and flux of each neutrino species in the following relation:

$$f(\vec{x}, \vec{p}, t) \propto e^{Z \cdot \cos \theta}, \tag{Eq. 5.2.2}$$

where θ is the angle between the momentum direction and the direction of the total flux. Z is a factor that needs to be calculated to give the total flux its expected value.

To simulate this neutrino flavor evolution in EMU, I chose a one-dimensional array of $1 \times 1 \times 128$ cells. Each cell's center released neutrinos in 24,088 directions with a roughly isotropic distribution. The reason for this choice is to get convergence on the exponential growth rate between the two solutions (see Appendix: Convergence test). Each particle carries a number of neutrinos and antineutrinos that satisfy the angular distribution of neutrinos given by the maximum entropy closure for the neutron star merger densities and fluxes in Eq. 5.2.1.

In the same manner that the one-dimensional fiducial simulation. In the NSM simulation, a small random perturbation of amplitude 10^{-6} was added to the off-diagonal components of the density matrix of each particle. This was done to establish the initial amplitude of the unstable modes.

In this simulation, I do not consider the vacuum neutrino oscillation or the MSW mechanism because they are strongly suppressed by the neutrino-neutrino coherent forward scattering Hamiltonian at the high neutrino densities of the NSM. The average neutrino energy in the NSM condition was 20 MeV. However, fast flavor conversion is an energy-independent mechanism.

In Figure 5.4 I show the time evolution of the domain-averaged density matrix components. As previously, the yellow and gray areas represent the linear and non-linear regimes, respectively.

In the linear regime (yellow area), the existence of a crossing in the angular distribution of neutrinos and antineutrinos indicate the presence of the fast flavor instability and fast unstable modes. In Figure 5.4, are observed as the exponential growth of the off-diagonal components of the density matrix between 0.05 and 0.25 ns. This exponential divergence of the small unstable modes eventually reaches saturation when their amplitudes grow enough to leave the linear regime at approximately 0.25 ns. By this time, the diagonal and off-diagonal components of the density matrix were approximately of the same order of magnitude, exhibiting a large flavor conversion of neutrinos.

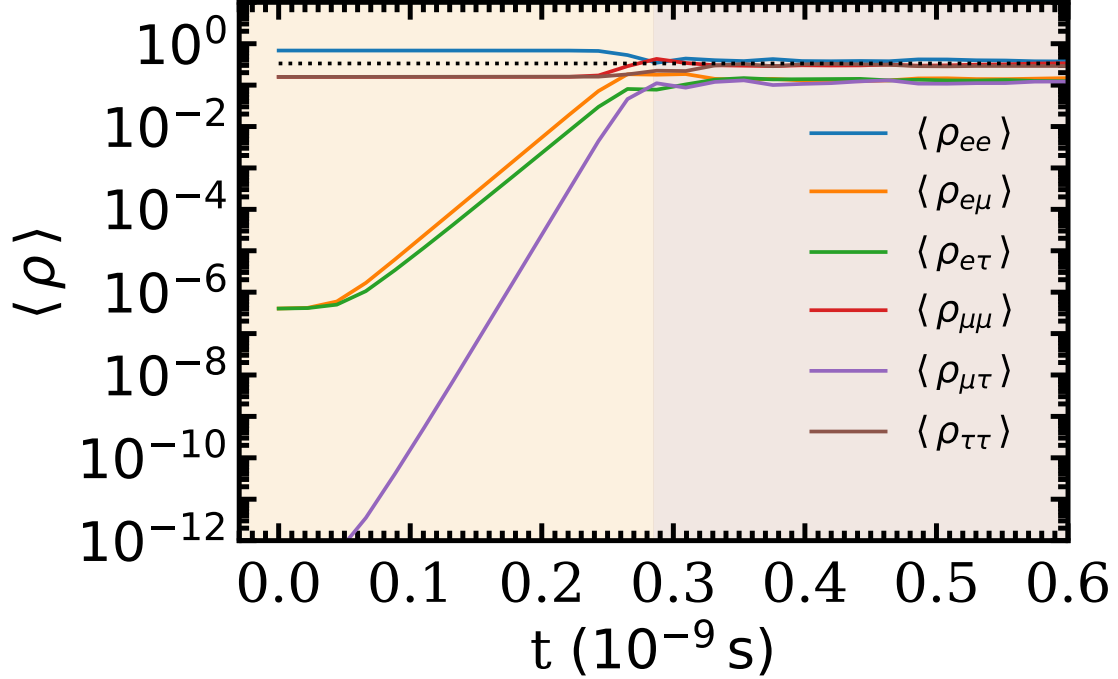


Figure 5.4: Behavior of the domain-averaged density matrix components for the NSM simulation. The yellow shaded area represents the linear regime in which the unstable modes grow exponentially according to the dispersion relation given by the linear stability analysis. The gray shaded area represents the non-linear regime in which the system reaches a flavor asymptotic behavior without completely reaching the flavor equipartition (black dotted line).

In the non-linear regime, the gray area in Figure 5.4, the domain-averaged diagonal component density matrix reaches an asymptotic behavior at late times. However, they never reach the flavor equipartition (black dotted line in Figure 5.1). The domain-averaged diagonal components slightly oscillate in a random manner around the following asymptotic values:

$$\begin{aligned}
 \langle \rho_{ee} \rangle &\approx 0.37 \\
 \langle \rho_{\mu\mu} \rangle &\approx 0.31 \\
 \langle \rho_{\tau\tau} \rangle &\approx 0.31.
 \end{aligned}
 \tag{Eq. 5.2.3}$$

The behavior of the diagonal components of the density matrix for a single computational particle in the NSM simulation is shown in Figure 5.5. As in the last figure, the yellow and gray shaded regions represent the linear and non-linear regimes, respectively. Noticeable flavor transformations are observed at the final part of the linear regime, when the unstable modes are saturated. The non-linear regime (gray shaded regions) is characterized by stochastic behavior of the flavor. In contrast to Figure 5.4 in which the density matrix averaged in the domain oscillates slightly around the asymptotic values of Eq. 5.2.3, the diagonal component of the density matrix of individual computational particles experiences flavor transformations with large amplitudes.

To test the stability of two NSM neutrino environments with nearly identical initial conditions, I defined the flavor state space vector as follows:

$$\vec{r} = \sum_i \sum_{\alpha, \beta} \rho_{\alpha\beta}^i \hat{e}_{\alpha\beta}^i,
 \tag{Eq. 5.2.4}$$

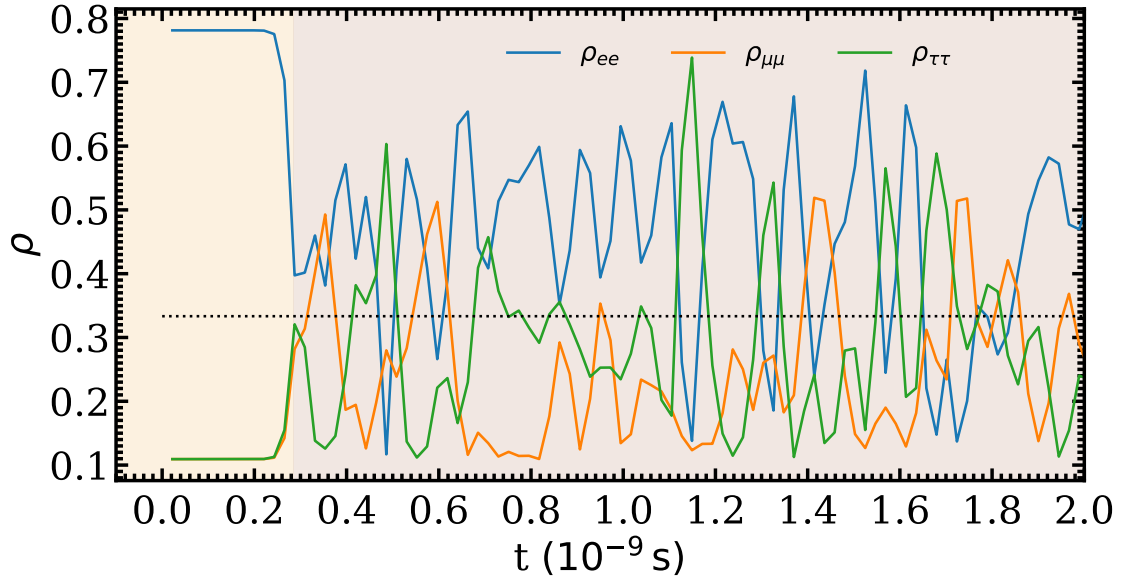


Figure 5.5: Time behavior of the diagonal components of the density matrix of a single computational particle in the NSM simulation. The linear and non-linear regimes are represented by the yellow and gray shaded regions, respectively. In the non-linear regime, the flavor transformation is highly stochastic. Contrary to the behavior of the averaged density matrix components, individual particles exhibit larger oscillation amplitudes approximately around the flavor equipartition (black dotted line).

where i runs over all the particles in the simulation and α and β run over the components of the upper part of the neutrino density matrix including the diagonal terms. This vector describes the complete flavor state of neutrinos in the neutron star merger simulation and will be used to quantify the impact of the initial conditions on the spatial distribution of the neutrino flavors as it provides a precise measurement of the difference between the flavor states of the perturbed and baseline simulation.

I ran two simulations. The first simulation, called the baseline simulation \vec{r}_{bas} , describes the neutron star merger's initial condition. The initial condition of the second simulation, called a perturbed simulation \vec{r}_{per} , is the baseline simulation plus a perturbation of amplitude 10^{-6} in a random direction

$$\vec{r}_{\text{per}}(t=0) = \vec{r}_{\text{bas}}(t=0) + 10^{-6} \cdot \hat{r}_{\text{random}}. \quad (\text{Eq. 5.2.5})$$

In Figure 5.6 the time evolution of the magnitude of the difference between the baseline and perturbed simulation $|\vec{r}_{\text{bas}} - \vec{r}_{\text{per}}|(t)$ is plotted. The yellow and gray shaded areas represent the linear and non-linear regimes, respectively.

In the linear regime, the difference between the two solutions stays approximately constant for the first 0.1 ns. After that, they start to diverge exponentially with a growth rate of $\lambda = 5.8 \times 10^{10} \text{ s}^{-1}$. This behavior stops at the end of the linear regime at approximately 0.25 ns and corresponds to the exponential growth of the unstable modes whose initial amplitudes were chosen randomly at the order of 10^{-6} . The exponential growth rate of the domain-averaged $\langle \rho_{e\mu} \rangle$ and $\langle \rho_{e\tau} \rangle$ components of the density matrix shown in the linear regime (yellow shaded area in Figure 5.4) are $\lambda = 6.1 \times 10^{10}$ and $\lambda = 5.8 \times 10^{10} \text{ s}^{-1}$, respectively. They are responsible for the dominant source of divergence in the linear regime. The exponential growth rate of $\langle \rho_{\mu\tau} \rangle$ is $\lambda = 11.9 \times 10^{10} \text{ s}^{-1}$. This is a factor of two higher than the other non-diagonal components [24]. The initial amplitude

of $\langle \rho_{\mu\tau} \rangle$ is zero and became comparable to the $\langle \rho_{e\mu} \rangle$ and $\langle \rho_{e\tau} \rangle$ only in the non-linear regime, this is why this fast exponential mode is not noticed in the difference between the baseline and perturbed simulation.

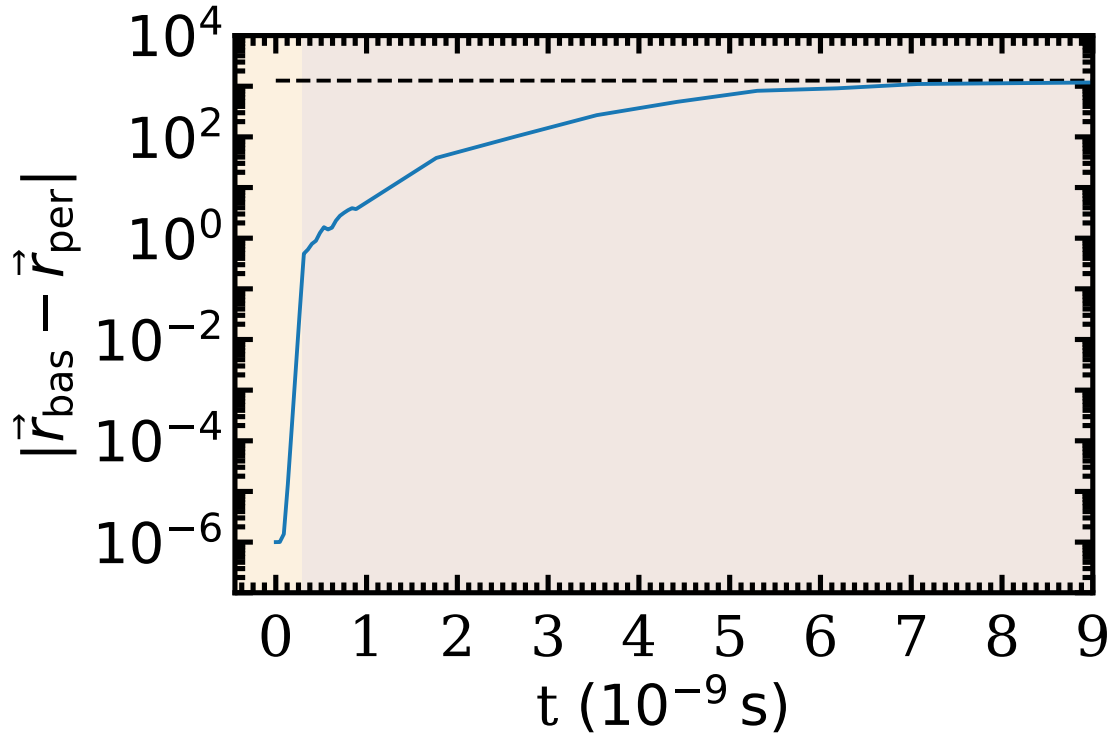


Figure 5.6: Divergence between two neutron star merger neutrinos simulations with close initial conditions. The yellow and gray shaded areas represent the linear and non-linear regimes, respectively. In the linear regime, the two neutrino solutions diverge exponentially following the fast unstable modes. In the non-linear regime, unstable modes saturate, stopping the exponential growth due to the fast flavor instability. However, the difference between the two neutron star merger neutrinos simulations continues to diverge exponentially at a lower rate between 0.25 and 1.8 ns. Finally, the solution reaches the maximum divergence value imposed by physical constraints (black dashed line).

Starting the non-linear regime, the baseline and perturbed simulations stop growing at an exponential rate of $5.8 \times 10^{10} \text{ s}^{-1}$ and start growing exponentially at a rate of approximately $2.8 \times 10^9 \text{ s}^{-1}$ until 1.8 ns. At this time in the nonlinear regime, the unstable modes are saturated, and the exponential growth rate of the unstable mode stops (see Figure 5.4 between 0.25 and 1.8 ns). At the same time, the domain-averaged diagonal components of the density matrix experience large flavor conversions, and single particles have already started to transform flavor in a stochastic manner (see Figure 5.5 between 0.25 and 1.8 ns). As the exponential growth rate can not be related to the fast unstable modes and the behavior of single computational particle is not exponential (it is mainly stochastic), the exponential difference between the two solutions must be a dynamical property of the flavor state space of the neutrino system.

After 1.8 ns in the nonlinear regime. The difference between the baseline and perturbed simulations starts an asymptotic tendency to the value of $|\vec{r}_{\text{bas}} - \vec{r}_{\text{per}}|(t \rightarrow \infty) = 1290$. This value represents the maximum divergence between two states as the vector \vec{r} is limited by the unitary constraint of each neutrino wave function. When the baseline and the perturbed simulation reach

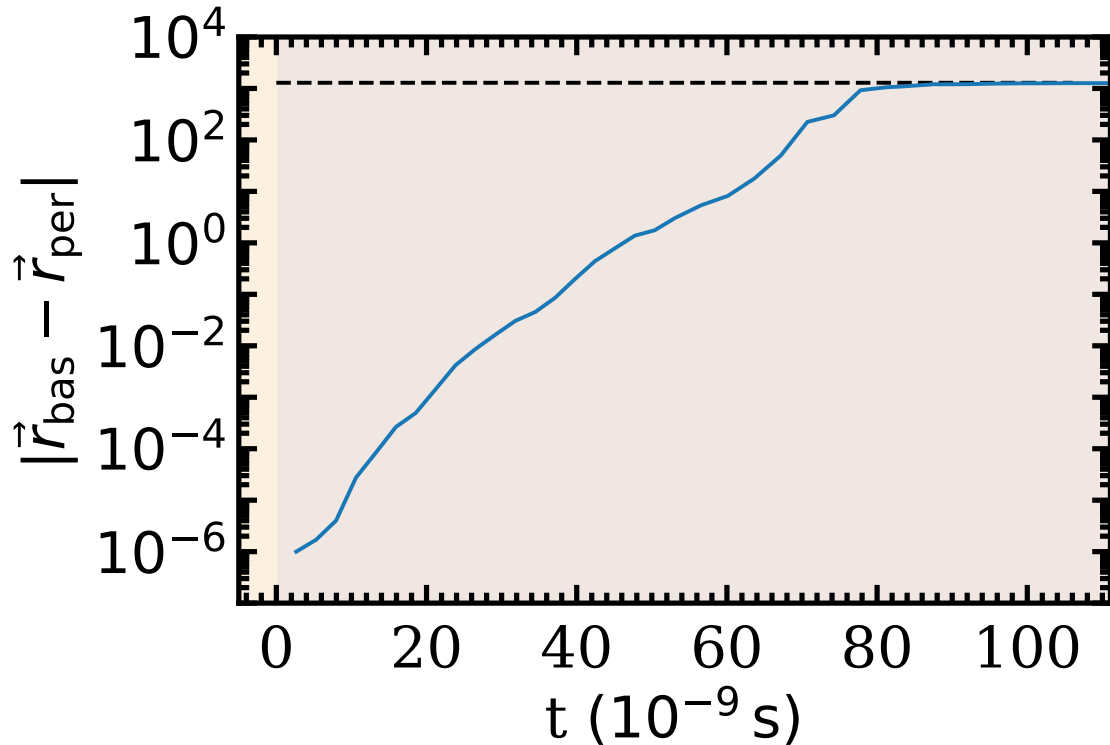


Figure 5.7: Divergence between two neutron star merger simulations with close initial conditions in the non-linear regime. At this time, the unstable modes are saturated and have stopped growing exponentially. The stochastic neutrino flavor transformations are the dominant phenomenon. The difference between the two close initial condition neutron star merger simulations grows exponentially, proving the unstable dynamics of the initial condition of the neutron star merger neutrinos system.

the asymptotic behavior, the magnitude of the flavor vector states \vec{r}_{bas} and \vec{r}_{per} are characterized by the following values:

$$\begin{aligned} |\vec{r}_{\text{bas}}|(t \rightarrow \infty) &\approx 1744 \\ |\vec{r}_{\text{per}}|(t \rightarrow \infty) &\approx 1744, \end{aligned}$$

this implies that an initial uncertainty of 10^{-6} on the initial flavor neutrino state vector \vec{r}_{bas} will grow until reach a maximum uncertainty of 44% after 8 ns.

To better understand the dynamics of the divergence between two neutron star merger simulations with close initial conditions, I will avoid the presence of unstable modes that grow exponentially in time by considering two nearby initial conditions in the non-linear regime of the neutron star merger neutrinos simulation. The main idea of this decision is to remove the instability-driven exponential growth in order to isolate chaos-driven exponential growth.

In Figure 5.7, I restarted two simulations in the non-linear regime at 2.65 ns. The baseline simulation describes the neutron star merger simulation. The perturbed simulation describes the baseline simulation plus a perturbation of amplitude 10^{-6} in a random direction

$$\vec{r}_{\text{per}}(t = 2.65 \text{ ns}) = \vec{r}_{\text{bas}}(t = 2.65 \text{ ns}) + 10^{-6} \cdot \hat{r}_{\text{random}}. \quad (\text{Eq. 5.2.6})$$

The difference between the two solutions (see Figure 5.7) grows exponentially (linear behavior in the logarithmic plot) with a rate of $2.6 \times 10^8 \text{ s}^{-1}$. This behavior stops approximately at 80 ns

when the difference between the two solutions reaches the maximum value. Figure 5.7 shows that the dynamics of the neutron star merger neutrinos simulations are highly sensitive and unstable to the initial condition and chaotic.

The impact of this exponential divergence rate on a single particle in the PIC simulation is shown in Figure 5.8. There, going from the top to the bottom panel is shown the behavior of the diagonal components of the density matrix (ρ_{ee} , $\rho_{\mu\mu}$ and $\rho_{\tau\tau}$). The dotted blue and orange lines are the diagonal components of the baseline and the perturbed simulation, respectively. The solid black line is the absolute value of the difference between each component of the density matrix ($\Delta\rho_{\alpha\alpha} = |\rho_{\alpha\alpha}^{\text{bas}} - \rho_{\alpha\alpha}^{\text{per}}|$, $\alpha = e, \mu$ and τ). In the bottom panel it is plotted the sum of the difference of all the diagonal components of the density matrix ($\Delta\rho_{ee} + \Delta\rho_{\mu\mu} + \Delta\rho_{\tau\tau}$) between the baseline and perturbed simulation.

The baseline and perturbed simulations stay close to each other for the first 65 ns as can be observed in Figure 5.8 (linear vertical scale). However, the difference between all of the density matrix components grows exponentially with approximately the same exponential growth rate as in Figure 5.7. After 65 ns the difference between the baseline and perturbed density matrix component reached the order of magnitude of 10^0 and the difference between the blue and orange dotted lines became evident in the linear scale of Figure 5.8.

The difference between the electron diagonal components reaches a maximum value of 0.43. The maximum muon diagonal component is approximately 0.63. The maximum tau diagonal component reaches a maximum difference of 0.63. This implies a high uncertainty in the diagonal component of the density matrix after the first 65 ns of the neutron star merger neutrino flavor evolution. This is also evident in the bottom panel of Figure 5.8. There, the sum of the difference of the diagonal components of the density matrix ($\Delta\rho_{ee} + \Delta\rho_{\mu\mu} + \Delta\rho_{\tau\tau}$) approximates the order of magnitude of 10^0 at 65 ns. As the value of the sum of the diagonal components of the density matrix is one, we can conclude that an initial uncertainty of 10^{-6} in the neutron star merger flavor state will lead to 100% uncertainty in the diagonal components of the density matrix of a single computational particle after approximately 100 ns.

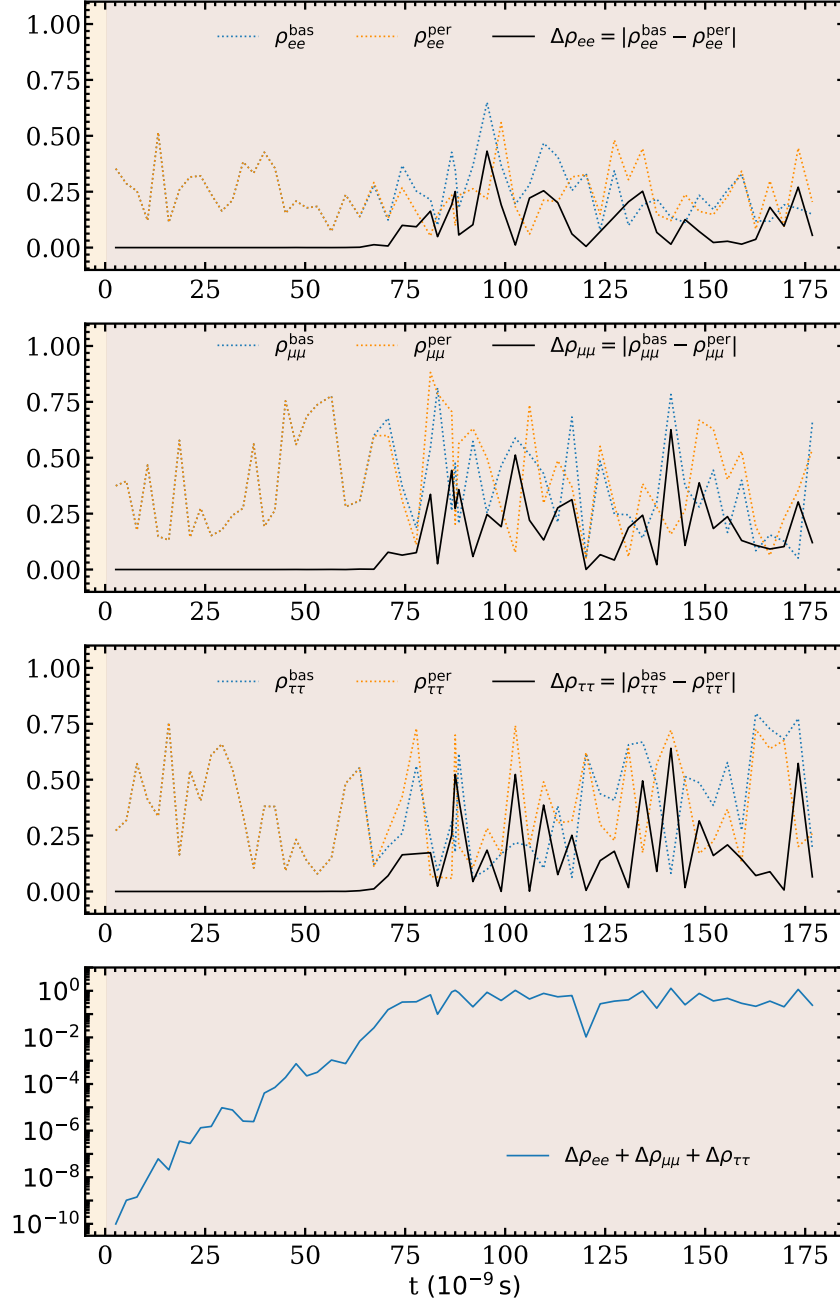


Figure 5.8: Absolute difference between the diagonal components of the density matrix for a single particle in the neutron star merger PIC simulation. Although it is not appreciable in the linear vertical domain of the figures, the difference between each of the diagonal density matrix components grows exponentially in time. At approximately 65 ns the difference between each component reached an order of magnitude of 10^0 and became appreciable in the plots. In the bottom panel, the sum of the absolute value of the difference between each density matrix component is plotted. At approximately 75 ns the uncertainty between the sum of the diagonal components of the density matrix reaches the value of one, implying a 100% uncertainty.

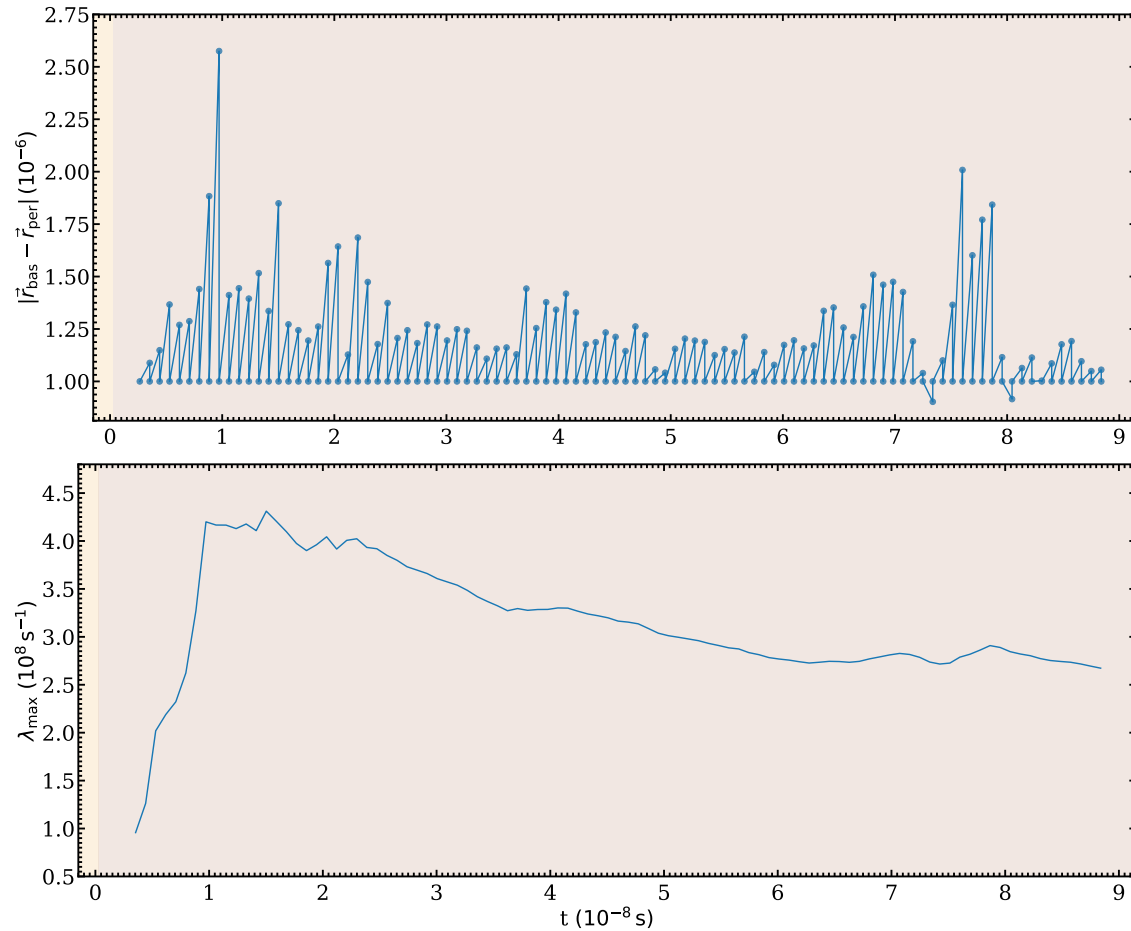


Figure 5.9: Top panel: Spectrum of the divergence rate between two neutron star merger neutrino simulations with close initial conditions. Both simulations start evolving in time at 2.65 ns with a difference between them of 10^{-6} . The difference between the two solutions is normalized each 0.9 ns conserving the direction. This corresponds to the Bennettin algorithm to compute the maximum Lyapunov exponent [3]. However, we are mostly interested in the initial trend of the difference between the two solutions. The spectrum showed divergence and convergence directions between the neutrino solutions with close initial conditions. The existence of directions of divergence (positive Lyapunov exponents) in the neutrino flavor state space is clear proof of chaos in the neutrino flavor evolution. Lower panel: Maximum Lyapunov exponent estimation (Eq. 5.2.8). The maximum Lyapunov exponent can not be lower than 10^8 s^{-1} . Even when this plot is not conclusive about the value of the maximum Lyapunov exponent because only the initial trend of the simulations was considered, it provides a good estimation of the main initial divergence tendency of the solutions. The observed trend agreed with the existence of positive Lyapunov exponents and chaos.

In the top panel of Figure 5.9 can be observed how the exponential growth rate of the divergence between the baseline and perturbed simulation changes in time. The main objective of this plot is to simulate the Bennettin algorithm to find the maximum Lyapunov exponent of a chaotic system [3]. For this analysis, I ran two simulations. The baseline solution corresponds to the neutron star merger neutrinos. The perturbed solution corresponds to the baseline simulation with the addition of a perturbation of amplitude 10^{-6} in a random direction. I restarted both simulations in the non-linear regime at 2.65 ns to avoid the presence of fast flavor unstable modes that grow exponentially in time.

Unlike the previous analysis in which I ran the baseline and perturbed simulation freely, I renormalized periodically each 0.9 ns the perturbed simulation to an amplitude of 10^{-6} preserving the direction of the vector between the baseline and the perturbed solutions

$$\vec{r}_{\text{per}}^{\text{ren}} = \vec{r}_{\text{bas}} + 10^{-6} \cdot \frac{\vec{r}_{\text{per}} - \vec{r}_{\text{bas}}}{|\vec{r}_{\text{per}} - \vec{r}_{\text{bas}}|}. \quad (\text{Eq. 5.2.7})$$

To get an overall estimate of the maximum Lyapunov exponent (see Section 3.3 for a discussion of chaos and its relation with positive Lyapunov exponent) the Bennettin algorithm [3] propose the following equation

$$\lambda_{\text{max}} = \frac{1}{t_n - t_0} \sum_{i=1,2,\dots}^n \ln \left(\frac{|\vec{r}_{\text{per}} - \vec{r}_{\text{bas}}|_{t=t_i}}{10^{-6}} \right). \quad (\text{Eq. 5.2.8})$$

In this case, $t_0 = 2.65$ ns and $|\vec{r}_{\text{per}} - \vec{r}_{\text{bas}}|_{t=t_i}$ is the difference between the baseline and the perturbed vectors before the perturbed simulation is renormalized at a time $t_i = 2.65 + 0.9i$ ns, where $i = 1, 2, 3, \dots$.

In the top panel of Figure 5.9 it is possible to see a broad spectrum of exponential growth rates. The highest exponential growth rate occurs at approximately 0.97×10^{-8} s and is around $10.7 \times 10^8 \text{ s}^{-1}$. The lowest exponential growth rate occurs at approximately 7.33×10^{-8} s and is around $-1.16 \times 10^8 \text{ s}^{-1}$.

This broad spectrum of exponential growth rates is expected because the neutrino N momentum quantum kinetic equation in equation 3.5.6 can be mapped to the classical Hamiltonian system in equation 3.5.8. For each canonical coordinate and momentum (see equation 2 of reference [80], in which the canonical variables are the polar coordinates and momentum that represent the flavor polarization vectors) it is expected to have a different Lyapunov exponent. One of the Lyapunov exponents is zero for each conserved quantity and all of them are zero for a stable or integrable system in which there exist as conserved quantities as degrees of freedoms. The Louville theorem claims that the state space volume of the canonical coordinates is a constant of motion, this implies that the spectrum of the Lyapunov exponents needs to be symmetric, as was previously exposed in Eq. 5.2.9 for the two-beam neutrino model and is generalized here as follows:

$$(\lambda_1, \lambda_2, \lambda_3, \dots, -\lambda_3, -\lambda_2, -\lambda_1).$$

This is the reason for the existence of the direction of convergence in Figure 5.9. However, the stable directions (negative Lyapunov exponents) in the neutrino flavor state space are dominated by the presence of the divergence direction (positive Lyapunov exponents), a simulation started in a stable direction will eventually move to a unstable one, this is the reason why unstable direction are most apparent. It is expected that the neutrino solution will end growing in the direction of maximum divergence.

The maximum exponent as calculated by Eq. 5.2.8 is plotted in the lower panel of Figure 5.9 for each renormalization done in the simulation shown in the top panel of Figure 5.9. This provides a good overall measurement of the main tendency of the initial divergence between the two solutions, which is approximately $3 \times 10^8 \text{ s}^{-1}$. This can be understood as a lower limit of the maximum Lyapunov exponent, whose order of magnitude satisfies the following relation:

$$\lambda_{\text{max}} > 10^8 \text{ s}^{-1}. \quad (\text{Eq. 5.2.9})$$

However, Figure 5.9 is not conclusive about the maximum Lyapunov exponent because only the initial divergence and convergence trend between the baseline and perturbed simulations were considered.

Chapter 6

Conclusion

Motivated by the high impact of the neutrino fast flavor transformation in the dynamics of core-collapse supernovae and the nucleosynthesis of heavy elements in binary mergers and earlier studies that claimed the neutrino bipolar flavor oscillation contained chaos, I simulated two dense neutrino systems including a distribution drawn from a neutron star merger simulation in a cube a few centimeters wide. My goal was to prove or disprove the existence of chaos in the evolution of neutrino flavors and to explain how chaos affects our capacity to forecast the neutrino flavor behavior in core-collapse supernovae and neutron star mergers. Using the particle-in-cell implementation of the neutrino quantum kinetic equations in the EMU code, I demonstrated that the neutrino flavor evolution is chaotic and highly dependent on the initial conditions. Due to positive Lyapunov exponents, the neutrino system showed an exponential divergence in the flavor space between nearby trajectories. Although the chaotic evolution of the neutrino flavor implies a huge uncertainty in the complete knowledge of the future flavor behavior of the system, the domain-averaged density matrix is not significantly impacted by chaos and can be used in global simulations of core-collapse supernovae and neutron star mergers that incorporate quantum neutrino transport.

In this work, the first simulation ran was the toy neutrino distribution widely investigated as the one-dimensional fiducial simulation in reference [24]. This neutrino distribution is characterized by having broad distribution of the neutrinos and antineutrinos traveling in opposite directions. I found that the off-diagonal components of the neutrino density matrix grew exponentially in the linear regime of the quantum neutrino transport equation (Figure 5.1), this corresponded to the appearance of fast flavor instabilities. There is a significant flavor conversion as a result of the fast flavor instability. Even when begun in the pure electron state, the domain averaged diagonal density matrix components achieved an approximate final asymptotic flavor equipartition in the non-linear regime. However, the density matrix diagonal component of each computational particle undergoes intricate, high-amplitude oscillation modes (Figure 5.2).

My main focus for the one-dimensional fiducial simulation was identifying the sensitive dependence on the initial condition of the domain-averaged density matrix components. The fast flavor instability had a significant impact on the absolute value of the difference between the domain-averaged density matrix components in the linear regime of the neutrino quantum kinetic equations. The predominant trend matched the exponential growth rate of fast unstable modes. In the non-linear regime of the solutions, the trend remained exponential but with a slower growth rate due to the absence of fast unstable modes (Figure 5.3).

The exponential trend observed in the domain-averaged density matrix components suggests the flavor state of the system is highly dependent on the initial condition. The highest possible value of the difference between each domain-averaged density matrix component was determined to be on the order of 10^{-2} . Future simulations of dense neutrino systems in core-collapse supernovae and binary mergers will heavily rely on this particular value. Based on a rough extrapolation in the simulation domain, the highest final uncertainty of the diagonal component of the neutrino

flavor density matrix will be around 1% when averaged over a 64 cm cube.

The second simulation involved a 7.86 cm cube containing neutrinos in a distribution extracted from a neutron star merger simulation. The neutrino and antineutrino angular distributions were approximated by a classical maximum entropy closure, this distribution exhibited a crossing in the angular distributions of neutrinos and antineutrinos and therefore were unstable. The off-diagonal components of the neutrinos density matrices grew exponentially in the linear regime. The domain-averaged diagonal component density matrix exhibited a long term asymptotic behavior in the non-linear regime, but failed to achieve complete flavor equipartition (Figure 5.4). The flavor changes of the computational particles showed no discernible pattern; however, the oscillation amplitudes were in the order of magnitude of 10^0 (Figure 5.5).

To test the sensitivity of the dependence on the initial condition, I defined a flavor state vector whose components were all the neutrino and antineutrino density matrix components of the computational particles. This vector completely captured the flavor state of the entire neutron star merger neutrino simulation. I conducted two neutron star merger neutrino simulations with close initial conditions (a difference between the initial flavor state vector of 10^{-6}). When both simulations were restarted at $t = 0$ ns, the difference between the flavor states increased exponentially according to the fast unstable modes (Figure 5.6). After fast unstable modes saturated in the non-linear domain, the difference between the flavor states kept expanding exponentially but with a lower rate. This trend was better observed when both simulations were restarted in the non-linear regime. The difference between the flavor states showed a strong exponential divergence pattern (Figure 5.7). This showed that the neutrino flavor simulation of the neutron star merger was highly sensitive and unstable to the initial conditions, implying chaos.

For the neutron star merge simulation, I also examined how the difference between the flavor states behaved along the trajectory in the state space of the solutions. In order to address this, I ran two neutron star merger neutrino simulations with an initial difference between the flavor state vectors of 10^{-6} and periodically normalized one of the simulations while maintaining the direction of the vector between them. This procedure follows the Bennettin algorithm that is normally used to determine the highest Lyapunov exponent in chaotic systems [3]. The solution's location in the state space had a significant impact on the exponential trend of the difference between the flavor state vectors (Figure 5.9). Due to conservation of phase-space volume in the neutrino quantum kinetic equations, the exponential growth rate spectrum had convergence zones (negative Lyapunov exponents). The main tendency (exponential growth rate) of the initial divergence between the two solution was approximately $3 \times 10^8 \text{ s}^{-1}$. This is a lower limit for the real value of the maximum Lyapunov exponent.

The impact of the sensitive dependence on the initial condition of the neutron star merger simulation on a single computation particle was also studied. An initial uncertainty of 10^{-10} in the trace of the neutrinos density matrix will increase exponentially, reaching the value of one in around 75 ns. This means a 100% uncertainty in each computational particle flavor state (Figure 5.8).

Understanding the whole neutrino flavor oscillation phenomenon in astrophysical systems is very difficult due to its chaotic character and strong dependence on the initial condition. In this work, this was reflected in the high uncertainty in both the spatial flavor neutrino distribution and the density matrix of the individual computational particles. However, in global simulations of core-collapse supernovae and neutron star mergers, the main interest is in the domain-averaged density matrix component defined by the spatial resolution of the simulation. As was demonstrated in this work, the domain-averaged neutrino density matrix component is not highly impacted by chaos and can be used as a key variable in the global simulation of core-collapse supernovae and neutron star mergers.

References

- [1] John N Bahcall, Aldo M Serenelli, and Sarbani Basu. New solar opacities, abundances, helioseismology, and neutrino fluxes. *The Astrophysical Journal*, 621(1):L85, 2005.
- [2] Cyrille Rossant. *IPython Interactive Computing and Visualization Cookbook: Over 100 hands-on recipes to sharpen your skills in high-performance numerical computing and data science in the Jupyter Notebook*. Packt Publishing Ltd, 2018.
- [3] Giancarlo Benettin, Luigi Galgani, Antonio Giorgilli, and Jean-Marie Strelcyn. Lyapunov characteristic exponents for smooth dynamical systems and for hamiltonian systems; a method for computing all of them. part 1: Theory. *Meccanica*, 15:9–20, 1980.
- [4] Takaaki Kajita. Atmospheric neutrino results from super-kamiokande and kamiokande — evidence for oscillations. *Nuclear Physics B - Proceedings Supplements*, 77(1-3):123–132, may 1999.
- [5] Q. R. Ahmad, R. C. Allen, T. C. Andersen, et al. Measurement of the rate of $\nu_e + d \rightarrow p + p + e^-$ interactions produced by ^8B solar neutrinos at the sudbury neutrino observatory. *Phys. Rev. Lett.*, 87:071301, Jul 2001.
- [6] S. P. Mikheyev and A. Yu. Smirnov. Resonant amplification of ν oscillations in matter and solar-neutrino spectroscopy. *Il Nuovo Cimento C*, 9, 1986.
- [7] L. Wolfenstein. Neutrino oscillations in matter. *Phys. Rev. D*, 17:2369–2374, May 1978.
- [8] Irene Tamborra and Shashank Shalgar. New developments in flavor evolution of a dense neutrino gas. *Annual Review of Nuclear and Particle Science*, 71(1):165–188, 2021.
- [9] Huaiyu Duan and James P Kneller. Neutrino flavour transformation in supernovae. *Journal of Physics G: Nuclear and Particle Physics*, 36(11):113201, 2009.
- [10] Hiroki Nagakura and Masamichi Zaizen. Time-dependent, quasi-steady, and global features of fast neutrino-flavor conversion, 2022.
- [11] Sherwood Richers and Manibrata Sen. Fast flavor transformations. *arXiv preprint arXiv:2207.03561*, 2022.
- [12] Alessandro Mirizzi, Irene Tamborra, H-Th Janka, Ninetta Saviano, Kate Scholberg, Robert Bollig, Lorenz Hüdepohl, and Sovan Chakraborty. Supernova neutrinos: production, oscillations and detection. *La Rivista del Nuovo Cimento*, 39(1):1–112, 2016.
- [13] Hans-Thomas Janka. Explosion mechanisms of core-collapse supernovae. *Annual Review of Nuclear and Particle Science*, 62(1):407–451, 2012.
- [14] David Branch and J Craig Wheeler. *Supernova explosions*, volume 4. Springer, 2017.

- [15] Jakob Ehring, Sajad Abbar, Hans-Thomas Janka, Georg Raffelt, and Irene Tamborra. Fast neutrino flavor conversion in core-collapse supernovae: A parametric study in 1d models. *Phys. Rev. D*, 107:103034, May 2023.
- [16] Michael A. Sandoval, W. Raphael Hix, O. E. Bronson Messer, Eric J. Lentz, and J. Austin Harris. Three-dimensional core-collapse supernova simulations with 160 isotopic species evolved to shock breakout. *The Astrophysical Journal*, 921(2):113, nov 2021.
- [17] Takami Kuroda, Tobias Fischer, Tomoya Takiwaki, and Kei Kotake. Core-collapse supernova simulations and the formation of neutron stars, hybrid stars, and black holes. *The Astrophysical Journal*, 924(1):38, jan 2022.
- [18] Adam Burrows, David Radice, David Vartanyan, Hiroki Nagakura, M Aaron Skinner, and Joshua C Dolence. The overarching framework of core-collapse supernova explosions as revealed by 3D furnaces simulations. *Monthly Notices of the Royal Astronomical Society*, 491(2):2715–2735, 11 2019.
- [19] Evan O’Connor, Robert Bollig, Adam Burrows, Sean Couch, Tobias Fischer, Hans-Thomas Janka, Kei Kotake, Eric J Lentz, Matthias Liebendörfer, O E Bronson Messer, Anthony Mezzacappa, Tomoya Takiwaki, and David Vartanyan. Global comparison of core-collapse supernova simulations in spherical symmetry. *Journal of Physics G: Nuclear and Particle Physics*, 45(10):104001, sep 2018.
- [20] Shashank Shalgar and Irene Tamborra. Supernova neutrino decoupling is altered by flavor conversion, 2022.
- [21] David Radice, Albino Perego, Francesco Zappa, and Sebastiano Bernuzzi. Gw170817: Joint constraint on the neutron star equation of state from multimessenger observations. *The Astrophysical Journal Letters*, 852(2):L29, jan 2018.
- [22] Ben Margalit and Brian D. Metzger. The multi-messenger matrix: The future of neutron star merger constraints on the nuclear equation of state. *The Astrophysical Journal Letters*, 880(1):L15, jul 2019.
- [23] M. R. Mumpower, R. Surman, D.-L. Fang, M. Beard, P. Möller, T. Kawano, and A. Aprahamian. Impact of individual nuclear masses on r -process abundances. *Phys. Rev. C*, 92:035807, Sep 2015.
- [24] Sherwood Richers, Don E. Willcox, Nicole M. Ford, and Andrew Myers. Particle-in-cell simulation of the neutrino fast flavor instability. *Phys. Rev. D*, 103:083013, Apr 2021.
- [25] David Radice, Sebastiano Bernuzzi, and Albino Perego. The dynamics of binary neutron star mergers and gw170817. *Annual Review of Nuclear and Particle Science*, 70(1):95–119, 2020.
- [26] Oliver Just, Sajad Abbar, Meng-Ru Wu, Irene Tamborra, Hans-Thomas Janka, and Francesco Capozzi. Fast neutrino conversion in hydrodynamic simulations of neutrino-cooled accretion disks. *Phys. Rev. D*, 105:083024, Apr 2022.
- [27] Meng-Ru Wu, Yong-Zhong Qian, Gabriel Martínez-Pinedo, Tobias Fischer, and Lutz Huther. Effects of neutrino oscillations on nucleosynthesis and neutrino signals for an 18 m supernova model. *Physical Review D*, 91(6):065016, 2015.
- [28] Jonas Lippuner, Rodrigo Fernández, Luke F. Roberts, Francois Foucart, Daniel Kasen, Brian D. Metzger, and Christian D. Ott. Signatures of hypermassive neutron star lifetimes on r -process nucleosynthesis in the disc ejecta from neutron star mergers. *Monthly Notices of the Royal Astronomical Society*, 472(1):904–918, 08 2017.

- [29] Takashi Yoshida, Toshitaka Kajino, Hidekazu Yokomakura, Keiichi Kimura, Akira Takamura, and Dieter H. Hartmann. Supernova neutrino nucleosynthesis of light elements with neutrino oscillations. *Physical Review Letters*, 96(9), mar 2006.
- [30] Eric Burns. Neutron star mergers and how to study them. *Living Reviews in Relativity*, 23(1):4, 2020.
- [31] Rodrigo Fernández and Brian D. Metzger. Electromagnetic signatures of neutron star mergers in the advanced ligo era. *Annual Review of Nuclear and Particle Science*, 66(1):23–45, 2016.
- [32] Raffaella Margutti and Ryan Chornock. First multimessenger observations of a neutron star merger. *Annual Review of Astronomy and Astrophysics*, 59(1):155–202, 2021.
- [33] David Radice, Sebastiano Bernuzzi, and Albino Perego. The dynamics of binary neutron star mergers and GW170817. 70(1):95–119.
- [34] B. P. Abbott, R. Abbott, T. D. Abbott, F. Acernese, et al. Gw170817: Observation of gravitational waves from a binary neutron star inspiral. *Phys. Rev. Lett.*, 119:161101, Oct 2017.
- [35] B. P. Abbott, R. Abbott, T. D. Abbott, F. Acernese, et al. Multi-messenger observations of a binary neutron star merger*. *The Astrophysical Journal Letters*, 848(2):L12, oct 2017.
- [36] P. S. Cowperthwaite, E. Berger, V. A. Villar, B. D. Metzger, et al. The electromagnetic counterpart of the binary neutron star merger ligo/virgo gw170817. ii. uv, optical, and near-infrared light curves and comparison to kilonova models. *The Astrophysical Journal Letters*, 848(2):L17, oct 2017.
- [37] Jennifer Barnes and Daniel Kasen. Effect of a high opacity on the light curves of radioactively powered transients from compact object mergers. *The Astrophysical Journal*, 775(1):18, aug 2013.
- [38] Daniel Kasen, N. R. Badnell, and Jennifer Barnes. Opacities and spectra of the r-process ejecta from neutron star mergers. *The Astrophysical Journal*, 774(1):25, aug 2013.
- [39] Francois Foucart, Philipp Mösta, Teresita Ramirez, Alex James Wright, Siva Darbha, and Daniel Kasen. Estimating outflow masses and velocities in merger simulations: Impact of r-process heating and neutrino cooling. *Phys. Rev. D*, 104:123010, Dec 2021.
- [40] Philipp Mösta, David Radice, Roland Haas, Erik Schnetter, and Sebastiano Bernuzzi. A magnetar engine for short grbs and kilonovae. *The Astrophysical Journal Letters*, 901(2):L37, oct 2020.
- [41] Vsevolod Nedora, Federico Schianchi, Sebastiano Bernuzzi, David Radice, Boris Daszuta, Andrea Endrizzi, Albino Perego, Aviral Prakash, and Francesco Zappa. Mapping dynamical ejecta and disk masses from numerical relativity simulations of neutron star mergers. *Classical and Quantum Gravity*, 39(1):015008, dec 2021.
- [42] Zhenyu Zhu and Luciano Rezzolla. Fully general-relativistic simulations of isolated and binary strange quark stars. *Phys. Rev. D*, 104:083004, Oct 2021.
- [43] Brian D. Metzger and Rodrigo Fernández. From neutrino- to photon-cooled in three years: Can fallback accretion explain the x-ray excess in gw170817? *The Astrophysical Journal Letters*, 916(1):L3, jul 2021.
- [44] Xinyu Li and Daniel M. Siegel. Neutrino fast flavor conversions in neutron-star postmerger accretion disks. *Phys. Rev. Lett.*, 126:251101, Jun 2021.

- [45] O Just, S Goriely, H-Th Janka, S Nagataki, and A Bauswein. Neutrino absorption and other physics dependencies in neutrino-cooled black hole accretion discs. *Monthly Notices of the Royal Astronomical Society*, 509(1):1377–1412, 10 2021.
- [46] Sherwood Richers, Donald Willcox, and Nicole Ford. Neutrino fast flavor instability in three dimensions. *Phys. Rev. D*, 104:103023, Nov 2021.
- [47] Amol V. Patwardhan, Michael J. Cervia, Ermal Rrapaj, Pooja Siwach, and A. B. Balantekin. Many-body collective neutrino oscillations: Recent developments. In *Handbook of Nuclear Physics*, pages 1–16. Springer Nature Singapore, nov 2022.
- [48] Joshua D. Martin, A. Roggero, Huaiyu Duan, and J. Carlson. Many-body neutrino flavor entanglement in a simple dynamic model, 2023.
- [49] Ermal Rrapaj. Exact solution of multiangle quantum many-body collective neutrino-flavor oscillations. *Phys. Rev. C*, 101:065805, Jun 2020.
- [50] Pooja Siwach, Anna M. Suliga, and A. Baha Balantekin. Entanglement in three-flavor collective neutrino oscillations. *Phys. Rev. D*, 107:023019, Jan 2023.
- [51] Alessandro Roggero. Dynamical phase transitions in models of collective neutrino oscillations. *Phys. Rev. D*, 104:123023, Dec 2021.
- [52] Alessandro Roggero. Entanglement and many-body effects in collective neutrino oscillations. *Phys. Rev. D*, 104:103016, Nov 2021.
- [53] Michael J. Cervia, Amol V. Patwardhan, A. B. Balantekin, S. N. Coppersmith, and Calvin W. Johnson. Entanglement and collective flavor oscillations in a dense neutrino gas. *Phys. Rev. D*, 100:083001, Oct 2019.
- [54] Sebastian Paeckel, Thomas Köhler, Andreas Swoboda, Salvatore R. Manmana, Ulrich Schollwöck, and Claudius Hubig. Time-evolution methods for matrix-product states. *Annals of Physics*, 411:167998, 2019.
- [55] Francesco Capozzi and Ninetta Saviano. Neutrino flavor conversions in high-density astrophysical and cosmological environments. *Universe*, 8(2), 2022.
- [56] Evan Grohs, Sherwood Richers, Sean M Couch, Francois Foucart, James P Kneller, and GC McLaughlin. Neutrino fast flavor instability in three dimensions for a neutron star merger. *arXiv preprint arXiv:2207.02214*, 2022.
- [57] Huaiyu Duan and Alexander Friedland. Self-induced suppression of collective neutrino oscillations in a supernova. *Phys. Rev. Lett.*, 106:091101, Mar 2011.
- [58] Basudeb Dasgupta. Collective neutrino flavor instability requires a crossing. *Physical Review Letters*, 128(8):081102, 2022.
- [59] Taiki Morinaga. Fast neutrino flavor instability and neutrino flavor lepton number crossings. *Physical Review D*, 105(10):L101301, 2022.
- [60] Meng-Ru Wu and Irene Tamborra. Fast neutrino conversions: Ubiquitous in compact binary merger remnants. *Phys. Rev. D*, 95:103007, May 2017.
- [61] Raymond F Sawyer. Speed-up of neutrino transformations in a supernova environment. *Physical Review D*, 72(4):045003, 2005.
- [62] Raymond F Sawyer. Multiangle instability in dense neutrino systems. *Physical Review D*, 79(10):105003, 2009.

- [63] R. F. Sawyer. Neutrino cloud instabilities just above the neutrino sphere of a supernova. *Phys. Rev. Lett.*, 116:081101, Feb 2016.
- [64] Manu George, Meng-Ru Wu, Irene Tamborra, Ricard Ardevol-Pulpillo, and Hans-Thomas Janka. Fast neutrino flavor conversion, ejecta properties, and nucleosynthesis in newly-formed hypermassive remnants of neutron-star mergers. *Phys. Rev. D*, 102:103015, Nov 2020.
- [65] Meng-Ru Wu, Irene Tamborra, Oliver Just, and Hans-Thomas Janka. Imprints of neutrino-pair flavor conversions on nucleosynthesis in ejecta from neutron-star merger remnants. *Phys. Rev. D*, 96:123015, Dec 2017.
- [66] Sajad Abbar and Huaiyu Duan. Fast neutrino flavor conversion: Roles of dense matter and spectrum crossing. *Phys. Rev. D*, 98:043014, Aug 2018.
- [67] Xinyu Li and Daniel M. Siegel. Neutrino fast flavor conversions in neutron-star postmerger accretion disks. *Phys. Rev. Lett.*, 126:251101, Jun 2021.
- [68] Meng-Ru Wu, Manu George, Chun-Yu Lin, and Zewei Xiong. Collective fast neutrino flavor conversions in a 1d box: Initial conditions and long-term evolution. *Physical Review D*, 104(10):103003, 2021.
- [69] Zewei Xiong and Yong-Zhong Qian. Stationary solutions for fast flavor oscillations of a homogeneous dense neutrino gas. *Physics Letters B*, 820:136550, 2021.
- [70] Joshua D Martin, John Carlson, Vincenzo Cirigliano, and Huaiyu Duan. Fast flavor oscillations in dense neutrino media with collisions. *Physical Review D*, 103(6):063001, 2021.
- [71] Sajad Abbar, Huaiyu Duan, Kohsuke Sumiyoshi, Tomoya Takiwaki, and Maria Cristina Volpe. On the occurrence of fast neutrino flavor conversions in multidimensional supernova models. *Phys. Rev. D*, 100:043004, Aug 2019.
- [72] Robert Glas, H.-Thomas Janka, Francesco Capozzi, Manibrata Sen, Basudeb Dasgupta, Alessandro Mirizzi, and Günter Sigl. Fast neutrino flavor instability in the neutron-star convection layer of three-dimensional supernova models. *Phys. Rev. D*, 101:063001, Mar 2020.
- [73] Francesco Capozzi, Sajad Abbar, Robert Bollig, and H.-Thomas Janka. Fast neutrino flavor conversions in one-dimensional core-collapse supernova models with and without muon creation. *Phys. Rev. D*, 103:063013, Mar 2021.
- [74] Sajad Abbar, Francesco Capozzi, Robert Glas, H.-Thomas Janka, and Irene Tamborra. On the characteristics of fast neutrino flavor instabilities in three-dimensional core-collapse supernova models. *Phys. Rev. D*, 103:063033, Mar 2021.
- [75] Hiroki Nagakura, Adam Burrows, Lucas Johns, and George M. Fuller. Where, when, and why: Occurrence of fast-pairwise collective neutrino oscillation in three-dimensional core-collapse supernova models. *Phys. Rev. D*, 104:083025, Oct 2021.
- [76] Soumya Bhattacharyya and Basudeb Dasgupta. Fast flavor depolarization of supernova neutrinos. *Phys. Rev. Lett.*, 126:061302, Feb 2021.
- [77] Sajad Abbar and Francesco Capozzi. Suppression of fast neutrino flavor conversions occurring at large distances in core-collapse supernovae. *Journal of Cosmology and Astroparticle Physics*, 2022(03):051, mar 2022.
- [78] Zewei Xiong, Andre Sieverding, Manibrata Sen, and Yong-Zhong Qian. Potential impact of fast flavor oscillations on neutrino-driven winds and their nucleosynthesis. *The Astrophysical Journal*, 900(2):144, sep 2020.

- [79] Manu George, Meng-Ru Wu, Irene Tamborra, Ricard Ardevol-Pulpillo, and Hans-Thomas Janka. Fast neutrino flavor conversion, ejecta properties, and nucleosynthesis in newly-formed hypermassive remnants of neutron-star mergers. *Phys. Rev. D*, 102:103015, Nov 2020.
- [80] Rasmus Sloth Hansen and Steen Hannestad. Chaotic flavor evolution in an interacting neutrino gas. *Phys. Rev. D*, 90:025009, Jul 2014.
- [81] Zewei Xiong, Meng-Ru Wu, and Yong-Zhong Qian. Symmetry and bipolar motion in collective neutrino flavor oscillations, 2023.
- [82] Shunsaku Horiuchi and James P Kneller. What can be learned from a future supernova neutrino detection? *Journal of Physics G: Nuclear and Particle Physics*, 45(4):043002, mar 2018.
- [83] Carlo Giunti and Chung W Kim. *Fundamentals of neutrino physics and astrophysics*. Oxford university press, 2007.
- [84] Kai Zuber. *Neutrino physics*. Taylor & Francis, 2020.
- [85] Fumihiko Suekane. *Neutrino Oscillations: A Practical Guide to Basics and Applications*, volume 898. 2015.
- [86] David Griffiths. *Introduction to elementary particles*. Wiley-VCH, 2008.
- [87] Mark Thomson. *Modern particle physics*. Cambridge University Press, 2013.
- [88] John N Bahcall. Solar neutrinos. i. theoretical. *Physical Review Letters*, 12(11):300, 1964.
- [89] JN Bahcall, William A Fowler, I Iben Jr, and RL Sears. Solar neutrino flux. *The Astrophysical Journal*, 137:344–346, 1963.
- [90] Bruce T. Cleveland, Timothy Daily, Jr. Raymond Davis, James R. Distel, Kenneth Lande, C. K. Lee, Paul S. Wildenhain, and Jack Ullman. Measurement of the solar electron neutrino flux with the homestake chlorine detector. *The Astrophysical Journal*, 496(1):505, mar 1998.
- [91] Raymond Davis, Don S. Harmer, and Kenneth C. Hoffman. Search for neutrinos from the sun. *Phys. Rev. Lett.*, 20:1205–1209, May 1968.
- [92] John N. Bahcall, Neta A. Bahcall, and Giora Shaviv. Present status of the theoretical predictions for the ^{37}Cl solar-neutrino experiment. *Phys. Rev. Lett.*, 20:1209–1212, May 1968.
- [93] J.N. Abdurashitov, E.L. Faizov, V.N. Gavrin, A.O. Gusev, A.V. Kalikhov, T.V. Knodel, I.I. Knysenko, V.N. Kornoukhov, I.N. Mirmov, A.M. Pshukov, A.M. Shalagin, A.A. Shikhin, P.V. Timofeyev, E.P. Veretenkin, V.M. Vermul, G.T. Zatsepin, T.J. Bowles, J.S. Nico, W.A. Teasdale, D.L. Wark, J.F. Wilkerson, B.T. Cleveland, T. Daily, R. Davis, K. Lande, C.K. Lee, P.W. Wildenhain, S.R. Elliott, M.L. Cherry, and R.T. Kouzes. Results from sage (the russian-american gallium solar neutrino experiment). *Physics Letters B*, 328(1):234–248, 1994.
- [94] P. Anselmann et al. Solar neutrinos observed by GALLEX at Gran Sasso. *Phys. Lett. B*, 285:376–389, 1992.
- [95] S. Fukuda, Y. Fukuda, M. Ishitsuka, Y. Itow, et al. Solar ^8B and hep neutrino measurements from 1258 days of super-kamiokande data. *Phys. Rev. Lett.*, 86:5651–5655, Jun 2001.
- [96] Keiko S Hirata, K Inoue, T Ishida, T Kajita, K Kihara, M Nakahata, K Nakamura, S Ohara, A Sakai, N Sato, et al. Observation of a small atmospheric $\nu\mu/\nu\text{e}$ ratio in kamiokande. *Physics Letters B*, 280(1-2):146–152, 1992.

- [97] KS Hirata, T Kajita, M Koshiba, M Nakahata, S Ohara, Y Oyama, N Sato, A Suzuki, M Takita, Y Totsuka, et al. Experimental study of the atmospheric neutrino flux. *Physics Letters B*, 205(2-3):416–420, 1988.
- [98] Y Fukuda, T Hayakawa, K Inoue, T Ishida, S Joukou, T Kajita, S Kasuga, Y Koshio, T Kumita, K Matsumoto, et al. Atmospheric $\nu\mu\bar{\nu}$ ratio in the multi-gev energy range. *Physics Letters B*, 335(2):237–245, 1994.
- [99] Y. Fukuda, T. Hayakawa, E. Ichihara, et al. Evidence for oscillation of atmospheric neutrinos. *Phys. Rev. Lett.*, 81:1562–1567, Aug 1998.
- [100] Ziro Maki, Masami Nakagawa, and Shoichi Sakata. Remarks on the Unified Model of Elementary Particles. *Progress of Theoretical Physics*, 28(5):870–880, 11 1962.
- [101] Makoto Kobayashi and Toshihide Maskawa. CP-Violation in the Renormalizable Theory of Weak Interaction. *Progress of Theoretical Physics*, 49(2):652–657, 02 1973.
- [102] Nicola Cabibbo. Unitary symmetry and leptonic decays. *Physical Review Letters*, 10(12):531, 1963.
- [103] Particle Data Group. Review of Particle Physics. *Progress of Theoretical and Experimental Physics*, 2020(8), 08 2020. 083C01.
- [104] X. Qian and P. Vogel. Neutrino mass hierarchy. *Progress in Particle and Nuclear Physics*, 83:1–30, 2015.
- [105] Albino Perego, Sebastiano Bernuzzi, and David Radice. Thermodynamics conditions of matter in neutron star mergers. *The European Physical Journal A*, 55(8):1–21, 2019.
- [106] A Burrows. Neutrinos from supernova explosions. *Annual Review of Nuclear and Particle Science*, 40:181–212, 1990.
- [107] Lucas Johns and Zewei Xiong. Collisional instabilities of neutrinos and their interplay with fast flavor conversion in compact objects. *Physical Review D*, 106(10):103029, 2022.
- [108] Zewei Xiong, Meng-Ru Wu, Gabriel Martínez-Pinedo, Tobias Fischer, Manu George, Chun-Yu Lin, and Lucas Johns. Evolution of collisional neutrino flavor instabilities in spherically symmetric supernova models. *Physical Review D*, 107(8):083016, 2023.
- [109] Lucas Johns. Collisional flavor instabilities of supernova neutrinos. *Physical Review Letters*, 130(19):191001, 2023.
- [110] Rasmus S. L. Hansen, Shashank Shalgar, and Irene Tamborra. Enhancement or damping of fast neutrino flavor conversions due to collisions. *Phys. Rev. D*, 105:123003, Jun 2022.
- [111] Stuart Samuel. Neutrino oscillations in dense neutrino gases. *Physical Review D*, 48(4):1462, 1993.
- [112] Chinami Kato and Hiroki Nagakura. Effects of energy-dependent scatterings on fast neutrino flavor conversions. *Phys. Rev. D*, 106:123013, Dec 2022.
- [113] Arka Banerjee, Amol Dighe, and Georg Raffelt. Linearized flavor-stability analysis of dense neutrino streams. *Physical Review D*, 84(5):053013, 2011.
- [114] Taiki Morinaga. Fast neutrino flavor instability and neutrino flavor lepton number crossings. *Phys. Rev. D*, 105:L101301, May 2022.
- [115] Masamichi Zaizen and Hiroki Nagakura. Simple method for determining asymptotic states of fast neutrino-flavor conversion.

- [116] S.H. Strogatz. *Nonlinear Dynamics and Chaos: With Applications to Physics, Biology, Chemistry, and Engineering*. Studies in Nonlinearity. Avalon Publishing, 2014.
- [117] Edward Ott. *Chaos in dynamical systems*. Cambridge University Press, 2 edition, 2002.
- [118] Gregory L. Baker and Jerry P. Gollub. *Chaotic Dynamics: An Introduction*. Cambridge University Press, 2 edition, 1996.
- [119] Robert C Hilborn. *Chaos and nonlinear dynamics: an introduction for scientists and engineers*. Oxford University Press, 2 edition, 2000.
- [120] J.R. Taylor. *Classical Mechanics*. University Science Books, 2005.
- [121] Alexander Schaum. Applied nonlinear dynamics.
- [122] Alessandro Colombo. Notes of nonlinear dynamics.
- [123] Sandro Wimberger. *Nonlinear dynamics and quantum chaos*, volume 10. Springer, 2014.
- [124] H Poincaré. Les méthodes nouvelles de la mécanique céleste. *Gauthier-Villars et Fils*, 1, 1892.
- [125] Edward N. Lorenz. Deterministic nonperiodic flow. *Journal of Atmospheric Sciences*, 20(2):130 – 141, 1963.
- [126] George M Zaslavsky and Georgij Moisevič Zaslavskij. *Hamiltonian chaos and fractional dynamics*. Oxford University Press, 2005.
- [127] Robert M May. Biological populations with nonoverlapping generations: stable points, stable cycles, and chaos. *Science*, 186(4164):645–647, 1974.
- [128] BA Huberman, JP Crutchfield, and NH Packard. Noise phenomena in josephson junctions. *Applied Physics Letters*, 37(8):750–752, 1980.
- [129] Troy Shinbrot, Celso Grebogi, Jack Wisdom, and James A Yorke. Chaos in a double pendulum. *American Journal of Physics*, 60(6):491–499, 1992.
- [130] Robert M May and George F Oster. Bifurcations and dynamic complexity in simple ecological models. *The American Naturalist*, 110(974):573–599, 1976.
- [131] A Libchaber, C Laroche, and Stephan Fauve. Period doubling cascade in mercury, a quantitative measurement. *Journal de Physique Lettres*, 43(7):211–216, 1982.
- [132] Marzio Giglio, Sergio Musazzi, and Umberto Perini. Transition to chaotic behavior via a reproducible sequence of period-doubling bifurcations. *Physical Review Letters*, 47(4):243, 1981.
- [133] Paul S Linsay. Period doubling and chaotic behavior in a driven anharmonic oscillator. *Physical review letters*, 47(19):1349, 1981.
- [134] James Testa, José Pérez, and Carson Jeffries. Evidence for universal chaotic behavior of a driven nonlinear oscillator. *Physical Review Letters*, 48(11):714, 1982.
- [135] FT Arecchi and F Lisi. Hopping mechanism generating 1 f noise in nonlinear systems. *Physical Review Letters*, 49(2):94, 1982.
- [136] WJ Yeh and YH Kao. Universal scaling and chaotic behavior of a josephson-junction analog. *Physical Review Letters*, 49(26):1888, 1982.

- [137] Masamichi Zaizen and Taiki Morinaga. Nonlinear evolution of fast neutrino flavor conversion in the preshock region of core-collapse supernovae. *Phys. Rev. D*, 104:083035, Oct 2021.
- [138] Lucas Johns, Hiroki Nagakura, George M. Fuller, and Adam Burrows. Fast oscillations, collisionless relaxation, and spurious evolution of supernova neutrino flavor. *Phys. Rev. D*, 102:103017, Nov 2020.
- [139] Francois Foucart, Evan O'Connor, Luke Roberts, Lawrence E Kidder, Harald P Pfeiffer, and Mark A Scheel. Impact of an improved neutrino energy estimate on outflows in neutron star merger simulations. *Physical Review D*, 94(12):123016, 2016.
- [140] J. Cernohorsky and S. A. Bludman. Maximum Entropy Distribution and Closure for Bose-Einstein and Fermi-Dirac Radiation Transport. , 433:250, September 1994.

Appendix: Convergence tests

I am especially interested in the convergence of the value of λ in the exponential divergence between two neutrino flavor solutions that start in close flavor states (baseline simulation \vec{r}_{bas} and perturbed simulation \vec{r}_{per}) that evolve as

$$\begin{aligned} |\vec{r}_{\text{bas}} - \vec{r}_{\text{per}}| &= A_0 e^{\lambda(t-t_0)} \\ t &\geq t_0. \end{aligned} \tag{Eq. 6.0.1}$$

this is equivalence to Eq. 3.3.3 (see Section 3.3 for a discussion of chaos and their relation with the exponential divergence of solutions with close initial condition). \vec{r} is the state vector¹ of the entire neutrino system

$$\vec{r} = \sum_i \sum_{\alpha, \beta} \rho_{\alpha\beta}^i \hat{e}_{\alpha\beta}^i, \tag{Eq. 6.0.2}$$

where i run over all the particles in the system and α and β run over the diagonal and upper components of the neutrino density matrix $\rho_{\alpha\beta}^i$.

The baseline simulation is the one-dimensional fiducial simulation (see Section 5.1 or reference [24] for more details). However, I will arbitrarily change the simulation parameters to obtain the convergence in the exponent λ . The perturbed simulation is the baseline simulation plus a small perturbation in a random direction at a specific time t_0

$$\vec{r}_{\text{per}}(t_0) = \vec{r}_{\text{bas}}(t_0) + \vec{r}_{\text{random}}, \tag{Eq. 6.0.3}$$

where the magnitude of the perturbation is $|\vec{r}_{\text{random}}| = A_0$. Both the original and perturbed simulations are then evolved forward in time.

To compute the value of λ in Eq. 6.0.2 I used the least squares linear fit method ($y = mx + b$) with the `numpy.polyfit()` function once the two solutions \vec{r}_{bas} and \vec{r}_{per} are known. Using $y = \ln |\vec{r}_{\text{bas}} - \vec{r}_{\text{per}}|$, $m = \lambda$, $x = t - t_0$ and $b = \ln A_0$ the `numpy.polyfit()` function return values of $\ln A_0$ and λ that minimize the sum of the squares of the residuals.

The particle-in-cell neutrino simulations in EMU depend on three imposed parameters: the domain size, the number of cells and the number of particles. The number of cells and the number of particles do not represent any physical parameters, and the result must be independent of the choice of them. However, these parameters must be carefully chosen to ensure convergence in the physical parameter under study. If the simulation domain is too small to contain the system's fastest unstable growth mode, the instability will grow more slowly than in reality. On the other hand, as the small-scale neutrino behavior depends on the number of cells; unstable modes with wavelengths shorter than the cell size, or equivalently, frequencies greater than the characteristic Nyquist frequency, will not emerge in the simulation.

In environments with high neutrino densities, the neutrino distribution is very well described as a continuous function with an effectively infinite number of neutrinos. To computationally

¹The vector \vec{r} is not a physical vector since it does not satisfy the transformation rules of physical vectors. Indeed, it represents in vector notation the solution of the system of differential equations that describe the time evolution of the neutrino density matrix components.

discretize the neutrino distribution, the particle-in-cell method clumps the real neutrinos into packages called particles (see Section 4 for more details on the discretization of the neutrino field). To obtain a good approximation of the original continuous distribution, it is necessary to consider many particles. The number of particles in the simulation also affect the angular resolution of the simulation. As the neutrino-neutrino coherent forward-scattering Hamiltonian in equation 2.5.3 depends on the neutrino direction, many particles imply that a greater number of neutrinos will be represented in different directions, increasing the precision of the simulation.

An important factor in the computation of the exponent λ is the amplitude of the initial perturbation $|\vec{r}_{\text{random}}| = A_0$. A small perturbation can lead to subtractive cancelation errors. On the other hand, high amplitudes can potentially stop the exponential trend once it has reached the divergence limit.

In the following subsections, I will test the impact of the domain size, number of cells, number of particles and perturbation amplitude on λ . This will help us to determine the set of parameters for which the simulation safely reproduces the value of λ .

Number of particles test

To determine whether λ is affected by the number of particles, we performed five baseline simulations in which neutrinos were emitted in a roughly isotropic distribution from each cell's center. We considered 92, 378, 6022, 24088 and 54202 directions for each case. The simulation domain was considered to be $1 \times 1 \times 64$ cm divided by 1024 cells in the \hat{z} direction.

I restarted the baseline simulations during the non-linear phase after saturation of the instability ($t = 2.65 \times 10^{-9}$ seconds). I added a perturbation of amplitude 10^{-6} in a random direction and let the neutrino solutions evolve until the simulation reached a time of 2×10^{-8} seconds or $|\vec{r}_{\text{bas}} - \vec{r}_{\text{per}}|$ reached a value of 10^{-2} .

The values of λ obtained can be observed as \bullet points in Figure 6.1. It is feasible to see that as the number of directions increases, the values of λ drop. Around the 24088 directions, convergence is attained. The number of particle in the simulation has a big impact on the exponential divergence of two nearby initial conditions states, implying that a high-precision simulation is needed to get convergence in λ .

Perturbation Amplitude Test

To assess the impact of the random perturbation \vec{r}_{random} on λ , we performed a baseline simulation with a domain of $1 \times 1 \times 64$ cm divided by 1024 cells in the \hat{z} direction. Each cell is initialized with 24088 particles at the center of the cell emitted in an approximately isotropic distribution.

As in the previous test, I restarted the baseline simulation during the nonlinear phase after saturation of the instability ($t = 2.65 \times 10^{-9}$ seconds). I ran five separate simulations starting from this point in time for three different random perturbation amplitudes: 1×10^{-6} , 1×10^{-8} and 1×10^{-10} . To calculate λ , I separately evolve the neutrino states \vec{r}_{bas} and the 15 perturbed \vec{r}_{per} . I terminate the simulation at 2×10^{-8} seconds or until the vector magnitude $|\vec{r}_{\text{bas}} - \vec{r}_{\text{per}}|$ reaches a value of 10^{-2} .

The values of λ obtained for an initial perturbation amplitude of 10^{-10} can be observed as \bullet points in Figure 6.2. λ varies from an average value of $6.10 \times 10^8 \text{ s}^{-1}$ with a standard deviation of $\sigma = 0.4 \times 10^8 \text{ s}^{-1}$. The blue area in Figure 6.2 shows the 2σ region.

We went through the same process again using perturbation amplitudes of 10^{-8} and 10^{-10} verify that the measurement of lambda is independent of the perturbation amplitude. In Figure 6.2, the outcomes are represented by the points \bullet and \bullet , respectively. For a initial perturbation amplitude of 10^{-8} the values of λ vary from an average of $6.11 \times 10^8 \text{ s}^{-1}$ with a standard deviation of $\sigma = 2.28 \times 10^7 \text{ s}^{-1}$. The values of λ for the simulations with an initial perturbation amplitude of 10^{-6} fluctuates from an average value of $6.48 \times 10^5 \text{ s}^{-1}$ with a standard deviation of $\sigma = 6.28 \times 10^3 \text{ s}^{-1}$.

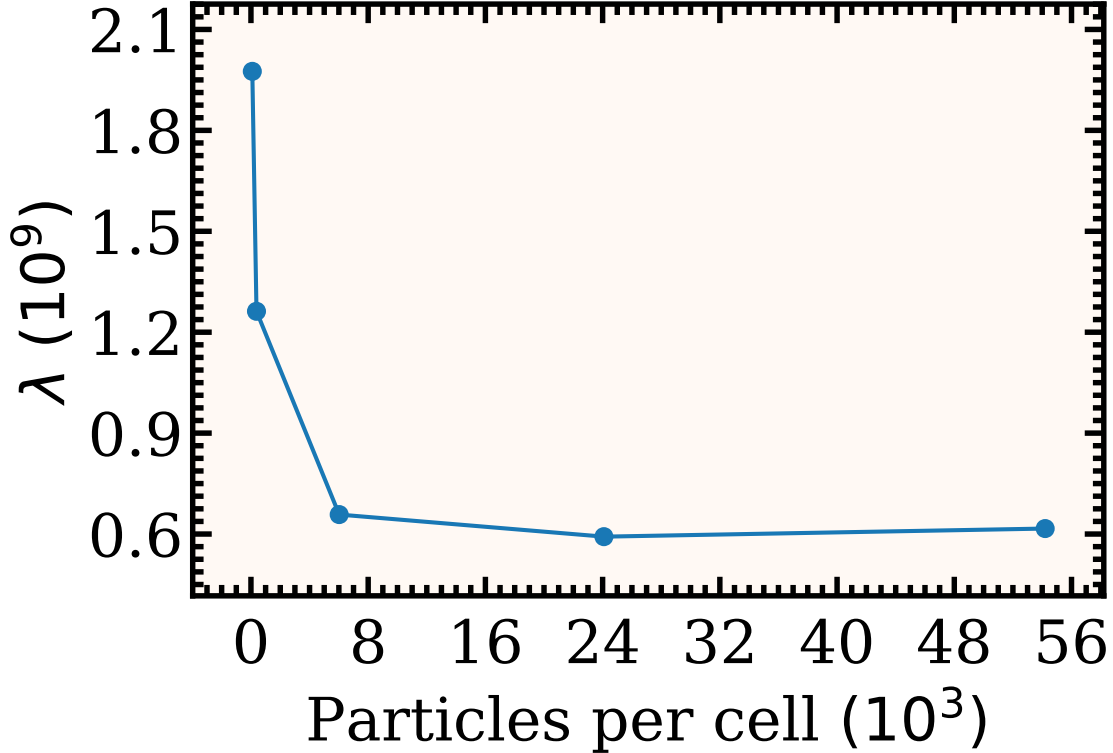


Figure 6.1: Test for convergence of the number of particles. The vertical axis shows the computed values of the exponent λ in equation $|\vec{r}_{\text{bas}} - \vec{r}_{\text{per}}| = A_0 e^{\lambda(t-t_0)}$ for five one-dimensional fiducial simulations in which were emitted 92, 378, 6022, 24088 and 54202 particles per cell in an approximately isotropic fashion. Each simulation used a $1 \times 1 \times 64$ centimeter domain divided into 1024 cells in the z direction. We added perturbation of magnitude $A_0 = 10^{-10}$ in a random direction when the neutrino system reached the non-linear regime. As the number of particles in the simulation grow, the values of λ obtained drop. The convergence is attained for a number of directions greater than 24088.

Less spread in λ is generated by bigger perturbations amplitudes. However, this does not change the mean significantly $\lambda = 6.11 \times 10^8 \text{ s}^{-1}$. At a perturbation amplitude of 10^{-6} the spread of λ is negligible and this amplitude can be considered as a convergence point.

Domain size test

I conducted three baseline simulations with domain sizes of 16, 32, and 64 cm in the \hat{z} direction and 1 cm in the \hat{x} and \hat{y} directions to examine the impact of the domain size in λ . The number of cell was established to have 16 cells per centimeter in the \hat{z} direction. From the center of each cell, 24088 particles were emitted in an approximately isotropic distribution.

As in the previous tests, I restarted the baseline simulations adding a perturbation of magnitude 10^{-6} in a random direction. We applied the perturbation at $t = 2.65 \times 10^{-9}$ seconds. This coincides with the neutrino solutions' non-linear phase after saturation of the instability. I only let the neutrino states evolve until the simulation reaches a time of 2×10^{-8} seconds or until the value of $|\vec{r}_{\text{bas}} - \vec{r}_{\text{per}}|$ reaches 10^{-2} .

In Figure 6.3 the computed values of λ are depicted as \bullet points. The values of λ are not highly impacted by the simulation domain and they stay approximately constant as the domain increase.

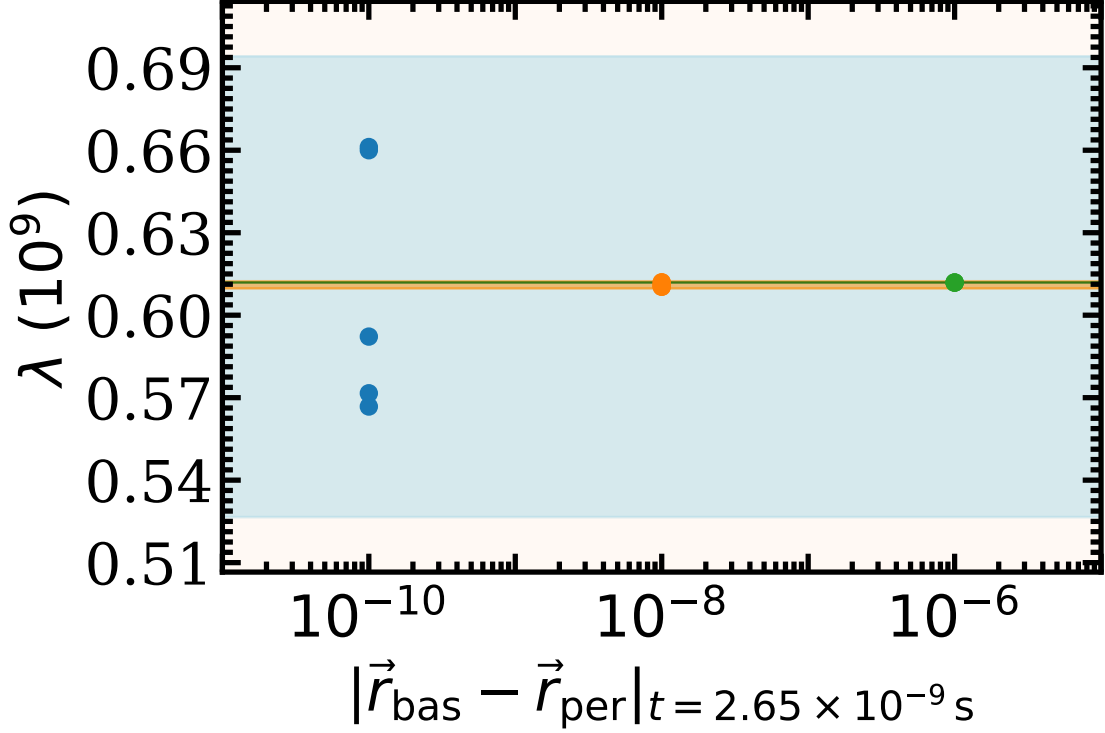


Figure 6.2: Test for convergence of the perturbation amplitude. Calculated values of λ in equation $|\vec{r}_{\text{bas}} - \vec{r}_{\text{per}}| = A_0 e^{\lambda(t - 2.65 \times 10^{-9})}$ for five one-dimensional fiducial simulations for each of the three initial perturbation amplitudes: $A_0 = 10^{-6}, 10^{-8}, 10^{-10}$. Each simulation has a domain of $1 \times 1 \times 64$ cm with 1024 cells in the \hat{z} direction and 24088 particles emitted in an approximately isotropic distribution from the center of each cell. The blue-shaded region represents a 2σ spread for λ with an initial perturbation amplitude of 10^{-10} . Less dispersion in λ is produced by bigger perturbations without changing the mean significantly. The orange-shaded region represents a 2σ spread for λ with an initial perturbation amplitude of 10^{-8} , the for green-shaded region represent the same for a perturbation amplitude of 10^{-6} .

Without losing any rigorously, in this work, I will consider a simulation domain of $1 \times 1 \times 64$ cm.

Number of cells test

To examine the impact of the number of cells on the computation of λ . I performed three baseline simulations with 256, 512 and 1024 cells. We considered a domain of $1 \times 1 \times 64$ cm. Each cell's center released neutrinos in 24088 directions with a roughly isotropic distribution.

As in the previous analysis, we restart the simulation in the non-linear phase after the saturation of the instability ($t = 2.65 \times 10^{-9}$ seconds) adding a perturbation of magnitude 10^{-6} in random direction. We only evolve the neutrino states until the simulation reach a time of 2×10^{-8} seconds or $|\vec{r}_{\text{bas}} - \vec{r}_{\text{per}}|$ reach a value of 10^{-2} .

The result of the computation of λ can be observed as \bullet points in Figure 6.4. The values of λ are slightly affected by the number of cells in the simulation, slowly increasing as the number of cell increase.

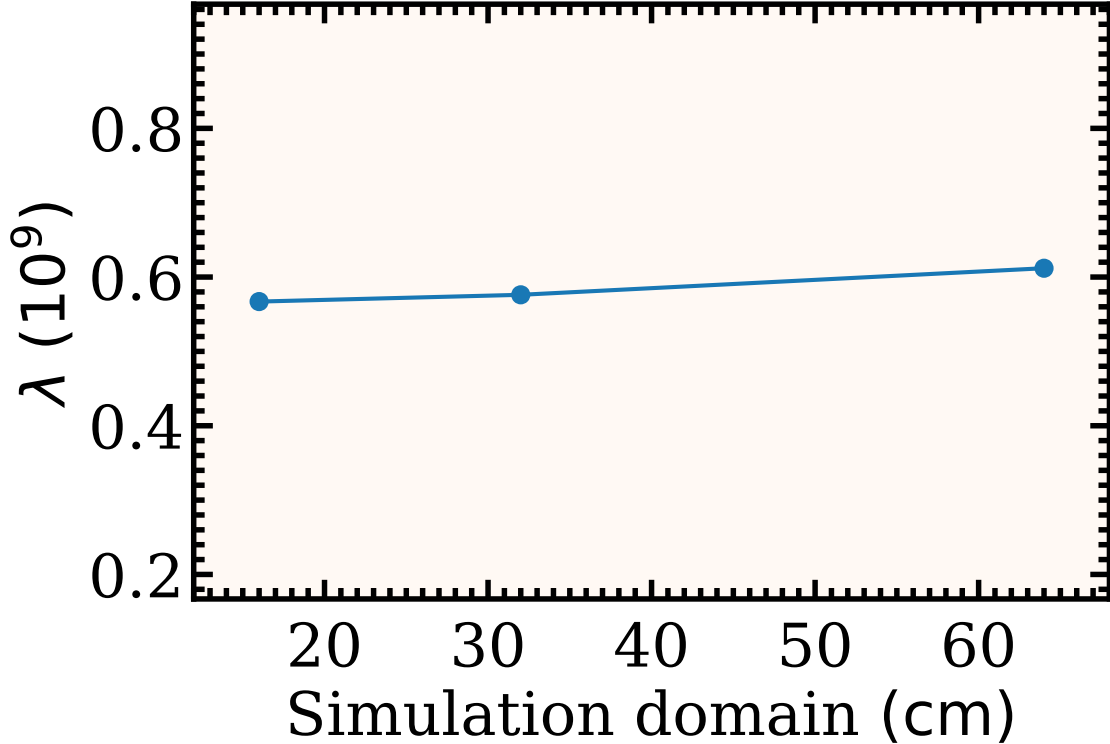


Figure 6.3: Test for convergence of the simulation domain. Calculated values of λ in equation $|\vec{r}_{\text{bas}} - \vec{r}_{\text{per}}| = A_0 e^{\lambda(t-t_0)}$ for three one-dimensional fiducial simulations with domains of 16, 32 and 64 cm in the \hat{z} and 1 cm in the \hat{x} and \hat{y} directions. 24088 particles per cells were consider in 16 cells per cm. Neutrinos were emitted in nearly isotropic directions. In the neutrino non-linear phase after saturation of the instability, we added a perturbation of magnitude $A_0 = 10^{-6}$ in a random direction. The values λ stay approximately constant as the simulation domain increase, having a small impact on the computation of λ .

Final setup

We showed that the simulation domain (Figure 6.3) and the number of cells (Figure 6.4) slightly impact the values of λ in the equation

$$|\vec{r}_{\text{bas}} - \vec{r}_{\text{per}}| = A_0 e^{\lambda(t-2.65 \times 10^{-9})}. \quad (\text{Eq. 6.0.4})$$

However, λ showed high sensitivity to the number of particles in the simulation (Figure 6.1). I found that in order to get convergence in λ it is necessary to consider more than 24088 particles emitted per cell in an approximately isotropic distribution. The spread of the values of λ was influenced by the perturbation amplitude. Given that the double variables in C++ used in EMU can hold 25 significant digits, I reasoned that perturbation amplitudes of 10^{-6} are small enough to accommodate a tiny spread of λ without producing numerical issues (Figure 6.2).

Previous works have shown that in order to get convergence in the average over the entire domain of the neutrino distributions after the instability saturates and the value of the unstable modes of the neutrino fast instability, it is necessary to consider a simulation domain greater than $1 \times 1 \times 64$ cm with a number of cells in the \hat{z} direction greater than 1024 and 92 particles [24].

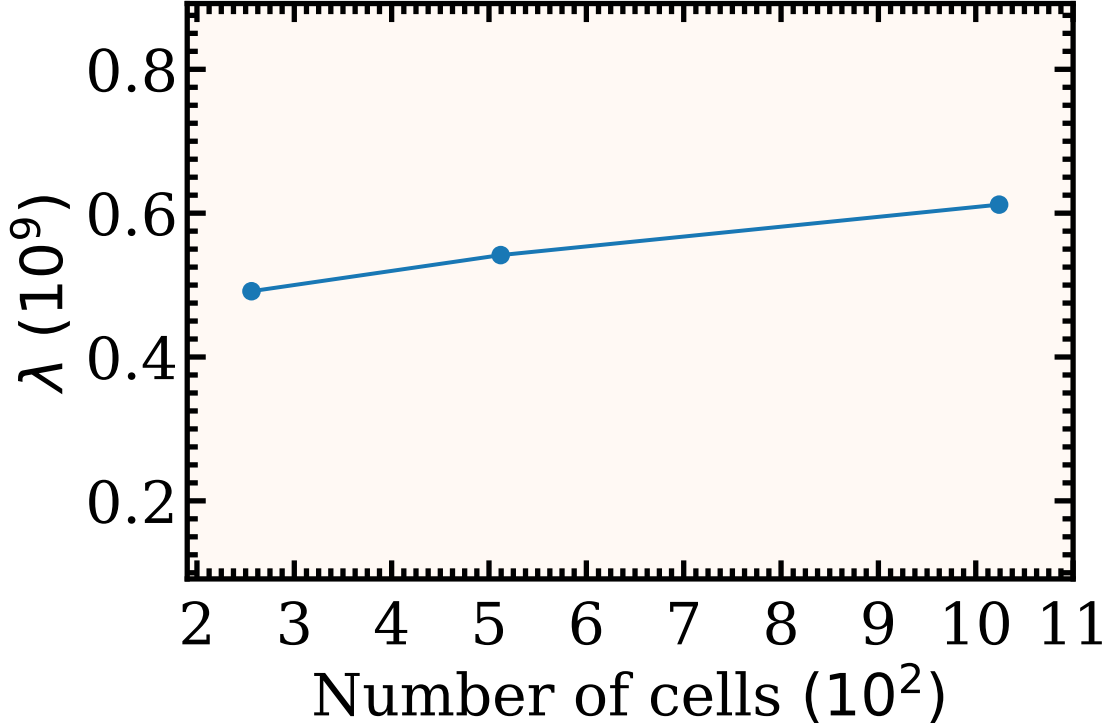


Figure 6.4: Test for convergence of the number of cells. Computed values of λ from equation $|\vec{r}_{\text{bas}} - \vec{r}_{\text{per}}| = A_0 e^{\lambda(t-t_0)}$ for three one-dimensional fiducial simulations with 256, 512 and 1024 cells. A $1 \times 1 \times 64$ cm domain was considered for all simulations. Neutrinos were emitted in nearly 24088 isotropic directions. We added a perturbation in a random direction of magnitude $A_0 = 10^{-6}$ when the neutrino system reached the non-linear phase after the saturation of the instability. The obtained values of λ slightly increase as the number of cells increase.

Using the four tests presented in this section together with the ones shown in reference [24], I concluded that the convergence in λ is obtained for a simulation with the following parameters:

- Simulation domain: $1 \times 1 \times 64$ cm
- Number of cells: 1024
- Number of directions per cell: 24088
- Perturbation amplitude: 10^{-6}

After the perturbation, we only allowed the neutrino states to develop for a maximum time of 1.7×10^{-8} seconds and for a value of $|\vec{r}_{\text{bas}} - \vec{r}_{\text{per}}|$ no greater than 10^{-2} .